Probing Cardiac Calcium Regulation Using Fluorescence Spectroscopy

A DISSERTATION

SUMBITTED TO THE FACULTY OF THE GRADUATE SCHOOL

OF THE UNIVERSITY OF MINNESOTA

BY

Elizabeth Lee Lockamy

IN PARTIAL FULFILLMENT OF THE REQUIREMENTS

FOR THE DEGREE OF

DOCTOR OF PHILOSOPHY

David D. Thomas, advisor

June 2011

ACKNOWLEDGEMENTS

I first want to thank my advisor, **Dr. David Thomas**, for allowing me to join his lab and for supporting me. Dave enticed me to come to his lab with assurances of a FRET drug screening venture that had landed on his doorstep. With my previous internships in industry, this project was my dream. I was able to continue developing my skills in assay development and drug screening while maintaining my other projects as graduate student. I realize how fortunate I have been to be a member of Dave's lab. I was given technicians, expensive toys, and any reagent I wanted. In addition, I was given the opportunity to travel every year to conferences from San Francisco, CA, to Boston, MA, to Aarhus, Denmark e.g. to share my research. Dave has illustrated to me the what the phrase, "Work hard. Party hard," means. I have learned from Dave to appreciate science, hard work, and fine wine.

I am grateful for **Dr. Deborah Ferrington**, who allowed me to be an honorary member of her lab. I was extremely fortunate to work with Deb as a rotation student during my first year. From this experience, I was able to publish a co-first author paper with her. I am indebted to Deb for giving me my first publication in graduate school. I was always welcomed in her lab, which became a place for me to escape whenever I was feeling overwhelmed. Her lab was also a source of fun – we made bonfires and s'mores, camped in her backyard, and rode on her pontoon boat. Deb showed me that a scientist can be both a loving mother and a disciplined teacher to her students and family at the same time. She has also demonstrated to me what dedication, perseverance, and a love a science can accomplish in one's career.

I would like to thank my committee, **Dr. John Lipscomb**, **Dr. Sharon Murphy**, and **Dr. Gianluigi Veglia**, for all the guidance and support you have given me especially these last years in graduate school.

Through my projects, I had the opportunity to work closely with **Dr. Razvan Cornea** and **Dr. Christine Karim**. Razvan has shown me that sheer curiosity can lead a person to many new exciting paths or to dead ends, but one should try to get an answer anyways. Without his creativeness, my projects probably would not have existed. Christine has illustrated that determination can carry a person far in life. She has also provided me with all the PLB I have needed over these past 6 years. Without her, none of my projects would have happened. Both Razvan and Christine have provided me with help and information involving SERCA and PLB. I appreciate their help and their friendship. Likewise, **Dr. Mike Autry** has been a source of vast knowledge in the SERCA-PLB field. I could rely on Mike for any literature question I had about this discipline.

To my membrane boys, **Kurt Torgerson**, **Simon Gruber**, **Zach James**, and **Jesse McCaffrey,** thank you for tolerating all of my quirks especially involving the cleanliness of our bench. I appreciate our discussions ranging from SERCA-PLB ideas all the way to philosophical views. Kurt was my classmate and travel buddy for 5 years. He was also a person I could gripe to about our classes, lab, and graduate school. Simon has shared my desk for the past 4 years and has probably been subjected to more of my peculiarities than anyone else in lab. We have had our fair share of silly yet intense arguments, but we've managed to remain friends. He challenges me daily to think critically about each method I perform and about what I say. I asked him to edit my

dissertation because I knew he would be my harshest critic. I am grateful to Simon for his opinion, his tolerance, and his friendship. Zach, thank you for the help with improving the co-reconstitution procedure. It was a time consuming project that will make everyone's lives easier on the membrane side. Jesse is the newest member to our corner, and he has brought a refreshing optimistic attitude that I hope the others don't destroy.

I trained each of my membrane boys, along with **Tyler Miller** and **Ji Li**, on multiple preps involving SERCA. Thanks to Tyler I probably graduated on time. He is wonderful technician, who always provided me with all the AEDANS-SERCA when I needed it. Since Ji and I work on similar projects, we were able to complain to each other about the woes of our research. He has also answered all my questions about fluorescent dyes and labeling procedures. Ji and **David Kast** both assisted with my education of the optical instruments and FargoFit. I also want to thank **Becca Moen** for allowing me to be a substitute teacher for her. It was a nice break from the lab in many ways. She also had a small hand in editing. I thank all of you for your friendship and the fun times together.

I also want to thank **Octavian Cornea** for assisting me with grant applications and with all of my computer problems. I also appreciate his friendship and small talk. Everyday, OC would drop by my wetlab desk to check on me and the lab. He will be the only person I allow to call me "Lizzy." OC, as I call him, is responsible along with **Sarah Blakely** in managing our entire lab. Without them, the Thomas Lab would crumble.

To all past and present members of the Thomas Lab, I have enjoyed getting to know all of you and working with you. We have had some entertaining times together

especially at Biophysical Society meetings and our own lab parties. I will always remember these adventures. For those continuing my projects, I wish you success plus a publication.

I would not have survived the Thomas Lab if it weren't for the friendship of **Sarah Blakely**, **Simon Gruber**, **Ben Matzke**, and **Christina Yi**. They have seen me at my best and my worst moments. They were always there with a sympathetic ear, a funny story, some comforting words, or the most recent gossip. I appreciate Sarah for her logical advice and cool headiness. Plus, her stories about her two adorable daughters were always good for a laugh. Simon, thank you again for you friendship and for tolerating me these past 4 years. Ben and Christina were the best undergraduates we ever had in the Thomas Lab. They were diligent and made lab more entertaining. They were also there with a hug when I needed one. Without them, the lab would not have been pleasant. I already miss Ben and Christina, who have graduated from the lab. I know I will have the same feelings about Sarah and Simon when I leave. Each of you deserves more credit than I have written. All I can say is that I am eternally grateful for each of you.

To **Nicole Waxmonsky, Leah Randles,** and **Nisha Patel**, thank you for getting me out the lab to explore the cities. Nicole, thank you for your encouragement and support throughout graduate school. She always challenged me to do more. I appreciated all of our times together especially our dinner and orchestra nights. Leah is an amazing, award-winning scientist, who is also a wonderful friend. I am glad we are not in the same class because my competition for awards would have increased. We have enjoyed many delectable breakfasts together and refreshing walks around the lakes with

her dog. Nisha has welcomed me into her circle of friends and exposed me to the world of law. I have enjoyed sharing these past two years together as roommates, and I look forward to the next few years. Nicole, Leah, and Nisha, each of you have provided memories that will last a lifetime.

Most importantly, I would like to thank my parents, **Al and Ginger**, and my sister, **Ginny**, for their unending love and unwavering support they have provided me throughout these years. We have celebrated, grieved, and enjoyed life together. They have listened to me complain more than they probably have wanted to do. My dad was always ready with a story to cheer me up about some crazy customer while my mom always reasoned with me, a task not for the faint at heart. Ginny has provided a source of understanding and wisdom that no one else could have given me. Words cannot express the gratitude and love that I have for each of you. Without you, I would not have accomplished all that I have. I hope you will accept my dissertation as a small token of my appreciation and my accomplishment.

DEDICATION

To my family, Al, Ginger, and Ginny Lockamy.

ABSTRACT

Calcium (Ca^{2+}) is stored in the sarcoplasmic reticulum (SR) in both cardiac and skeletal muscle. A Ca^{2+} induced Ca^{2+} release mechanism triggers the ryanodine receptor (RyR) to release Ca^{2+} from the SR into the cytoplasm. This Ca^{2+} discharge increases the Ca^{2+} concentration causing the muscle to contract. RyR is regulated by calmodulin (CaM), a Ca^{2+} binding protein that inhibits RyR when the $[Ca^{2+}] > \mu M$. To relax the muscle, the Sarco-endoplasmic Reticulum Calcium Adenosine Triphosphatase (SERCA), an integral membrane enzyme, pumps Ca^{2+} back into the SR driven by ATP hydrolysis. In cardiac tissue, SERCA is regulated by phospholamban (PLB), an integral membrane protein that inhibits SERCA at submicromolar $[Ca^{2+}]$. This inhibition is relieved either by addition of micromolar Ca^{2+} or by phosphorylation of PLB by cAMP-dependent protein kinase A (PKA).

The goal of this research was to investigate Ca^{2+} regulation during muscle contraction and relaxation. The major findings included: 1) two PLB variants bind tightly to SERCA, thus competing with and displacing wild-type (WT) PLB, 2) SERCA contains a novel nucleotide binding site that is not an artifact of crystallization, and 3) oxidation of specific Met residues in CaM are vital for proteasomal degradation.

Using functional co-reconstitution and fluorescence resonance energy transfer (FRET), we tested the hypothesis that the loss-of-function (LOF) mutants can compete with WT-PLB to relieve SERCA inhibition. We investigated two LOF mutants, S16E (phosphorylation mimic) and L31A, for their inhibitory potency and their ability to compete with WT-PLB. Our functional studies demonstrate that SERCA co-reconstituted with mixtures of WT-PLB and LOF PLB mutants had a lower inhibitory

potency compared to SERCA and WT-PLB mixtures only. FRET experiments added further support by showing that unlabeled LOF mutants lowered the FRET between donor-labeled SERCA and acceptor-labeled WT-PLB. Thus, we have provided a convenient FRET method for screening future PLB mutants for the use in gene therapy to treat heart failure.

Similarly, we used another fluorescence technique, time-resolved fluorescence resonance energy transfer (TR-FRET), to investigate nucleotide binding in SERCA. Based on biochemistry and crystallography, it has been proposed that SERCA has two distinct modes of nucleotide binding. To extend this observation from the crystal to the functional sarcoplasmic reticulum membrane, we have performed TR-FRET to measure the distance between donor-labeled SERCA and the fluorescent nucleotide TNP-ADP, in the presence and absence of inhibitors. TR-FRET experiments confirmed a novel binding site in SERCA, bringing the γ-phosphate of ADP closer to the phosphorylation site, Asp351, compared to other crystal structures with bound nucleotide. To determine whether these modes of nucleotide binding occur in solution during SERCA enzymatic cycle, we performed transient TR-FRET ($[TR]^2$FRET) experiments, in which a complete subnanosecond TR-FRET decay was recorded every 0.1 ms after rapid mixing of donor-labeled SERCA and TNP-ADP in a stopped-flow instrument. We clearly observed a biphasic reaction with a fast component (260 s^{-1}) and a slower component (17 s^{-1}). TR-FRET is a powerful technique for connecting structural dynamics of SERCA with its static crystal structures.

The major focus of this research has been muscle relaxation through the interaction of SERCA and PLB utilizing fluorescence spectroscopy. However, another

project with implications for muscle contraction concentrated on the signals for proteasomal degradation by using CaM as a model system. CaM variants were designed using site-directed mutagenesis in order to perform site-specific oxidation of Met residues. Utilizing circular dichroism (CD), thermodynamic stability CD experiments, and proteasomal degradation assays, it was demonstrated that oxidation of Met residues 51, 71, and 72 located in the N-terminus of CaM are essential for degradation. Functional data from ryanodine binding assays showed that oxidation of Met residues in the C-terminus of CaM completely abolished CaM's ability to bind and inhibit RyR. Accumulation of these CaM within the cell could be detrimental to CaM regulation of RyR impairing Ca^{2+} regulation during muscle contraction.

TABLE OF CONTENTS

LIST OF TABLES

LIST OF FIGURES

LIST OF EQUATIONS

ALPHABETICAL LIST OF ABBREVIATIONS

AMPPCP, adenylylmethylenediphosphonate disodium salt
AMPPNP, adenosine 5'-(β,γ-imido)triphosphate tetralithium salt
ANS, 1-anilinonaphthalene-8-sulfonate
ATP, adenosine triphosphate
BCA, bicinchoninic acid
$C_{12}E_8$, octaethyleneglycol monododecyl ether
Ca, divalent calcium ion (Ca^{2+})
CaM, calmodulin
CaMKII, calcium/calmodulin-dependent protein kinase II
CD, circular dichroism
CPA, cyclopiazonic acid
DABCYL-SE, 4-((4-(dimethylamino)phenyl)azo)-benzoic acid succinimidyl ester;
DMF, dimethylformamide
DOPC, 1,2-dioleoyl-sn-3-glycero-phosphocholine
DOPE, 1,2-dioleoyl-sn-3-glycero-phosphoethanolamine
EGTA, ethyleneglycol-bis-(2-aminoethyl ether)*N*,*N*,*N*,*N*-tetraacetic acid
EPR, electron paramagnetic resonance
ESI, electrospray ionization mass spectroscopy
FMOC, 9-fluorenylmethyloxycarbonyl
FRET, fluorescence resonance energy transfer
GOF, gain of function
HEK, human embryonic kidney
HEPES, 4-(2-hydroxyethyl)-1-piperazineethanesulfonic acid
HOMOPIPES, homopiperzine-1,4-bis(2-ethanesulfonic acid)
HPLC, high performance liquid chromatography
HSR, heavy sarcoplasmic reticulum
IADEANS, 5-((((2-iodoacetyl) amino) ethyl) amino) naphthalene-1-sulfonic acid
K_d, dissociation constant
kDa, kilodaltons
LOF, loss of function
MALDI-TOF, matrix-assisted laser desorption ionization time-of-flight
MOPS, 3-(*N*-morpholino)propanesulfonic acid
MTSSL, methanethiosulfonate spin label
NADH, nicotinamide adenine dinucleotide (reduced form)
NaOH, Sodium hydroxide
NKA, Na^+, K^+-ATPase
NMR, nuclear magnetic resonance
NZW, New Zealand White
pCa, -log[Ca^{2+}]
PDB, protein data bank
PEG-PS, polyethylene glycol–polystyrene (graft support)
P_i, inorganic phosphate
PIPES, 1,4-piperazinedietanesulfonic acid

PKA, cAMP dependent protein kinase A
pK_{Ca}, -log(K_{Ca}), calcium concentration at half-maximal ATPase activity
PLB, phospholamban
PLM, phospholemman
RyR, ryanodine receptor
SEM, standard error of the mean
SDS-PAGE, sodium dodecyl sulfate polyacrylamide gel electrophoresis
SERCA, sarco-endoplasmic reticulum calcium ATPase
SR, sarcoplasmic reticulum
TG, thapsigargin
TFE, trifluoroethanol
TM, transmembrane
TNP-ADP, 2'- *O*-(trinitrophenyl)adenosine 5'-diphosphate
TRIS, 2-amino-2-hydroxymethyl-propane-1,3-diol
WT, wild-type

CHAPTER 1 – Introduction

1.1. Proteins of the Sarcoplasmic Reticulum

The sarcoplasmic reticulum (SR) stores calcium (Ca^{2+}) in both cardiac and skeletal muscle. During an action potential, the ryanodine receptor (RyR) is stimulated by a Ca^{2+} induced Ca^{2+} release mechanism causing RyR to discharge Ca^{2+} into the cytoplasm, increasing the [Ca^{2+}] by 10,000 fold. This rise in [Ca^{2+}] results in muscle contraction (Figure 1) (*1*). In order for the muscle to relax, the Sacro-endoplasmic Reticulum Calcium Adenosine Triphosphatase (SERCA) pumps Ca^{2+} back into the SR

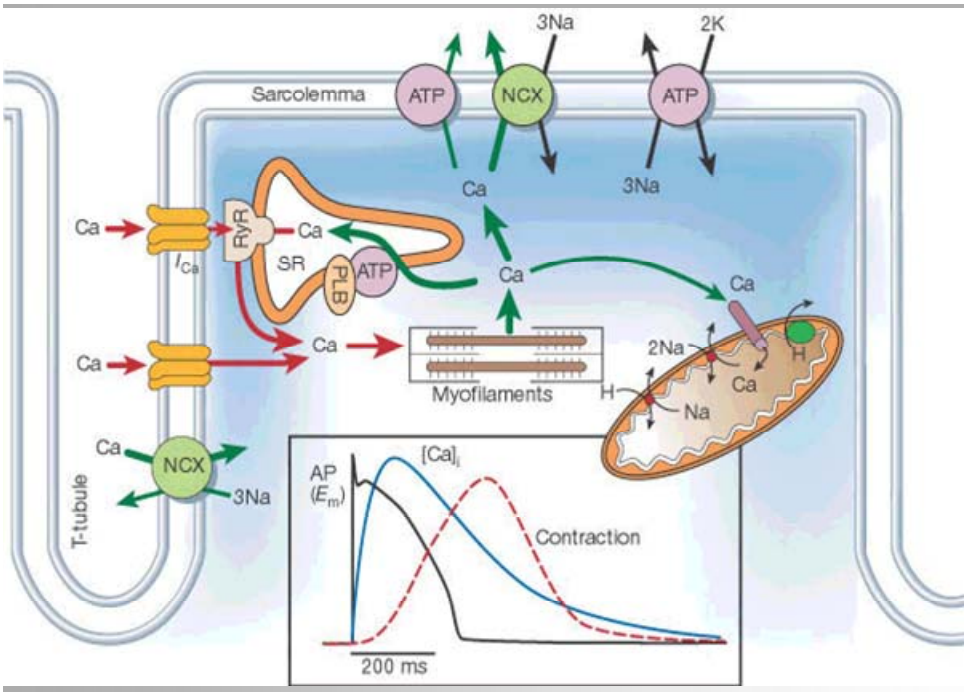

Figure 1: Contraction and relaxation of muscle. The sarcoplasmic reticulum (SR) is the primary storage unit of calcium in cardiac and skeletal muscle. The main calcium regulatory proteins in muscle are RyR, SERCA (labeled ATP in figure), and PLB. Upon stimulation, RyR releases Ca^{2+} into the cytoplasm causing the muscle to contract (*1*). SERCA is responsible for muscle relaxation by pumping the Ca^{2+} back into the SR. In cardiac muscle, SERCA is regulated by PLB.

against its concentration gradient. This process of transporting Ca^{2+} is driven by ATP hydrolysis, where 1 ATP is hydrolyzed per 2 Ca^{2+} ions carried back into the SR (*2-4*).

In the heart, SERCA is regulated by phospholamban (PLB), an integral membrane protein that inhibits SERCA at sub-micromolar [Ca^{2+}] (*5*). PLB exists in a dynamic equilibrium between a pentamer and monomer state. The monomeric PLB is thought to be the inhibitory form of SERCA (*6-8*). This inhibition is relieved by either micromolar [Ca^{2+}] or by phosphorylation of PLB by protein kinase A (PKA) at Ser 16 or by calcium/calmodulin kinase II (CaMKII) at Thr 17 (*5, 9*). The role of dual phosphorylation continues to be contentious, but it has been demonstrated that phosphorylation of Ser16 alone is enough to relieve inhibition of SERCA (*10, 11*).

1.2. RyR

1.2.1. RyR Structure

The ryanodine receptor (RyR) is composed of homotetramers of 550 kDa subunits yielding a 2.3 MDa Ca^{2+} sensitive release channel (Figure 2), the largest ion channel known to date (*13-15*). It is expressed in three isoforms sharing 65% sequence identity in mammals (*15*). They include RyR1 in skeletal muscle, RyR2 in cardiac muscle, and RyR3 in lower levels in various tissues.

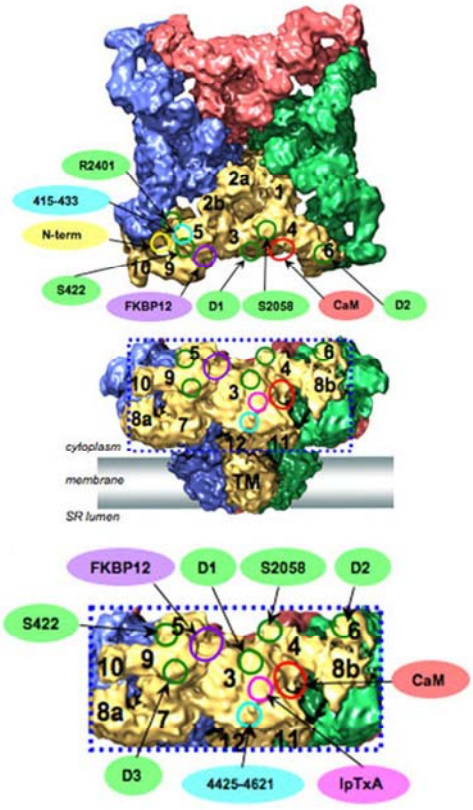

Figure 2: RyR structure. Cryo-electron microscopy structure at 9.6 A resolution. *Upper panel:* top view; *Middle panel:* side view; *Bottom panel*: side-view detail of binding sites for protein regulators (*12*).

The structures of these isoforms are virtually identical based on cryoelectron microscopy (*16-28*). The cytoplasmic domain of RyRs makes up ~80% of the channel while the transmembrane (TM) domain is ~20% of the channel. The transmembrane region contains the ion pore thought to involve 6 TM helices per subunit based on modeling with the mammalian potassium channel Kv1.2 (*21, 29*). The cytoplasmic region contains multiple indentations and grooves that are sites of interactions with protein regulators (Figure 2C). The corners of the cytoplasmic domain are called "clamps" that are connected to the "handle" domain encompassed by the "central rim" domain that joins the cytoplasmic and transmembrane regions together (*30*). The "clamps" undergo large conformational changes upon the opening and closing of the channel (*21, 25*). They are also proposed sites for RyR intermolecular interactions, and are sites for protein modulators to bind (*31-36*).

1.2.2. RyR Regulation

RyR regulation involves multiple interactions ranging from ions to protein modulators. Two protein regulators that bind to RyR are calmodulin (CaM) and FK506-binding proteins (FKBP) 12 and 12.6. CaM is a 17-kDa Ca^{2+} binding protein that binds to one site per RyR subunit (*37*). It has four EF-hand Ca^{2+} binding motifs total: 2 are located in the N- terminus and the other 2 are located in the C- terminus. CaM binds and regulates all three RyR isoforms in their Ca^{2+} free and Ca^{2+} bound states with different effects (*38, 39*). For RyR1, CaM acts as a partial agonist in the Ca^{2+}- free state whereas CaM acts as an inhibitor in the Ca^{2+} bound state (*40*). CaM binding inhibits RyR2 opening at all Ca^{2+} concentrations, increasing the threshold [Ca^{2+}] required to activate the channel (*40, 41*).

Both FKBP 12 and 12.6 bind to all RyR isoforms (*42*) at a ratio of four FKBPs per RyR channel (*43-45*). Each FKBP has different expression and binding affinities for RyR. For instance, FKBP12 binds mainly to RyR1 (*43, 46*) whereas FKBP12.6 binds predominantly to RyR2 (*47-50*). The proposed role of FKBP is to stabilize the closed form of RyR (*46, 51-55*).

1.3. SERCA

1.3.1. SERCA Enzymatic Cycle

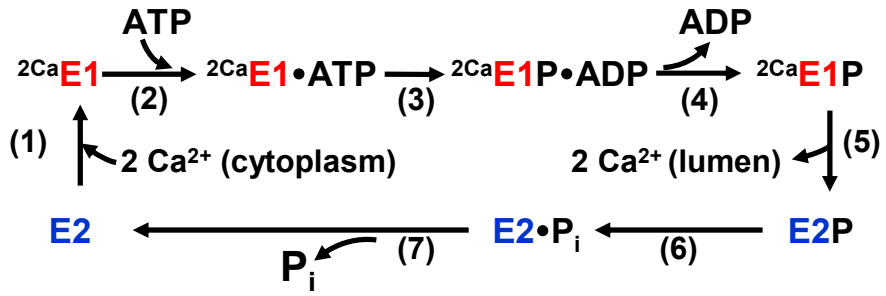

Figure 3: Schematic of SERCA enzymatic cycle. High Ca^{2+} affinity (E1) states are shown in red while low Ca^{2+} affinity (E2) states are shown in blue.

The enzymatic cycle of SERCA has been widely studied and is proposed to have two biochemical states, a high calcium affinity (E1) form and a low calcium affinity (E2) form (*56-61*). The cycle begins with apo-SERCA binding two Ca^{2+} ions in its transmembrane domain inducing a conformational change between the E2 and E1 states. This change permits Mg-ATP to bind within the nucleotide binding domain generating the E1-ATP state. SERCA then hydrolyzes ATP, transferring the γ-phosphate of ATP to Asp351, located in the phosphorylation domain of SERCA. Next, ADP is released producing a low Ca^{2+} affinity intermediate that releases the two Ca^{2+} ions into the SR lumen forming the E2 state. A conformational change brings about the E2-P state,

preparing SERCA to discharge the inorganic phosphate, and leaving it in the E2 state in order for the cycle to repeat itself (Figure 3).

1.3.2. Interchangeability of SERCA Isoforms

Humans have three SERCA genes (1, 2, and 3), each of which can be alternatively spliced and expressed in a tissue-dependent manner. SERCA1 isoforms (a and b) are mainly found in fast-twitch skeletal muscle, where SERCA1a is the adult form and SERCA1b is the embryonic form (*62-65*). SERCA2a is expressed primarily in the heart and slow-twitch skeletal muscle(*66*). Unlike SERCA 2a, SERCA 2b is expressed ubiquitously throughout all tissues (*67*). SERCA 3 isoforms are more diverse (a-f) and are located in non-muscle cells such as hematopoietic cells and in epithelial and endothelial cells (*68, 69*).

These isoforms have very few functional and structural differences between them. Their primary amino acid sequence is highly conserved. SERCA1a and SERCA2a have 84% identity whereas SERCA3a has 75% identity with SERCA1a and SERCA2a (*65*). Ca^{2+} binding sites, ATP binding site, and phosphorylation residue have been shown to be highly conserved based on mutagenesis studies (*70*). These studies also determined that the Ca^{2+} uptake and ATP and Ca^{2+} affinities were different amongst these isoforms (*71*). SERCA2 had a slower Ca^{2+} turnover rate and SERCA3 had lower affinity to Ca^{2+} compared to SERCA. These differences were attributed to the small variances in their sequences and their specific function in their localized expression (*70*). Overall, these isoforms have great similarities suggesting that they have analogous structures. One study that provided strong evidence that SERCA1 and SERCA2 can be interchanged with one another used transgenic mice expressing SERCA1a in the heart. They found that

SERCA1a had the same properties of SERCA2a when subjected to a cardiac environment (*72*). This finding allowed for SERCA1a to be used as a model for all isoforms in functional and structural studies. X-ray crystallography studies on SERCA have been done exclusively with SERCA1a since it is abundant in tissues, and these isoforms can be interchanged with each other.

1.3.3. SERCA Structure

SERCA is defined as a P-type ATPase because of its ability to auto-phosphorylate itself at Asp 351 during its enzymatic cycle. It contains four domains named for each domain's function: actuator (A), nucleotide binding (N), phosphorylation (P), and transmembrane (TM) domain (Figure 4). A-domain gates Ca^{2+}, N-domain contains the nucleotide binding site, P-domain includes the phosphorylation residue, Asp 351, and the TM- domain has ten α helices (M1-M10) that has the 2 Ca^{2+} binding sites. The transmembrane domain also contains a hydrophobic groove between M2, M4, M6, and M9 where PLB binds and regulates SERCA (*74*).

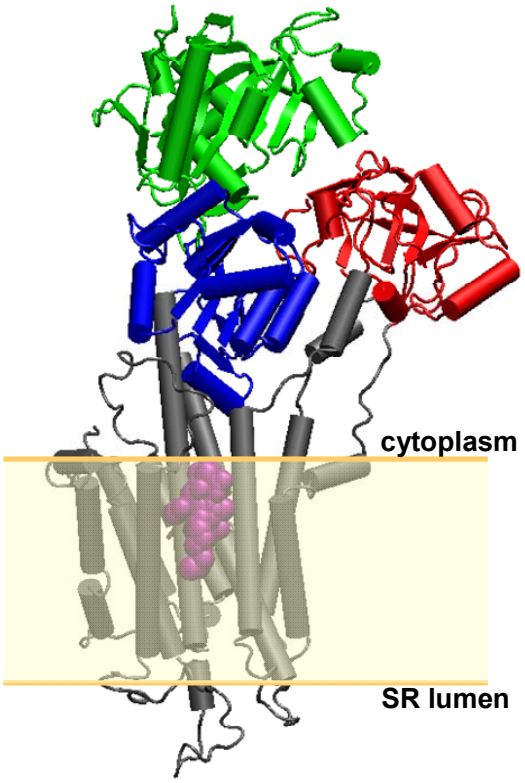

Figure 4: SERCA structure. The E2 (1IWO) crystal structure of SERCA showing the nucleotide binding (green), phosphorylation (blue), actuator (red), and transmembrane (grey) domains. Thapsigargin used to crystallize the E2 form is shown in purple (*73*). Structural representation made using PyMol.

The current number of crystals structures of SERCA has grown steadily since 2000 when the first structure was published (Figure 5) (*75*). These structures now include E1, E2, and intermediate biochemical states of SERCA with and without inhibitors. The first published structures contained inhibitors, thapsigargin (TG), cyclopiazonic acid (CPA) or 2,5-di(tert-butyl)-1,4-benzohydroquinone (BHQ) that were thought to stabilize the TM domain of SERCA in order to crystallize it (*73, 75-77*). However, in 2007, Olesen et al published the crystal structures of the E2-P and E2-P* ($E2\text{-}P_i$ in Figure 3) states without inhibitors. Comparing the structures with and without inhibitors, no major conformational changes were observed (*78*).

One contested SERCA structure has been the E1-Ca state. Its first published structure determined by x-ray crystallography contained a large opening, 6.6 nm, between the N and A domains in the presence of 10 mM Ca^{2+} (Figure 5) (*75*). Other x-ray structures with bound nucleotide in the E1 state only had 4 nm distance between these domains (*73, Sorensen, 2004 #233*). In 2008, the Thomas lab expressed SERCA with fusion proteins attached to the N and A domains in insect cells to determine if this large distance occurred physiologically or was it an artifact of crystallization. Using fluorescence

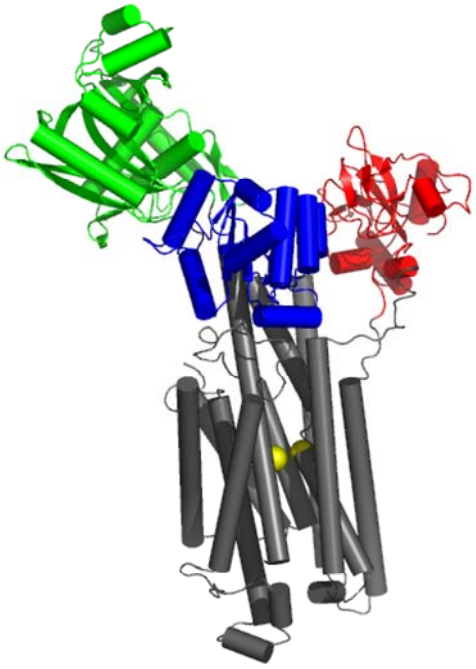

Figure 5: E1-Ca X-ray crystal structure of SERCA. First published E1-Ca crystal structure at 2.6 Å. Ribbon structure of SERCA is overlaid with surface rendering mode using PyMol and coordinates from PDB:ID 1SU4 (*75*). N domain (green), the P domain (blue), the A domain (yellow) and the ten TM α-helices (grey) are shown. Two Ca^{2+} ions (yellow) are highlighted.

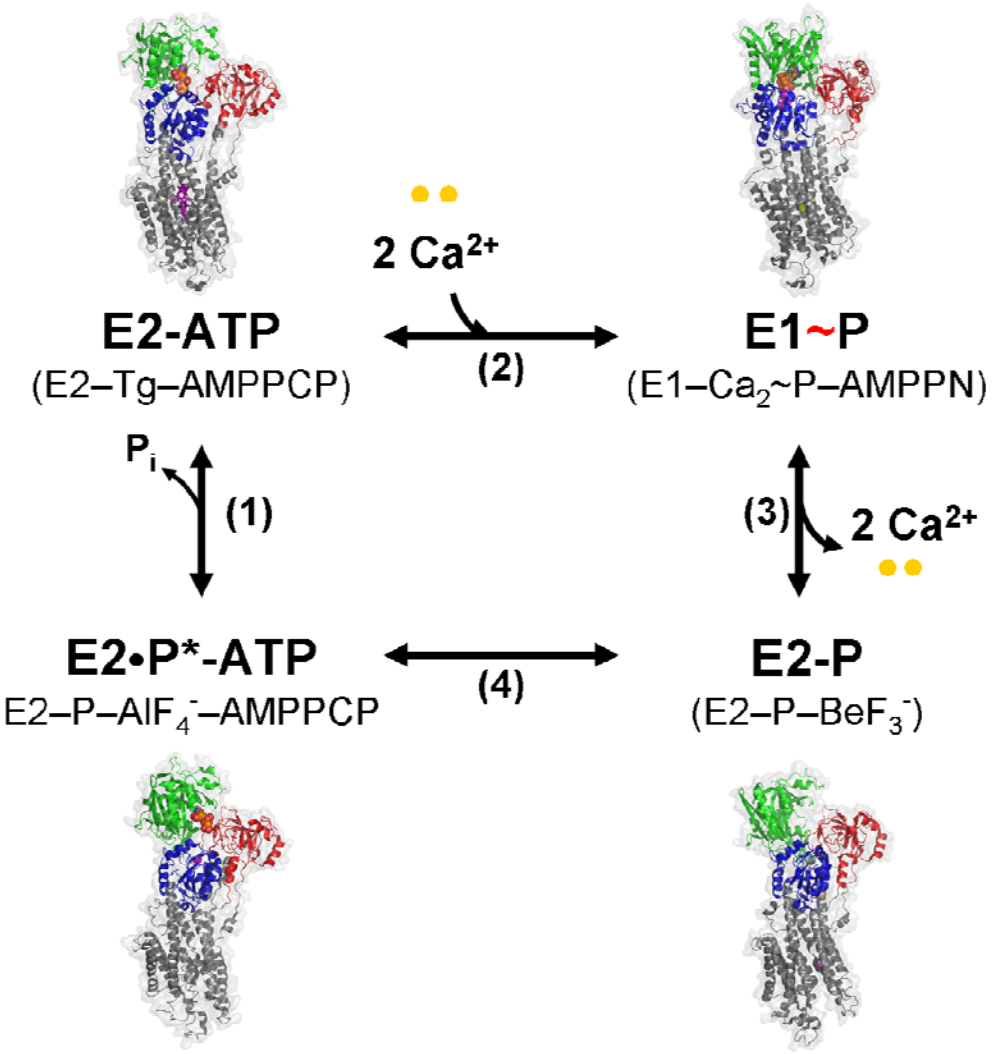

Figure 6: Schematic of SERCA enzymatic cycle with revised E1-Ca structure. Revised reaction scheme assumes E1 state has small opening and bound nucleotide or P_i at all intermediates of the enzymatic cycle. Model based on PDB:ID (1)1VFP, (2)1BA6, (3)3B9B, (4)3B9 (*78, 80*). Structural representations made using PyMol. Adapted from (*78*).

resonance energy transfer (FRET) and molecular modeling, we concluded that the distance between the N and A domains in the E1-Ca state is more compact, similar to the other structures in the enzymatic cycle (Figure 6)(*79*).

1.4. PLB

Phospholamban is a single-pass transmembrane protein containing 52 amino-acids and is known to regulate SERCA2a in cardiac tissue (*5*). It consists of three domains. Domain Ia (residues 1-16), located in the cytoplasm of the SR, contains a PKA phosphorylation site at Ser 16. The loop region (residues 17-22) acts as a flexible hinge that connects domain Ia to domain Ib (residues 23-31). Domain II (residues 31-52) comprises the transmembrane portion of PLB that is inserted into the membrane (Figure 7) (*81, 82*).

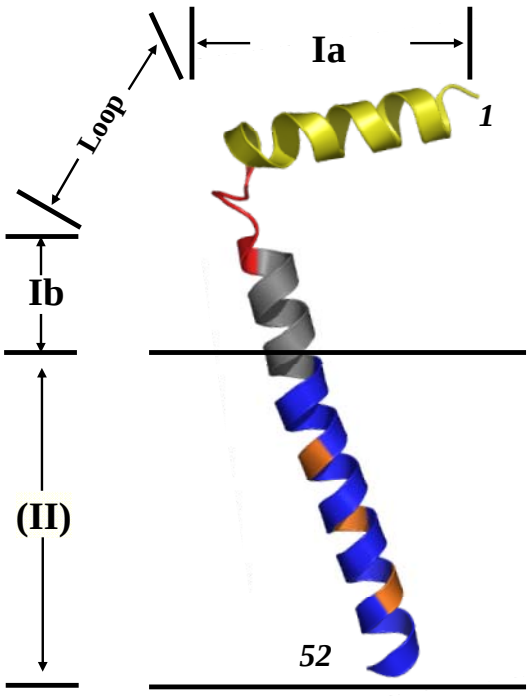

Figure 7: AFA-PLB structure in DPC micelles. NMR determined structure of AFA-PLB in DPC micelles (1N7L). Highlighted are domain Ia (yellow), the loop (red), domain Ib (grey), and domain II (blue). The three Cys residues which are mutated to Ala, Phe and Ala, respectively are colored in orange (*81*). Structural representation made using PyMol.

PLB exists in dynamic equilibrium between monomer and pentamer states. The monomeric species is the inhibitory form while the pentameric species acts a storage component for PLB in the membrane (*6-8*). Mutagenesis studies have shown that the pentamer form of PLB is stabilized by a leucine-isoleucine zipper in the transmembrane domain with three essential cysteines at positions 36, 41, and 46 (*6*). Further analysis revealed that mutating these three cysteines to Ala, Phe, and Ala respectively resulted in the monomeric species of PLB, referred to as AFA, with identical inhibitory properties (*83, 84*). Additional mutagenesis studies

demonstrated that the transmembrane domain of PLB was sufficient for inhibition while the cytoplasmic domain alone has no inhibitory effect (*85*). It has also been shown that the phosphorylation of PLB in cytoplasmic domain is responsible for the relief of inhibition (*85-87*).

Several models based on nuclear magnetic resonance (NMR) exist for PLB. The first structures were determined in organic solvents that revealed slight differences in the transmembrane domain. However, large differences were seen in the cytoplasmic domains. From these NMR experiments, four different models have been proposed: extended helix/sheet, continuous helix, bellflower, and pinwheel (Figure 8)(*88-92*). Collaborations between the Thomas and Veglia have sought to clarify the structure of the pentameric form of PLB. Using NMR and electron paramagnetic resonance (EPR), they determined that the pinwheel model of PLB most accurately describes the pentamer structure in both micelles and lipid bilayers (*91-94*). Further collaborations of these laboratories have yielded results on the orientation and dynamics of AFA, the monomeric PLB (Figure 9)(*95*).

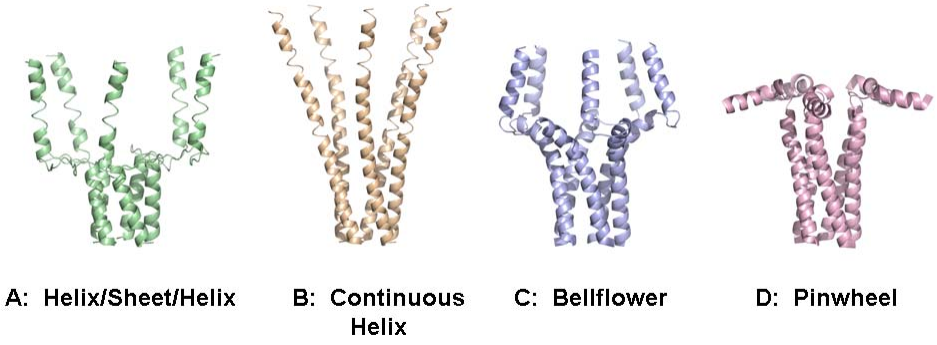

Figure 8: Proposed PLB pentamer structures. (A) Helix/sheet/helix (*88*). (B) Continuous helix (*89*). (C) Bellflower [PDB:ID 1ZLL (*90*) (D) Pinwheel [PDB:ID 1XNU (*91*) Structural representations made using PyMol. Adapted from (*92*).

1.5. SERCA-PLB Complex and Regulation

Currently, no crystal structure exists with PLB bound to SERCA. However, a model based on cross-linking, crystallography, and NMR experiments was created utilizing molecular dynamic calculations (*74, 96, 97*). PLB was docked into SERCA, and its transmembrane domain was shown to interact with M2, M4, M6, and M9 of SERCA (Figure 10). Domain Ib of PLB was modeled to be an extended disorder region while domain Ia was considered to be α-helical lying in a groove on M9 of SERCA. Both phosphorylation sites are exposed in this model, and these sites are important for the regulation of SERCA (*98*).

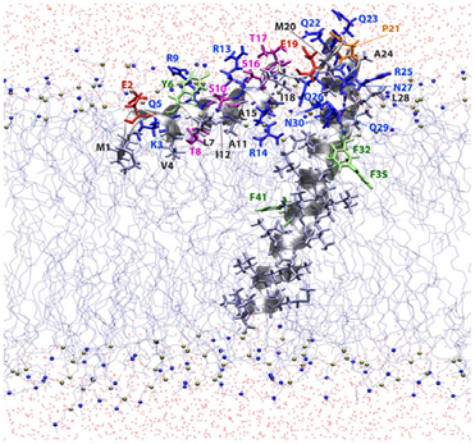

Figure 9: Structure of AFA-PLB in a lipid bilayer. High resolution structure of AFA-PLB in a lipid bilayer shows both secondary structure and topology. The cytoplasmic domain is partially buried in the lipid and makes a 102 ° angle with respect to the bilayer normal. The TM domain is a continuous helix and is tilted 24 degrees with respect to the membrane normal. Adapted from (*95*).

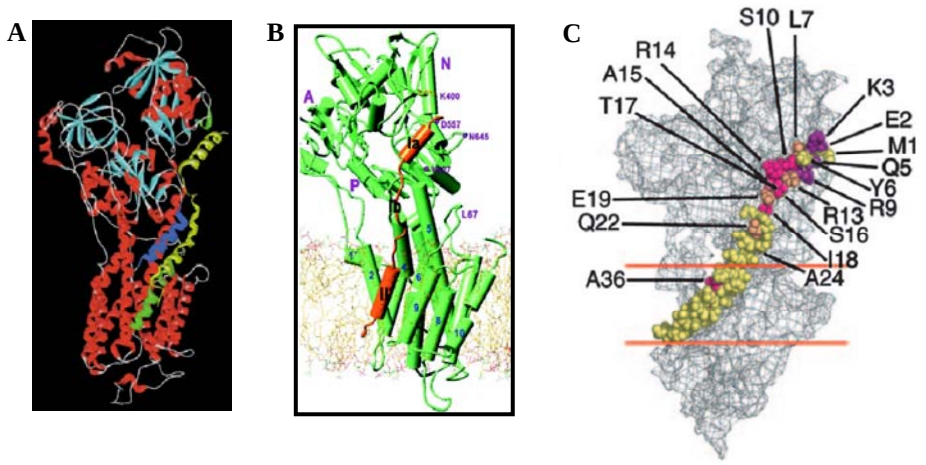

Figure 10: Models of the SERCA-PLB Complex. (A) Model of AFA-PLB (yellow) docked to E2 SERCA crystal structure (*96*). (B) Model of AFA-PLB (orange) docked into E2 SERCA (green) crystal structure (*74*). (C) Model of SERCA-PLB complex from (B). Colors other than yellow on PLB represent those amino acids affected by SERCA binding based on NMR experiments (*97*).

PLB binds and inhibits SERCA in cardiac tissues at submicromolar [Ca^{2+}]. This inhibition can be relieved by either increasing [Ca^{2+}] to micromolar or phosphorylation of PLB by PKA (*5, 11, 99*). It has been proposed that the relief of this inhibition requires complete dissociation of SERCA-PLB complex. This hypothesis was established based on a series of cross-linking studies that demonstrated PLB completely dissociated from SERCA under micromolar [Ca^{2+}], phosphorylation of PLB, and addition of a PLB antibody (*100, 101*). However, work from the Thomas lab revealed that PLB remained bound to SERCA when micromolar [Ca^{2+}] was added (*85, 102, 103*). Differences between these results were explained by uncontrolled [Ca^{2+}] concentration in the cross-linking studies (*103*). Currently, the mechanism of relief of inhibition is still contentious. Interestingly, the Na^+/K^+ ATPase (NKA), a relative of SERCA, has a regulatory subunit called phospholemman (PLM) that is also a single pass transmembrane protein (*104-106*). Like PLB, PLM binds and inhibits NKA. This inhibition is relieved by

phosphorylation of either S63 or S68 by PKA or PKC (*104, 107-109*). Based on these similarities and work in our lab and several others, the hypothesis is that PLB is essentially a subunit of SERCA (*85-87, 93, 103, 110, 111*), but more investigations are need to support this idea.

1.6. SERCA, PLB, and Disease

1.6.1 SERCA and Disease

Mutations within all SERCA isoforms have been linked to diseases, but none have been associated with heart disease. SERCA1a mutations lead to a condition called Brody's disease that causes severe muscle cramping due to difficulties with muscle relaxation (*112*). Lifespan of patients with Brody's disease are not affected due to the upregulation of SERCA2 isoforms, which help with muscle relaxation (*65*). Mutations within the SERCA2 gene that affect both SERCA2a and SERCA2b protein expression have been associated with a skin condition called Darier's disease that causes keratinization and loss of adhesion between epidermal cells. Like Brody's disease, Darier's disease does not affect lifespan or have any association with heart disease (*113*). SERCA3 mutations have been linked to type-II diabetes (*114*). Further studies using different SERCA null mice revealed roles for each SERCA isoforms. SERCA1a null mice yielded pups that survived birth but died shortly after due to severe respiratory stress (*115*). SERCA2 null mice produced offspring that did not survive birth because of its vital role in the heart and muscles (*116*). As for SERCA3 null mice, Liu *et al* did not see any phenotypic differences between the null mice and WT mice (*117*).

1.6.2. PLB and Cardiovascular Disease

In contrast to SERCA, PLB mutations have been associated with many different forms of cardiomyopathies in humans. The first discovery in a human was a missense mutation in PLB that changed Arg 9 to a Cys (R9C) (*119*). After generating a family tree, it was noted that this mutation lead to an autosomal dominant dilated cardiomyopathy and caused early death. These affected individuals carried one wild-type allele for WT-PLB and one allele for the R9C mutation. This mutation was characterized in HEK-293 cells transfected with R9C and in a transgenic mouse model. In living cells, experiments demonstrated that R9C PLB was not able to be phosphorylated by PKA leading to constant inhibition of SERCA by R9C (*119*).

A more recent study using FRET in living cells and biochemical assays revealed that R9C stabilizes the pentamer form of PLB preventing deoligomerization of the pentamer, and therefore, preventing the regulation of SERCA by the monomeric form of PLB (*120*). Ha et al also corroborated that PKA was unable to phosphorylate R9C PLB mutant (*120*). In the transgenic mice models, tests revealed decreased contractility, lethargy, and peripheral cyanosis. After death, autopsies disclosed the increase in heart size especially on the left side of the heart, characteristics of dilated cardiomyopathy (Figure 11).

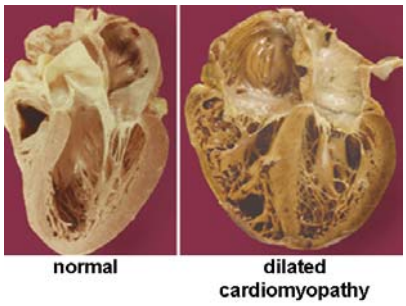

Figure 11: Cross-sectional view of normal and diseased states of the heart. Left ventricle and left atrium exposed from normal heart and hearts with dilated cardiomyopathy or familial hypertrophic cardiomyopathy (*118*).

Constant inhibition of SERCA by PLB leads to disease, but ablation of PLB also results in disease. A PLB-L39stop mutation produces a protein truncation in which the

first 39 amino acids are present (*121*). Affected individuals can be either heterozygous or homozygous leading to dilated cardiomyopathy. Since the majority of the transmembrane domain of PLB (amino acids 31-52) is missing, this PLB-L39stop does not properly insert itself into the SR membrane. Expression of this mutation in HEK-293 cells showed that PLB-L39stop was located in the plasma membrane and not the SR membrane. Therefore, PLB-L39stop was not inhibiting SERCA leading to a constitutively active SERCA, which results in cardiac disease at an early age (15-25 years) in humans, who are either heterozygous or homozygous for this mutation.

Unlike the previous mutations, deletion of Arg 14 in PLB (PLB-R14Δ) causes heart disease, mainly dilated cardiomyopathy, in older individuals (*122*). Using HEK 293 cells, researchers found that PLB-R14Δ was expressed and was able to be phosphorylated by PKA. Further experiments with transgenic mice revealed that the homozygous mice had dilated cardiomyopathy. The co-expression of PLB-R14Δ with WT PLB within the hearts of these mice led to super inhibition of SERCA meaning that SERCA's calcium affinity was significantly decreased and muscle contraction would be extended (*122*).

1.6.3. SERCA, PLB, and Treatments for Cardiovascular Disease

Cardiovascular disease is the leading cause of mortality worldwide. A major feature of cardiovascular disease, especially heart failure, is the mishandling of Ca^{2+} that may be explained by the relative abundance of SERCA-PLB in the heart (*7, 99, 123*). The result is that the intracellular [Ca^{2+}] is too high, preventing the heart from fully relaxing and consequently leading to a smaller contraction. Unfortunately, the existing

treatments only deal with the symptoms and do not directly address the root of the problem.

Newer approaches are focusing on utilizing recombinant associated adenosine vector (rAAV) to deliver either SERCA2a or pseudo-phosphorylated PLB to restore the SERCA-PLB ratio in the heart (*124*). Since it is known that SERCA2a expression is decreased in heart failure models (*125, 126*), clinical efforts to correct this imbalance were to deliver SERCA2a using rAAV in pigs. The results revealed that long-term expression of SERCA2a in the heart improved contractility (*127*). These positive findings led to a Phase 1 human clinical trial where patients showed improvements in a variety of heart failure parameters including diastolic and systolic functions (*128*). Another possible option is using rAAV to deliver a pseudo-phosphorylation PLB mimic, S16E. This procedure has been tried in both large and small heart failure animal models. In both cases, heart failure progression was reversed along with improved cardiac diastolic and systolic functions (*129-133*).

1.7 Aims

Aim 1: To investigate the molecular effectiveness gene therapy proposals for heart failure by using co-reconstitution of labeled SERCA, labeled WT-PLB, and unlabeled loss-of-function PLBs, S16E and L31A in functional and FRET assays. In large and small heart failure animal models, S16E, a phosphorylation mimic PLB mutant, has been delivered to the heart using rAAV and was shown to improve cardiac function (*129-133*). L31A is a transmembrane domain mutation that almost completely relieves SERCA inhibition (*134*). Functional and FRET data in Chapter 3 demonstrate that both LOF PLBs are able to maintain their ability to bind SERCA and compete both physically

and functionally with WT. These data support the efficacy of using S16E in gene therapy and demonstrate that other LOF PLBs may be used as well in gene therapy.

Aim 2: To probe nucleotide binding in SERCA with labeled SERCA and TNP-ADP, a fluorescent nucleotide, utilizing time-resolved FRET and transient time-resolved FRET. Based on kinetic studies and crystallography, it has been proposed that SERCA has two distinct modes of nucleotide binding. To examine this observation from the crystal to the functional SR membrane, we have performed time-resolved FRET to measure the distance between donor-labeled SERCA and the fluorescent nucleotide TNP-ADP, in the presence and absence of inhibitors. Transient time-resolved FRET was used to study the kinetics of this nucleotide binding in SERCA. Chapter 4 data confirm the existence of this novel nucleotide binding site in SERCA and show a biphasic reaction for nucleotide binding.

Aim 3: To determine the molecular signals for 20S proteasomal degradation using calmodulin as a model system. CaM variants were designed utilizing site-directed mutagenesis in order to perform site-specific oxidation of Met residues. Using circular dichroism, thermodynamic stability CD experiments, and proteasomal degradation assays, it was shown that oxidation of Met residues 51, 71, and 72 located in the N-terminus of CaM are essential for degradation. Functional data from ryanodine binding assays showed that oxidation of Met residues in the C-terminus of CaM completely abolished CaM's ability to bind and inhibit RyR. Accumulation of these CaM within the cell could be detrimental to CaM regulation of RyR impairing Ca^{2+} regulation during muscle contraction. These data are presented in Chapter 5.

CHAPTER 2 – Fluorescence Spectroscopy

2.1. Fluorescence Theory

Luminescence occurs when an electronically excited molecule emits a photon. It is divided into two processes, fluorescence (singlet excited state) and phosphorescence (triplet excited state). In both cases, a molecule absorbs a photon (*hv*) that excites an electron from the ground singlet state (S_0) to the first excited singlet state (S_1). The photon absorbed must have an energy that is equal to the energy gap between these two singlet states. Occasionally, the excited electron enters a higher vibrational energy level within the S_1 state. When this event occurs, the electron undergoes vibrational relaxation, a non-radiative process, in which the excited electron returns to the lowest vibrational

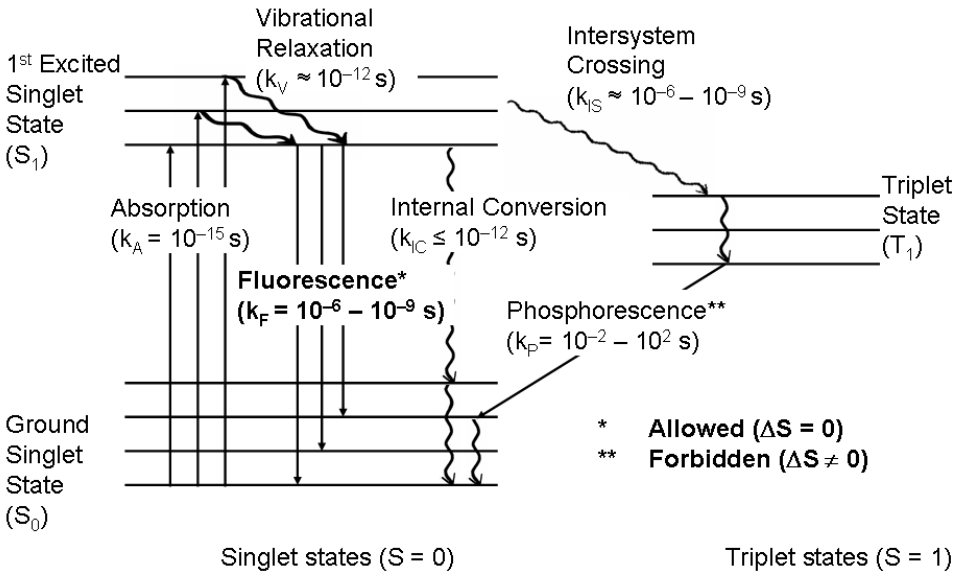

Figure 12: Jabloński diagram. Jabloński diagram illustrating energy transitions for a typical fluorescent molecule. Radiative transitions such as absorption or emission of photon are represented by straight lines. Non-radiative processes (relaxation or quenching) are depicted as wavy lines. Modified from (*135*) and Dr. David Thomas's lecture notes.

level within the S_1 state.

From this lowest vibrational level of the S_1 state, the electron can undergo multiple processes including fluorescence and phosphorescence to return to the ground state. Fluorescence occurs when an electron spontaneously emits energy as it returns to the S_0 state from the S_1 state. Since this process is allowed, it occurs on a timescale of nanoseconds to microseconds. In order for phosphorescence to happen, the excited electron must undergo a spin conversion into the first excited triplet state (T_1) known as intersystem crossing. Phosphorescence is the emission of a photon from T_1 and is a forbidden transition so it occurs on the millisecond to second time range. Another process that an excited electron can experience in order to return to the ground state is internal conversion. In this process, the excited electron emits thermal energy instead of a photon as it goes back to the ground state. This process has a timescale similar to fluorescence and usually occurs before emission of a photon. Other processes that are non-radiative, such as collisional quenching and fluorescence resonance energy transfer (FRET), also contribute to de-populating the excited state.

Both fluorescence and phosphorescence can be directly detected because they both involve emission of a photon. Non-radiative processes are studied through changes in emission intensity, which is directly proportional to the quantum yield of a fluorophore. The quantum yield of fluorescence (ϕ_F) is the probability that an excited fluorophore will emit a photon. It is defined as the number of photons emitted per photons absorbed, or the ratio the fluorescence rate constant (k_F) to the sum of fluorescent and non-radiative (k_{NR}) rate constants:

$$\phi_F = \frac{k_F}{(k_F + k_{NR})}. \qquad \textbf{Equation 1}$$

Since a fluorophore has invariable rate constant, changes in quantum yields are due to differences in non-radiative processes. These variations can be studied in the emission intensity in steady state and in the lifetimes in time-resolved fluorescence.

2.2. Fluorescence Resonance Energy Transfer

Fluorescence resonance energy transfer (FRET) is a non-radiative transfer of energy from an excited donor molecule to an acceptor molecule within a certain distance (R). This transfer of energy does not involve the emission or absorbance of a photon; it is caused by dipole-dipole interactions between the donor and acceptor molecules. In order for FRET to occur, the emission spectrum of the donor molecule must overlap with the absorption spectrum of the acceptor molecule. FRET is known as the "spectroscopic ruler" that is used to measure distances between proteins on a scale of 20-100 angstroms (*136*).

The rate of energy transfer (k_T) between a donor and acceptor at a certain distance (R) can be described by the Förster equation:

$$k_T = \frac{1}{\tau_D}\left(\frac{R_0}{R}\right)^6. \qquad \textbf{Equation 2}$$

Here, τ_D symbolizes the unquenched donor excited state lifetime, R represents the distance between the donor and acceptor probes, and R_0 is the Förster distance that is the distance (R) when the energy transfer efficiency (E) is 50%.

The Förster distance is defined as:

$$R_0 = 9{,}790\left(J\kappa^2\eta^{-4}\phi_D\right)^{1/6}. \qquad \textbf{Equation 3}$$

In this equation, , κ^2 is the orientation factor that relies on the orientation of the donor and acceptor transition dipoles and is assumed to be 2/3 for a random orientation, η

symbolizes the refractive index of the medium and is assumed to be 1.4 for aqueous solutions, ϕ_D is the quantum yield for the donor, and J is the integrated spectral overlap between the donor emission spectrum and the acceptor absorption spectrum. J is calculated by:

$$J(\lambda) = \frac{\int F_{\mathrm{D}}(\lambda)\, \varepsilon_A(\lambda)\, \lambda^4\, \mathrm{d}\lambda}{\int F_{\mathrm{D}}(\lambda)\, d\lambda}, \qquad \textbf{Equation 4}$$

where $F_D(\lambda)$ represents the donor emission spectrum and $\varepsilon_A(\lambda)$ symbolizes the acceptor absorption spectrum.

The energy transfer efficiency (E) is obtained from the ratio of transfer rate (k_T) to the total decay rate:

$$E = \frac{k_T}{(k_T + k_D)}, \qquad \textbf{Equation 5}$$

where k_D is the donor's rate decay. To relate E to distances, the Förster equation (Equation 2) is substituted into Equation 5to yield:

$$E = \frac{R_0^{\,6}}{R_0^{\,6} + R^6}. \qquad \textbf{Equation 6}$$

When R is equal to R_0, E is equal to 50%, which is optimal for measuring distances. E is most sensitive to R between 0.5 R_0 and 1.5 R_0.

E is also the fractional decrease of the donor emission (F_D) in the presence of the acceptor (F_{DA}) in steady state fluorescence or the fractional decrease of the donor decay (τ_D) in the presence of the acceptor (τ_{DA}) in time-resolved fluorescence:

$$E = 1 - \frac{F_{\mathrm{DA}}}{F_{\mathrm{D}}} = 1 - \frac{\tau_{\mathrm{DA}}}{\tau_{\mathrm{D}}}. \qquad \textbf{Equation 7}$$

2.3. Fluorescent Probes

To study the interaction between SERCA and PLB, extrinsic fluorescence probes were used to label specific sites on these proteins. Two fluorescent probes, 5-((((2-iodoacetyl)amino)ethyl)amino) naphthalene-1-sulfonic acid (IAEDANS) and 4-((4-(dimethylamino)phenyl)azo)-benzoic acid succinimidyl ester (Dabcyl-SE or Dabcyl), were chosen as the fluorescent donor and acceptor respectively (Figure 13). The spectral overlap between these probes is 32 Å meaning that these probes can detect distances between 16Å and 48 Å since the sensitivity range of FRET is given by $0.5R_0$ and $1.5R_0$ (Figure 14). At $R=R_0$, FRET is the most sensitive to changes in distances. Therefore, if PLB dissociates from SERCA, the energy transfer between these proteins will be zero because distance between the donor and acceptor is larger than their sensitive range.

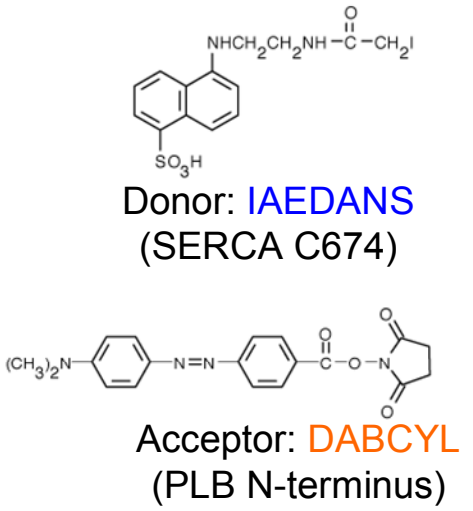

Figure 13: Fluorescent probes. Structures of IAEDANS and DABCYL fluorescent probes used as donor on SERCA and acceptor on PLB, respectively.

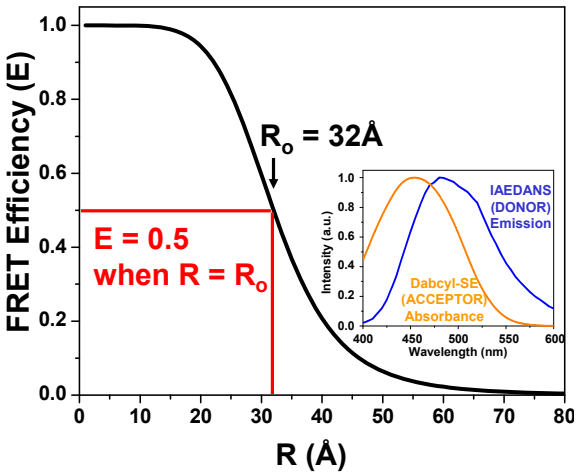

Figure 14: Sensitivity range of FRET probes, IAEDANS and DABCYL. Greatest sensitivity is seen at $R = R_0$. Inset of spectral overlap between IAEDANS emission and DABCYL absorbance.

SERCA was specifically labeled at Cys674 with IAEDANS through a covalent linkage between the thiol of Cys and the acetamide group of IAEDANS (Figure 15).

Specific labeling procedure can be found in Chapter 3. IAEDANS was selected due to its maximum excitation at 336 nm, which is optimal for the 355 nm laser on the time-resolved instrument, and its long fluorescent lifetime of 18 ns. In a FRET experiment where the efficiency = 50% and IAEDANS is the fluorescent donor, a 9 ns lifetime would be easily resolved from the donor only lifetime of 18 ns.

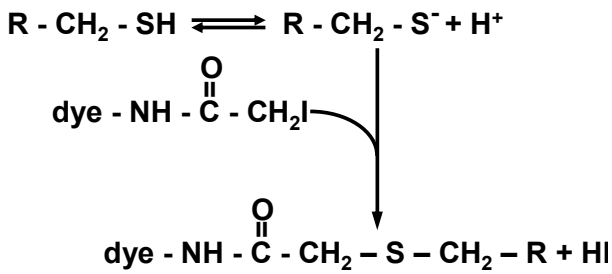

Figure 15: Reaction scheme of IAEDANS. Iodoacetamide group reacts specifically with the sulfonic anion of cysteine.

PLB was assembled on Fmoc-Leu-PEG-PS resin by Fmoc chemistry using a PE Biosystems PioneerTM peptide synthesis system, as previously reported (*103*). The *N*-terminal amino group was acetylated using acetic anhydride. For FRET, PLB was labeled with DABCYL-SE on Lys 3. DABCYL was chosen because it lacks fluorescence emission and, therefore, does not interfere with the donor emission signal. All synthetic PLBs were submitted to MALDI-TOF and amino acid analysis to confirm peptide composition and concentration. The purified PLBs were stored in methanol at –80°C until used for reconstitution. (Figure 16).

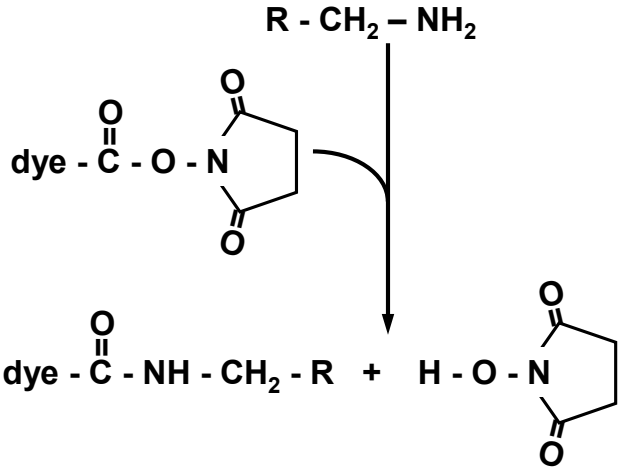

Figure 16: Reaction scheme of DABCYL. Succinimidyl ester reacts specifically with free amine groups.

2.4. Fluorescent Instrumentation

A common technique applied throughout this dissertation is fluorescence spectroscopy. Specifically, steady-state fluorescence, time-resolved fluorescence, and transient time-resolved fluorescence are used in this work. SS-fluorescence experiments in Chapter 5 are utilized to determine if hydrophobic regions of CaM get exposed after oxidation of methionines. SS-fluorescence experiments involving FRET are applied in Chapter 3 to screen potential PLB candidates for use in gene therapy. SS-fluorescence measures the average distances of each sample, but it cannot resolve different distances within a sample. However, TR-FRET is able to determine these different distances and different mole fractions associated with these distances. TR-FRET was required in Chapter 4 in order to determine if two different nucleotide binding sites exist in SERCA. Additionally, transient TR-FRET experiments were performed in Chapter 4 to test the kinetics of nucleotide binding in SERCA.

Steady-state Fluorescence. A Jobin-Evon Spex Fluoromax 2 was used to excite 1- anilinonaphthalene-8-sulfonate (ANS) at 372 nm and record the fluorescence emission from 450 nm – 600 nm after incubating CaM mutants with ANS. This instrument has a Xenon light source with adjustable slits to optimize the bandwidth. It also contained dual monochromators for 1 nm measurements during wavelength scanning.

Steady-state FRET. For steady-state FRET experiments, spectra were detected using a Gemini EM spectrofluorimeter microplate reader from Molecular Devices (Sunnyvale, CA). This instrument has a Xenon flash lamp (1 Joule/flash) and with dual monochromators in order to allow for 1 nm increment measurements during wavelength scanning. SERCA-PLB samples were pipetted into 384 well Greiner clear flat bottom

plate. AEDANS-SERCA was excited at 350 nm, and donor emission was recorded from 420-600 nm with 2 nm increments. Buffer background was subtracted from the experimental emission spectra. FRET was calculated by Equation 7.

Time-resolved FRET. Time-resolved fluorescence waveforms were recorded utilizing an instrument designed by the Thomas laboratory and Fluorescence Innovations, Inc (Bozeman, MT). In detailed, this instrument has a frequency-tripled neodymium-doped yttrium/aluminum garnet (Nd:YAG) pulsed laser that is utilized to excite AEDANS-SERCA at 355 nm. It also operates at a rate of 10 kHz with an Acqiris digitizer that acquires the entire fluorescence waveform after each laser shot, at a time resolution of 0.125 ns/data point. An instrument response function (IRF) was measured with a light scattering sample and was used in data analysis to determine fluorescence lifetimes in order to calculate the FRET efficiency.

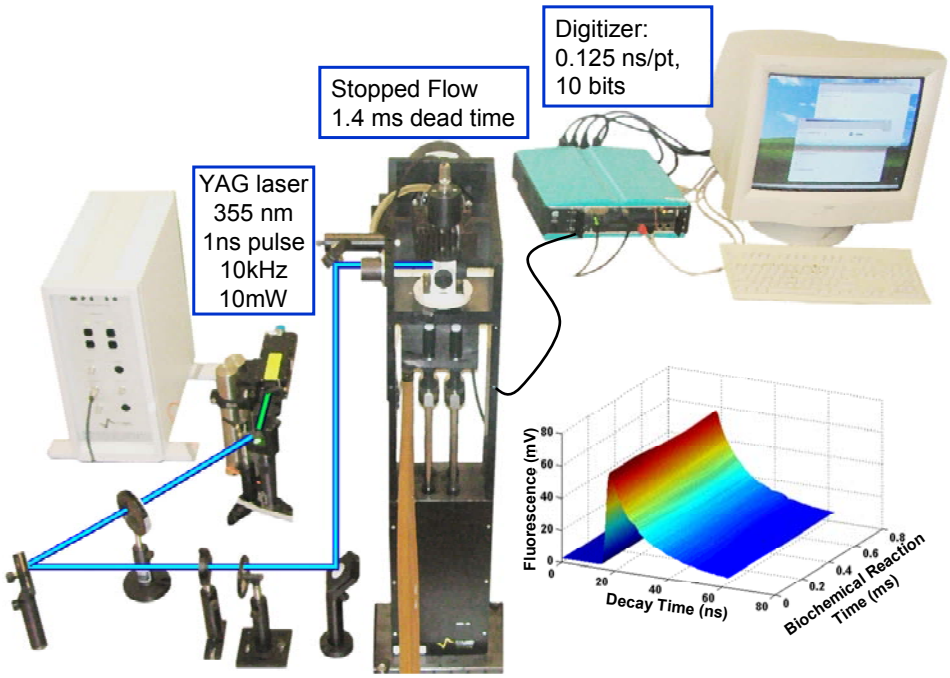

Figure 17: Transient time-resolved FRET instrumentation. Rapid mixing of IAEDANS-SERCA and TNP-ADP occurs and is excited at 355 nm by a Nd:YAG laser pulsing every 0.1 ms.

Transient time-resolved FRET. The same laser and digitizer were used here as in time-resolved FRET. However, the laser is aligned to hit a cuvette within a rapid mixing apparatus that is connected to two syringes, one with AEDANS-SERCA and the other with TNP-ADP (Figure 17). In the case of transient time-resolved measurements, a complete subnanosecond TR-FRET decay (from 0 to 60 ns after the pulse, 0.125 ns/data point) was recorded every 0.1 ms after rapid mixing of 10 μM AEDANS-SERCA and 30 μM TNP-ADP, which was averaged over five shots. One rapid mixing experiment takes about 1 s. This technology allowed us to capture structural data (e.g. inter-probe distance) with sub-millisecond time resolution.

CHAPTER 3 - Functional and Physical Competition between Phospholamban and its Mutants Provides Insight into the Molecular Mechanism of Gene Therapy for Heart Failure

Reprinted with permission from:

Elizabeth L. Lockamy, Razvan L. Cornea, Christine B. Karim, and David D. Thomas. Functional and Physical Competition between Phospholamban and its Mutants Provides Insight into the Molecular Mechanism of Gene Therapy for Heart Failure. *BBRC*, 2011; (408) 3; 388-392

Functional and Physical Competition between Phospholamban and its Mutants Provides Insight into the Molecular Mechanism of Gene Therapy for Heart Failure

Elizabeth L. Lockamy, Razvan L. Cornea, Christine B. Karim, and David D. Thomas*

Department of Biochemistry, Molecular Biology and Biophysics, University of Minnesota Medical School, Minneapolis, Minnesota 55455

Elizabeth L. Lockamy purified and labeled SERCA, performed all functional and FRET experiments, analyzed the data, and made all initial figures. I also wrote the original manuscript and edited the final copy. Razvan L. Cornea developed the equations 9, 10, 11, and 13 and simulated the data from these equations. He added these simulations to figures 18, 19, and 20. He designed experiments and assisted with writing and editing of the manuscript. Christine B. Karim synthesized and purified all PLB. David D. Thomas edited the final manuscript and contributed ideas to the project.

We have used functional co-reconstitution of purified sarcoplasmic reticulum (SR) Ca^{2+}-ATPase (SERCA) with phospholamban (PLB), its inhibitor in the heart, to test the hypothesis that loss-of-function (LOF) PLB mutants (PLB_M) can compete with wild-type PLB (PLB_W) to relieve SERCA inhibition. Co-reconstitution at varying PLB-to-SERCA ratios was conducted using synthetic PLB_W, gain-of-function mutant I40A, or LOF mutants S16E (phosphorylation mimic) or L31A. Inhibitory potency was defined as the fractional increase in K_{Ca}, measured from the Ca^{2+}-dependence of ATPase activity. At saturating PLB, the inhibitory potency of I40A was about three times that of PLB_W, while the potency of each of the LOF PLB_M was about one third that of PLB_W. However, there was no significant variation in the apparent SERCA affinity for these four PLB variants. When SERCA was co-reconstituted with mixtures of PLB_W and LOF PLB_M, inhibitory potency was reduced relative to that of PLB_W alone. Furthermore, FRET between donor-labeled SERCA and acceptor-labeled PLB_W was decreased by both (unlabeled) LOF PLB_M. These results show that LOF PLB_M can compete both physically and functionally with PLB_W, provide a rational explanation for the partial success of S16E-based gene therapy in animal models of heart failure, and establish a powerful platform for designing and testing more effective PLB_M targeted for gene therapy of heart failure in humans.

3.1. Introduction

Muscle relaxation occurs when the sarcoplasmic reticulum (SR) Ca^{2+}-ATPase (SERCA) hydrolyzes ATP and pumps Ca^{2+} from the sarcoplasm back into the SR against its concentration gradient. In the heart, SERCA activity is regulated by phospholamban (PLB), a single-span membrane protein that functions to inhibit SERCA by decreasing its apparent Ca-affinity (increasing K_{Ca}) (*137*). PLB inhibition of SERCA is relieved physiologically either by micromolar Ca^{2+} or by phosphorylation of PLB at Ser 16 by PKA (*5, 99, 138*), and can also be relieved by a number of point mutations (*134*), including S16E (a cytoplasmic domain mutation that partially mimics phosphorylation (*86*)) and L31A (a transmembrane domain mutation (*134*)).

Insufficient SERCA activity is a hallmark of heart failure (HF), which is a leading cause of hospitalization and death in most parts of the world (*123*), and overexpression of SERCA, using recombinant AAV vectors, has been shown to relieve heart failure in clinical trials (*124*). HF is associated with an increased ratio of PLB to SERCA (*7*), so the inhibitory interaction between SERCA and PLB has become an attractive therapeutic target (*99*). Indeed, interfering with the SERCA-PLB interaction in HF animal models can result in improved cardiac function (*129-133*). However, complete ablation of PLB can lead to premature death in humans (*121*), suggesting that a more subtle approach is needed.

Relief of PLB-dependent SERCA inhibition, whether by micromolar Ca^{2+}, PLB phosphorylation, or functional mutation in PLB, has long been thought to require dissociation of the SERCA-PLB complex (Figure 18A), a hypothesis supported primarily by cross-linking studies (*100, 101*). However, this hypothesis is inconsistent

with measurements of fluorescence resonance energy transfer (FRET) from SERCA to PLB that demonstrated no Ca^{2+}-dependence of SERCA-PLB affinity (*103*) and with intra-PLB FRET and electron paramagnetic resonance (EPR) studies that showed no SERCA-PLB dissociation by either Ca^{2+} or phosphorylation of PLB at S16 (*85, 102*), suggesting that PLB remains bound upon SERCA activation (Figure 18B). In addition, several loss-of-function (LOF, with less inhibitory potency than WT) PLB mutants have been shown to retain at least some SERCA binding affinity (*86, 87, 139*). These results suggest that it might be feasible to identify a LOF PLB mutant (denoted PLB_M below) with sufficient SERCA affinity to compete with WT (denoted PLB_W below) for SERCA binding, and that such a mutant would be a useful therapeutic reagent. Intriguingly, *in vivo* cardiac rAAV delivery of a gene corresponding to S16E, a pseudophosphorylated PLB mutant, prevents HF occurrence or progression in small and large animal models (*129, 131, 140*). To understand the molecular basis of the therapeutic effectiveness of S16E, we previously studied its structural dynamics, showing that the S16E mutation does not abolish SERCA binding, but it partially unfolds the cytoplasmic domain of PLB (detected by EPR and NMR) (*86, 87*), almost as much as is caused by phosphorylation at S16 (*85, 87, 110*). We suggest that S16E can relieve SERCA inhibition by competing with PLB_W for SERCA binding.

In the present study, we test this hypothesis directly and quantitatively by performing both FRET and functional assays on reconstituted membranes containing donor-labeled SERCA, acceptor-labeled PLB_W, and unlabeled S16E. We ask whether this LOF mutant of PLB can compete with the native WT for SERCA binding, which should reduce both FRET and inhibition (Figure 18C). We use a similar approach to evaluate the LOF PLB mutant L31A (*134*) as a phosphorylatable alternative to S16E. The results have important implications for future efforts in gene therapy.

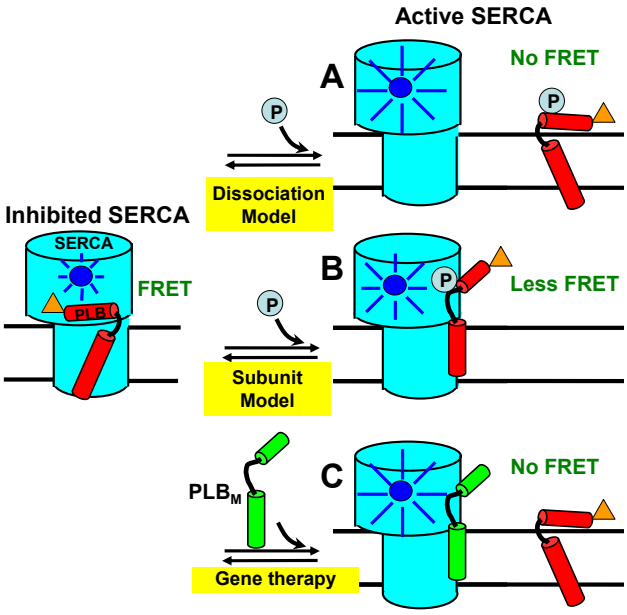

Figure 18: Models for relief of SERCA inhibition. Left: PLB_W binding to SERCA is detected when the fluorescence of donor (blue) on SERCA is quenched by the acceptor (orange) on PLB via FRET. (A) In the Dissociation Model, loss of function (e.g., due to phosphorylation) requires dissociation of the SERCA-PLB complex, which would completely eliminate FRET. (B) In the Subunit Model, inhibition can be relieved by a structural rearrangement, without dissociation of the SERCA-PLB complex. (C) For HF gene therapy applications, if a LOF mutant PLB_M has affinity for SERCA comparable to that of PLB_W, it can compete with PLB_W to increase SERCA function. These hypotheses can be tested by FRET.

3.2. Materials and Methods

3.2.1.. SERCA Purification and Labeling

SERCA was purified (*141*) and labeled with IAEDANS (*103*) as described previously. To determine the dye concentration in labeled samples, the absorbance (ε_{334nm} = 6100 M-1 cm-1) (*142*), was taken after treatment with 0.1M NaOH and 1% SDS. Samples of AEDANS-SERCA were flash-frozen and stored in the dark at -80°C until further usage.

3.2.2. Synthesis, Purification, and Labeling of PLB Mutants

PLB was assembled on Fmoc-Leu-PEG-PS resin by Fmoc chemistry using a PE Biosystems Pioneer™ peptide synthesis system, as previously reported (*103*). The *N*-terminal amino group of unlabeled PLBs was acetylated using acetic anhydride. For FRET, PLB_W was labeled at the N-terminus with the non-fluorescent acceptor Dabcyl-SE (denoted Dab-PLB_W). Peptide composition and concentration were confirmed by MALDI-TOF and amino acid analysis, and samples were stored in methanol at -20°C.

3.2.3. Co-reconstitution of SERCA and PLB

SERCA and PLB were co-reconstituted, as previously described (*143-145*), at 700 lipids/SERCA. Each sample contained 40μg of SERCA and varying amounts of PLB to obtain molar ratios of 0-20 PLB to SERCA. Ca^{2+}-ATPase activity and FRET measurements were performed immediately after co-reconstitution.

3.2.4. Ca^{2+}-ATPase Functional Measurements

Functional and FRET measurements were carried out at 25°C. ATPase activity was measured using an NADH-detecting enzyme-linked assay, as a function of [Ca^{2+}], in 96-well microtiter plates (*144, 146*). The time-dependence of absorbance at 340 nm was measured in a SpectraMaxPlus™ microplate reader (Molecular Devices, Sunnyvale, CA). Data were fitted using the Hill function:

$$V = V_{max}/[1+ 10^{-n\,(pKCa\,-\,pCa)}]\,, \qquad \text{Equation 8}$$

where V is the initial ATPase rate and n is the Hill coefficient. The inhibitory effect of each PLB variant was indicated by the observed increase in the apparent Ca^{2+}

dissociation constant K_{Ca}, measured relative to SERCA reconstituted in the absence of PLB.

Based on K_{Ca} measured as above, we define inhibitory potency, P, as the % increase in K_{Ca} (decrease in apparent Ca^{2+} affinity) caused by PLB:

$$P(n) = [K_{Ca}(n)/K_{Ca}(0) - 1]*100 \,, \qquad \text{Equation 9}$$

where n = PLB/SERCA.

To determine the apparent affinity of each PLB variant for SERCA, $P(n)$ data in Figure 19*B* were fitted using the specific binding function:

$$P(n) = P_{max}*n/(n + K_d) \,, \qquad \text{Equation 10}$$

where K_d is the apparent dissociation constant.

We assume that the effects of a mixture of PLB_W with a LOF PLB_M (Figure 20) on the SERCA K_{Ca} depends on the relative potencies and affinities of the PLB variants competing for a single inhibitory binding site on SERCA:

$$P(w+m)=\{[w*P(w)+A*m*P(m)]/(w+A*m)\} \,, \qquad \text{Equation 11}$$

where w = PLB_W/SERCA; m = PLB_M/SERCA; $A = K_d(PLB_W)/K_d(PLB_M)$.

3.2.5. Fluorescence Resonance Energy Transfer (FRET) Measurements

Fluorescence emission spectra were acquired using a Gemini EM microplate fluorimeter (Molecular Devices, Sunnyvale, CA) with excitation at 350 nm from a Xenon flash lamp (1 Joule/flash). Samples were plated in triplicate (75 μL per well) on 384-well, black wall, optical bottom well plates (Nalge Nunc International, Rochester, NY). Emission spectra were recorded in triplicate, from 420 nm to 600 nm, with a 2 nm step size, and a 420 nm long-pass emission filter. The fractional decrease in the integrated

fluorescence emission of the donor (AEDANS-SERCA) caused by the presence of an acceptor (Dab-PLB_W) is defined as the FRET efficiency $E = 1 - (F_{D+A}/F_D)$, where F_{D+A} and F_D are the fluorescence intensities in the presence and absence of acceptor. If the acceptor-labeled PLB binds to a single specific binding site with a dissociation constant K_d, then

$$E = E_{max}*[PLB]/(K_d + [PLB]) \quad , \qquad \text{Equation 12}$$

where E_{max} is the limiting value of E for the SERCA-PLB complex at saturation, and [PLB] and K_d are in 2-dimensional units, PLB per 1000 lipids (*103*). For convenience, titration curves are plotted below with units of PLB/SERCA on the abscissa, but the units are converted to PLB per 1000 lipids to calculate meaningful K_d values. In the competition experiments, when AEDANS-SERCA is co-reconstituted with Dab-PLB_W and unlabeled PLB_M, E depends on the relative affinities of the co-existing PLBs competing for binding to SERCA:

$$E(w+m) = w*E(w)/(w+A*m) \quad , \qquad \text{Equation 13}$$

where w, m, A, E are as defined as in Equation 11. Equation 13 is simpler than Equation 11 because PLB_M is unlabeled, so $E(m) = 0$.

3.3. Results

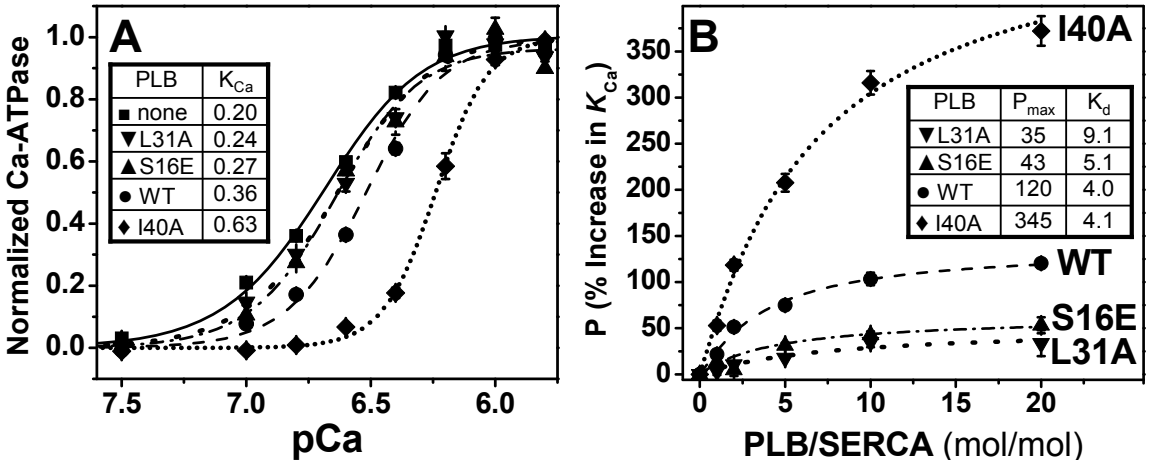

Figure 19: Effect of PLB mutants on the apparent Ca^{2+}-affinity of SERCA. (A) Ca^{2+} dependence of ATPase activity of SERCA reconstituted in lipid in the absence of PLB or in the presence of 5 moles of PLB per mole of SERCA. Activity is normalized relative to V_{max}, along with fits using the Hill function (Equation 8), with best-fit K_{Ca} (μM) values in inset table. (B) Dependence of PLB inhibitory potency (P, Equation 9) on PLB/SERCA, along with fits to the data using Equation 10, with best-fit P_{max} (%) and K_d (PLB/1000 lipids) values in inset table. Each plotted symbol represents mean ± SEM from at least three measurements.

3.3.1. Effects of Synthetic PLB and its Mutants on SERCA K_{Ca}

The effects of synthetic PLB variants on K_{Ca}, the apparent Ca^{2+}-affinity of SERCA, were determined in co-reconstituted samples of well-defined lipid/SERCA, and PLB/SERCA. At the approximately physiological level of 5PLB/SERCA (*147*), all PLB variants decrease the apparent Ca^{2+} affinity of SERCA (K_{Ca} values in Figure 19*A*). This pattern of potency is consistent with previous results using recombinant PLB variants (*86, 134, 144, 148, 149*); I40A inhibits much more than PLB_W, while S16E and L31A inhibit much less. While I40A is predominantly monomeric, the other three PLB variants have been shown to be primarily pentameric, (*134, 138, 150*), so loss of inhibitory function is not due to differences in PLB oligomeric stability.

To further characterize the inhibitory potencies of these PLB mutants, we performed co-reconstitution varying PLB/SERCA from 0 to 20 (maintaining 700 lipids/SERCA), thus probing the normal physiological range (PLB/SERCA ≤ 5), as well

as the pathophysiological range (PLB/SERCA > 5) that is often present in failing myocardium (*151, 152*). Potency profiles are given in Figure 19B, along with fits to Equation 10. As expected, the saturating potency, P_{max}, of I40A (345 ± 3%) is about 3 times that of PLB_W (120 ± 6%) (*134, 144, 148*), whereas both LOF PLB_M have P_{max} values about 3 times less than that of PLB_W (43 ± 7% for S16E, 35 ± 10% for L31A). Surprisingly, the apparent affinities of PLB_W and I40A for SERCA obtained from fitting their potency profiles in Figure 19B are not significantly different: K_d values (PLB/1000 lipids) are 4.1 ± 0.8 (PLB_W), 4.0 ± 0.4 (I40A), 5.1 ± 1.1 (S16E), and 9.1 ± 4.9 (L31A). We conclude that the differences in potency displayed by these PLB variants reflect mainly the intrinsic potency of the SERCA-PLB complex at saturation, P_{max}, not the binding affinity, $1/K_d$ (Equation 10).

3.3.2. Functional Competition between PLB_W and LOF PLB_M

To determine whether LOF PLB_M can attenuate the inhibition of SERCA induced by PLB_W, we co-reconstituted SERCA with mixtures of PLB_W and each of the LOF PLB_M (S16E and L31A). In Figure 20, triangles illustrate the measured potencies of SERCA/PLB_W/PLB_M mixtures at 1/2/2, 1/2/5, 1/5/5, and 1/5/10. Functional competition data are displayed relative to the inhibition profile of PLB_W from Figure 19B (as upper bound, Figure 20 dashed line) and an average of LOF PLB_M profiles from Figure 19B (as lower bound, Figure 20 dotted line). For each sample containing w PLB_W and m PLB_M mixtures, the increase in K_{Ca} is significantly smaller than for the corresponding reference samples containing only w PLB_W. This is the relevant effect for gene therapy applications. These experimental data, reflecting the functional competition of PLB_M with PLB_W for SERCA binding (Figure 20 symbols), were fitted using Equation 11, yielding apparent K_d values (PLB_M/1000 lipid) of 3.2 ± 0.5 for S16E and 3.5 ± 0.6 for L31A. These are similar to the K_d values measured directly from the functional potency profiles of these PLB_M (Figure 19B, Equation 10).

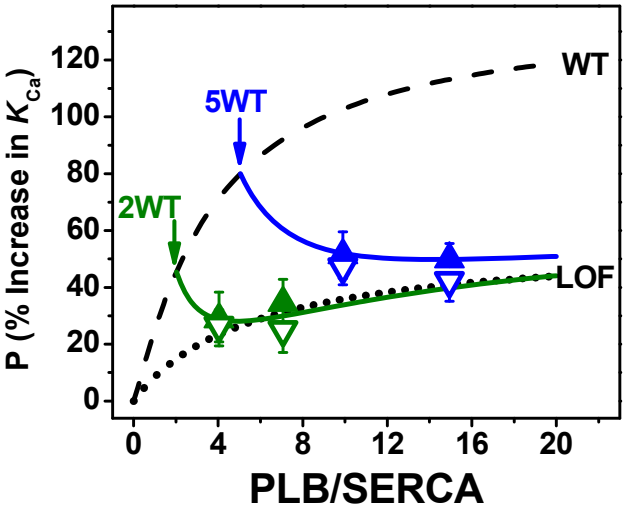

Figure 20: Functional competition. Effects of LOF PLB_M (S16E solid triangles, L31A open triangles) on inhibitory potency, P, in the presence of 2 (green) and 5 (blue) PLB_W/SERCA. Dashed curve: PLB_W-alone profile (from Figure 19B). Dotted curve: averaged LOF PLB_M profile (from Figure 19B). Solid curves represent fits to the competition data using Equation 11. Each plotted point is the mean ± SEM from at least three measurements.

3.3.3. FRET Measurement of Competition between PLB_W and LOF PLB_M

We measured FRET between AEDANS-SERCA and Dab-PLB_W co-reconstituted in lipid over a range of PLB/SERCA. Lipids/SERCA was fixed at 700. The resulting FRET profile (Figure 21, circles) allows a direct determination of PLB's binding affinity for SERCA, as previously shown (*103*). The dashed line represents the best fit to Equation 12, giving K_d = 1.2 ± 0.3 PLB/1000 lipids. This affinity is significantly tighter than indicated by the functional profile (Figure 19B, PLB_W), suggesting that some binding occurs without inhibition. To determine whether PLB_M and PLB_W physically compete for SERCA binding, we co-reconstituted AEDANS-SERCA, Dabcyl-PLB_W, and unlabeled LOF PLB_M at SERCA/PLB_W/PLB_M = 1/2/m (m= 2, 4, 8). As in the case of functional competition, FRET is decreased by both PLB_M (Figure 18, triangles are below circles), indicating competition with PLB_W for binding to SERCA. Thus, both unlabeled LOF mutants PLB_M compete physically with labeled PLB_W (Figure 21). These FRET competition data were fitted using Equation 13, yielding K_d values (PLB/1000 lipids) for the two PLB_M binding to SERCA that were indistinguishable: 1.8 ± 0.5 for S16E and 2.2 ± 0.8 for L31A.

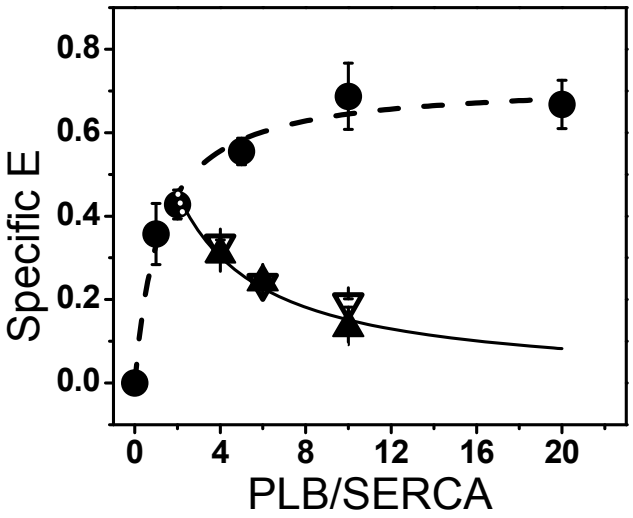

Figure 21: FRET Competition. The dependence of FRET $E(w)$ on the ratio w of Dab-PLB_W to AEDANS-SERCA (circles) was fitted using Equation 10 (dashed curve), giving K_d = 1.2 ± 0.3 PLB/1000 lipids. FRET competition data, $E(w+m)$, are shown for w = 2 Dab-PLB_W and m = 2, 4, or 8 unlabeled PLB_M (S16E closed triangles, L31A open triangles). Solid curve shows the best fit of the averaged PLB_M data to Equation 13, giving K_d = 2.0 ± 0.9 PLB/1000 lipids. Each plotted point represents the mean ± SEM from at least three measurements.

3.4. Discussion

By varying the molar ratio of PLB to SERCA and measuring the Ca^{2+}-dependence of SERCA activity, we found that the potency profiles, $P(n)$, of all four PLB variants are characterized by indistinguishable affinities ($1/K_d$), despite saturating potencies (P_{max}) that vary by a factor of 10 (I40A>>PLB_W>S16E>L31A) (Figure 19B). We conclude that, for these PLB variants, the inhibition in the SERCA-PLB complex at saturation (P_{max}) is essentially independent of affinity. This result suggests that the two LOF PLB_M should compete effectively with PLB_W for SERCA binding, thus relieving SERCA inhibition. The functional competition data (Figure 20) supports this hypothesis – both S16E and L31A compete effectively with PLB_W to decrease the net potency (shift in K_{Ca}). Indeed, the K_d values of S16E and L31A calculated from the functional competition measurements (3.2 ± 0.5 for S16E and 3.5 ± 0.6 from L31A, Figure 20) are even slightly smaller (greater affinity) than calculated from the potency profiles (5.1 ± 1.1 for S16E and 9.1 ± 4.9 for L31A, Figure 19B). The similar SERCA affinity of PLB_W and LOF PLB_M is further supported by the FRET data, which demonstrate physical competition between these PLB variants (Figure 21).

These results demonstrate that inhibitory potency of PLB_M is distinct from binding affinity and thus provide a rational explanation for the partial success of S16E-based gene therapy in animal models of heart failure (*129, 131, 140*). This work establishes a convenient, rapid FRET-based method for testing improved PLB_M candidates for HF therapies. Indeed, the L31A mutant may already be superior to S16E as a therapeutic candidate, because it can be phosphorylated by PKA at Ser 16, thus providing a level of adrenergic response that S16E lacks. Although the current collection

of PLB variants does not show significant variation in K_d, the observation that P_{max} is uncoupled from K_d supports the hypothesis that more LOF PLBs can be designed that have either (a) a lower P_{max} than S16E or L31A, without decreasing affinity, or (b) a higher affinity without increasing P_{max}. Indeed, previous studies with PLB mutants show that insight into structure-function correlations, gained from EPR and NMR analysis of PLB structural dynamics and function, can be used effectively to guide the PLB_M engineering process (*86, 87*).

CHAPTER 4 - Nucleotide Movement within SERCA Detected by FRET Resolved on the Nanosecond and Millisecond Time Scales

Elizabeth L. Lockamy purified and labeled SERCA, prepared all samples, performed all experiments, and analyzed data in and made Figures 23 and 24. David Kast assisted in transient time-resolved FRET experiments and fitted the data in order to determine a plausible model. He also made Figure 26 and 27. Bengt Svensson made Figure 21 and will be writing the manuscript. David D. Thomas assisted in developing experiments and how to fit the data.

4.1. Introduction

SERCA relaxes muscle by pumping Ca^{2+} from the cytosol to the lumen of the sarcoplasmic reticulum at the expense of ATP hydrolysis. The canonical binding mode for ATP, based on theE2P-AMPPCP.Tg crystal (PDB code 2C88) (*153*), has the adenine

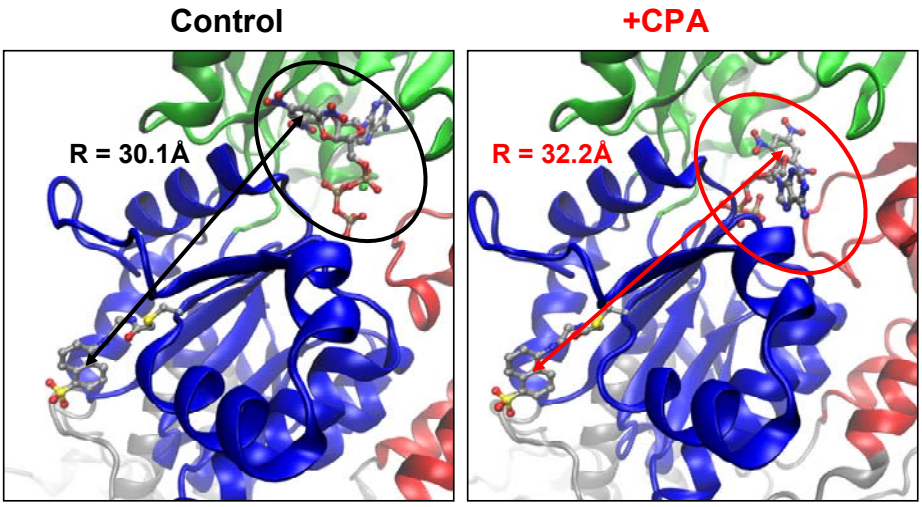

Figure 22: Two modes of nucleotide binding within SERCA. Left panel shows TNP-ADP, a fluorescent nucleotide, in the canonical binding position. Measured distance from TNP-ADP to the center of AEDANS is 30.1Å using PyMol (based on PDB 2C88) (*153*). Right panel depicts TNP-ADP in a new binding mode from the CPA crystal structure with a distance of 32.2Å from TNP-ADP to the center of AEDANS (based on PDB 2OA0) (*154*).

ring coordinated by F487, K515, and R560 of the P domain (Figure 22, left panel). Recently, a crystal structure of SERCA was reported in which the presence of cyclopiazonic acid (CPA), a toxin found in certain fungi that is an inhibitor of SERCA, produced a novel nucleotide binding mode where the adenine ring is between R489 and R678 of the N and P domains of SERCA, respectively (PDB code 2OA0) (Figure 22, right panel)(*154*).

To test if this binding site was induced by CPA, we have used functional sarcoplasmic reticulum membrane, where we have performed time-resolved FRET (TR-FRET) to measure the distance between C674 (labeled with the dye AEDANS) in the P domain and the fluorescent nucleotide TNP-ADP, in the presence and absence of CPA. Furthermore, we have tested the kinetics of TNP-ADP binding to SERCA using transient Time-Resolved FRET (TR^2-FRET). In these experiments, a complete subnanosecond TR-FRET decay (from 0 to 60 ns after the pulse) was recorded every 0.1 ms after rapid mixing of AEDANS-SERCA and TNP-ADP in a stopped-flow instrument. We observed a clear biphasic reaction with a fast component (260 s^{-1}, a rate constant proportional to nucleotide concentration, presumably representing the nucleotide binding reaction) and a slower component (17 s^{-1}) representing a conformational change within SERCA, that likely corresponds to the predicted nucleotide rearrangement. These results confirm that CPA changes the mode of nucleotide binding without perturbing the separation of the N and P domains of SERCA, consistent with the model based on the 2OA0 crystal structure. This new ATP binding mode, which is found in a third of all ATP-dependent proteins (*155, 156*), may play a critical role in the Ca^{2+}-ATPase reaction mechanism.

Only by simultaneously measuring fluorescent decays and biochemical kinetics can structure and function be connected.

4.2. Materials and Methods

Materials. Fluorescent probes, IAEDANS and 2'- *O*-(trinitrophenyl)adenosine 5'-diphosphate (TNP-ADP) were both purchased from Invitrogen. CPA and thapsigargin (TG) were bought from Sigma.

SERCA purification and labeling. SERCA was purified (*141*)and labeled (*103*) as previously reported. Dye concentration of labeled SERCA was determined using the absorbance of IAEDANS at 334 nm (ε_{334nm} = 6100 M^{-1} cm^{-1}) (*142*) after treatment with 0.1M NaOH and 1% SDS.

Sample preparation. Samples were prepared using 10 μM AEDANS-SERCA and 30 μM TNP-ADP. For equilibrium experiments, a range of TNP-ADP concentrations were utilized to determine the K_d of TNP-ADP. Samples containing 330 μM CPA and 30 μM thapsigargin (TG) were incubated for 20 minutes prior to measuring fluorescence. A higher concentration of CPA was used because it is a less specific inhibitor of SERCA than TG. Calcium concentration was kept constant at 210 μM Ca^{2+} using EGTA.

Time-resolved FRET. Time-resolved fluorescence decays were detected using a fluorometer from Fluorescence Innovations, Inc. (Bozeman, MT) as described in Chapter 2. Briefly, the instrument contained a Nd:YAG laser that operates at 10kHz and a digitizer that acquires entire fluorescence waveforms every 0.1 ms. Decays were analyzed using global nonlinear fits as described previously (*157, 158*). The instrument response function (IRF) was measured with water as a light-scattering sample. Data were fitted by Equation 14,

$$F_{D+A}(t) = (1-X_B)F_D(t) + X_B F_{DA}(t) \quad \text{Equation 14}$$

where F_D is the measured donor only waveform, F_{DA} is the measured donor with acceptor waveform, and X_B represents fraction bound. Fraction bound was then plotted as a function of acceptor concentration and fitted to a total binding curve,

$$y = y_{max}(x)/(x+K_d) + (x/K_{ns}) \quad \text{Equation 15}$$

where x is the concentration of TNP-ADP, y_{max} is the maximum limit of TNP-ADP bound, K_d is the apparent affinity of TNP-ADP for SERCA, and K_{ns} is the non-specific binding constant.

Transient time-resolved FRET. The same laser and digitizer were used here as in time-resolved FRET. However, the laser is aligned to hit a cuvette within a rapid mixing apparatus that is connected to two syringes, one with AEDANS-SERCA and the other with TNP-ADP. In the case of transient time-resolved measurements, a complete subnanosecond TR-FRET decay (from 0 to 60 ns after the pulse, 0.125 ns/data point) was recorded every 0.1 ms after rapid mixing of 10 μM AEDANS-SERCA and 30 μM TNP-ADP, which was averaged over five shots. One rapid mixing experiment takes about 1 s. This technology allowed us to capture structural data (e.g. inter-probe distance) with sub-millisecond time resolution.

4.3. Results

Effect of CPA on nucleotide binding. To investigate the effect of CPA on nucleotide binding, we utilized the fluorescent nucleotide, TNP-ADP, and TR-FRET. The control sample had a distance of 31Å while the CPA sample had a distance of 33Å (Figure 23). Both of these experimental distances are similar to the reported distances within their respective crystal structures. CPA induced at ~2Å increase in distance compared to the control, which is consistent with the effect seen crystal structure 2OA0 (*154*) compared to 2C88 (*153*). These data suggest that there is another binding state of SERCA and nucleotide.

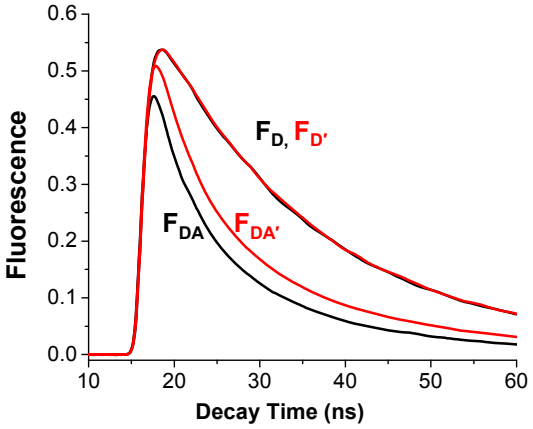

Sample	Xtal R (Å)	R (Å)
AE SERCA + TNP-ADP	30.1	31 ± 0.1
AE SERCA + TNP-ADP+ CPA	32.2	33 ± 1.2

Figure 23: TR-FRET from AE-SERCA to TNP-ADP in the presence of CPA. Waveforms for AE-SERCA only (FD) and AE-SERCA + CPA (FDA). Samples containing CPA are shown in red. Mean distance ± std. dev of n = 3 trials.

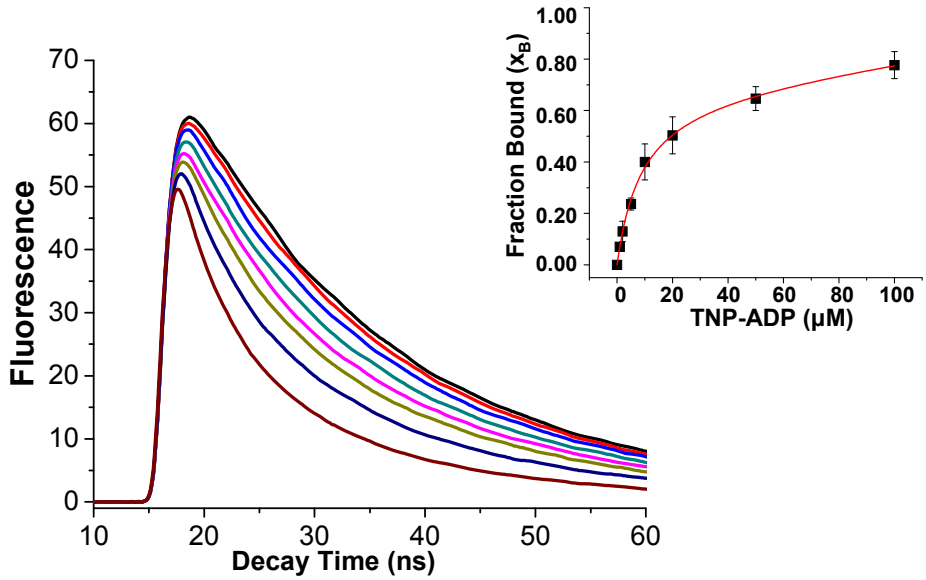

Figure 24: Equilibrium TR-FRET from AE-SERCA to TNP-ADP. Shown are measured waveforms containing increasing concentrations of TNP-ADP starting at the red waveform. Inset illustrates the fraction bound determined from global fitting the waveforms versus the concentration of TNP-ADP.

Equilibrium TR-FRET. Different concentrations of TNP-ADP were titrated into AEDANS-SERCA in order to establish the K_d values of the proposed two different binding sites. After globally fitting the waveforms, the fraction bound for each waveform was plotted versus the concentration of TNP-ADP. These data are the fraction of SERCA molecules with bound TNP-ADP and were fitted using a total binding equation (Equation 15). From this equation, we determined that the K_d for TNP-ADP to be 10 μM. If there are two binding sites, their K_d values are not distinguishable at equilibrium (Figure 24).

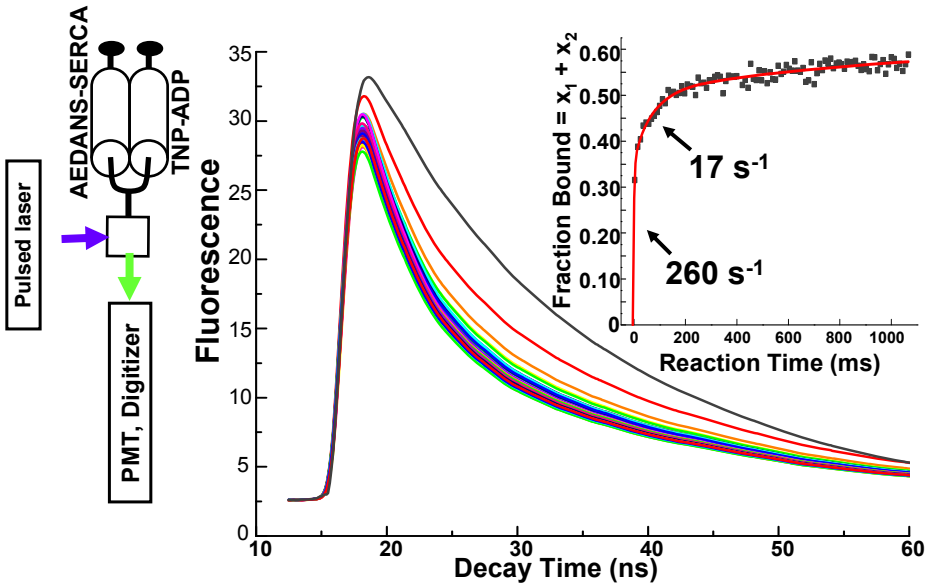

Figure 25: Transient TR-FRET from AE-SERCA to TNP-ADP. Rapid mixing of IAEDANS-SERCA and TNP-ADP occurs and is excited at 355 nm by a Nd:YAG laser pulsing every 1 ns. Gray waveform represents SERCA only. Colored waveforms represent the fluorescent decay collected sequentially after 10 ms of rapid mixing over the course of 1 second. Inset is the total fraction bound versus the reaction time in ms. A clear biphasic reaction is seen.

Transient time-resolved FRET. In order to resolve these two proposed binding modes, we used transient time-resolved FRET to determine both the distance and fraction bound. Because we can measure on the nanosecond time scale, we are able to ask whether these sites are resolved kinetically. AEDANS-SERCA and TNP-ADP were rapidly mixed and a measured waveform was measured every 0.1 ms. A biphasic reaction with a fast component (260 s^{-1}), presumably representing nucleotide binding, and a slow component (17s^{-1}) possibly representing a conformational change within SERCA (Figure 25 inset) were detected.

4.4. Discussion

Relationship between crystal structure and time-resolved fluorescence. The crystal structure containing CPA placed the nucleotide, ADP, within a novel binding mode. The adenine ring of ADP was sandwiched between two arginines, R489 and R678 of the N and P domains of SERCA, respectively (PDB code 2OA0) (Figure 22, right panel) (*154*). Time-resolved fluorescence experiments confirmed the existence of this nucleotide binding site (Figure 23). It was not an artifact of crystallization; it exists under physiological conditions. This binding mode is consistent with an adenine recognition motif found in about one-third of all ATP dependent proteins (*155, 156*). This year, Toyoshima et al determined the crystal structure of SERCA in the presence of TNP nucleotides including TNP-ADP (*159*). This crystal structure using the standard inhibitor, thapsigargin, showed that TNP-ADP was located between R489 and R678. Likewise, the other TNP nucleotides were bound in this fashion. This binding mode brings the γ-phosphate of ADP within 4.3Å of the residue Asp351 that is phosphorylated during SERCA's catalytic cycle (Figure 22, right panel). Compared with the 2C88 crystal structure (*153*) in Figure 22 (left panel) that has the γ-phosphate of ADP 9.0Å away from Asp351, this novel binding site is closer and helps explain how a reaction between ADP and Asp351 occurs, a crucial step in SERCA's enzymatic cycle.

Figure 26: Proposed model of nucleotide binding to SERCA. Plausible scheme involves a fast component representing when the nucleotide binds to SERCA given by ES and a slow component representing a conformational change within SERCA given by E*S.

Proposed Model of Binding. Transient time-resolved FRET experiments allowed us to resolve kinetically the proposed two binding modes. We observed a biphasic

reaction that begins with a fast component (260 s^{-1}), representing the nucleotide binding reaction (ES in Figure 26). The other component was slower (17 s^{-1}) representing a conformational change within SERCA, that likely corresponds to the predicted nucleotide rearrangement (E*S in Figure 26). These data verify that CPA traps the nucleotide in a novel binding site between two arginines, an established adenine recognition motif within other ATP-dependent proteins (*155, 156*), without perturbing the separation of the N and P domains of SERCA. These data are also consistent with the model based on crystal structures. This new ATP binding mode may be a crucial step in SERCA's enzymatic cycle bringing the γ-phosphate of ADP close enough to Asp351 for phosphorylation to take place.

CHAPTER 5 – Site-Specific Methionine Oxidation Initiates Calmodulin Degradation by the 20S Proteasome

5.1. Preface

My primary focus has been muscle relaxation studying the interaction between SERCA and PLB. Another project expanded my research into the field of proteasomal degradation using calmodulin, a calcium binding protein of ryanodine receptors, as a model system. Though the goal of this work was to determine the molecular signals that target a protein to the proteasome for degradation, this study has implications for Ca^{2+} regulation. Experiments included [^{3}H]ryanodine binding assays that were utilized to ascertain the functional consequence of CaM mutants. CaM binds and inhibits RyR channel opening, preventing the release of Ca^{2+}. Ryanodine binds specifically to open RyR channels with high affinity. By measuring the amount of [^{3}H]ryanodine bound to RyR, we were able to monitor the changes in the number of open receptors. We found that oxidation of the C-terminal methionines in CaM, which do not signal for proteasomal degradation, had a more deleterious effect on the RyR. Therefore, accumulation of these oxidized CaM could impair CaM regulation of RyR affecting Ca^{2+} equilibria during muscle contraction.

Edward M. Balog, Elizabeth L. Lockamy, David D. Thomas, and Deborah A. Ferrington. Site-Specific Methionine Oxidation Initiates Calmodulin Degradation by the 20S Proteasome. *Biochemistry*, 2009; (48) 13; 3005-3016.

SITE-SPECIFIC METHIONINE OXIDATION INITIATES CALMODULIN DEGRADATION BY THE 20S PROTEASOME †

Edward M. Balog [‡§], Elizabeth L. Lockamy [‡], David D. Thomas [‡], Deborah A. Ferrington [‖*]

From Department of Biochemistry, Molecular Biology and Biophysics[‡] and Department of Ophthalmology[‖],

University of Minnesota, Minneapolis, MN 55455

Elizabeth L. Lockamy designed and performed all proteasomal degradation assays, circular dichroism, thermal denaturation, fluorescence, and mass spectrometry experiments. In addition, I analyzed all data from above experiments and made Figures 27-32, 35 and Table 1 to report the results. I also wrote the methods and materials involving those experiments and edited the paper. Edward M. Balog designed and performed mutagenesis for each calmodulin (CaM) variant. He also characterized and analyzed the CaM mutants functional abilities as shown in Figure 33, Figure 34, and Table 2. He wrote the methods and materials section for the ryanodine binding (functional) experiments and the part of the discussion involving the significance of the

ryanodine binding. David D. Thomas aided in the design of thermal denaturation and circular dichroism experiments. He also wrote the abstract and edited the paper. Deborah A. Ferrington designed all experiments and performed statistical analysis on degradation experiments. She also wrote the Introduction, Results, and Discussion sections of the paper.

The proteasome is a key intracellular protease that regulates processes, such as signal transduction and protein quality control, through the selective degradation of specific proteins. Signals that target a protein for degradation, collectively known as degrons, have been defined for many proteins involved in cell signaling. However, the molecular signals involved in recognition and degradation of proteins damaged by oxidation have not been completely defined. The current study used biochemical and spectroscopic measurements to define the properties in calmodulin that initiate degradation by the 20S proteasome. Our experimental approach involved the generation of multiple calmodulin mutants with specific Met replaced by Leu. This strategy of site-directed mutagenesis permitted site-selective oxidation of Met to Met sulfoxide. We found that the oxidation-induced loss of secondary structure, as measured by circular dichroism, correlated with the rate of degradation for wild-type and mutants containing Leu substitutions in the C-terminus. However, no degradation was observed for mutants with Met to Leu substitution in the N-terminus, suggesting that oxidation-induced structural unfolding in the N-terminal region is essential for degradation by the 20S proteasome. Experiments comparing the thermodynamic stability of CaM mutants helped to further localize the critical site of oxidation-induced focal disruption to residues 51 and 72 in the N-terminal region. This work brings new biochemical and structural clarity to the concept of the degron, the portion of a protein that determines its susceptibility to degradation by the proteasome.

5.2. Introduction

The selective degradation of proteins by the proteasome is a key mechanism for regulating processes essential for cell survival. The proteolytic core of the proteasome, known as the 20S proteasome, is composed of four stacked rings of seven subunits each. The catalytic sites are sequestered within the core's interior, so proteins destined for degradation must first be unfolded to gain access to the catalytic sites. The functions of the 20S proteasome include both basal degradation of proteins containing an unfolded region inherent to their native conformation, e.g., p53, p21 ^{cip}, α-synuclein (*160*) and conditional degradation of proteins that contain an unfolded region induced by heat, stress, or mild oxidation (*161, 162*). The 26S proteasome, formed when the regulatory complex PA700 binds to the 20S catalytic core, recognizes and degrades both ubiquitin-modified (*163-165*) and some non-ubiquitinated (*166-170*) protein substrates. Selective destruction of proteins involved in cell signaling, cell cycle progression, and regulation of apoptosis are examples of processes controlled by the 26S proteasome (*164, 165*).

The ATP-independent degradation of proteins by the 20S proteasome has been suggested as the primary mechanism for degrading oxidized proteins following an oxidative insult (*162, 171*). The signals that target a protein for degradation, such as specific amino acid sequences or structural motifs that are revealed by oxidation-induced post-translational modifications, are collectively known as degrons. One well-described degron associated with the proteasome-dependent degradation of oxidized proteins is exposure of hydrophobic patches (*172-174*). However, this degron is not the universal signal for degradation of all oxidized proteins. For example, calmodulin (CaM) is one

oxidized protein that does not utilize this degron (*175*), suggesting that other molecular signals trigger degradation of this oxidized protein.

CaM is a ubiquitously expressed calcium-sensing protein that binds to and regulates over 100 distinct proteins, including calcium channels and pumps, kinases, phosphatases and transcription factors (*176*). Thus, regulation of cellular CaM levels is an important determinant in cell signaling. CaM's ability to regulate large numbers of molecules can be attributed to its unique structure, which consists of N- and C-globular domains connected by a flexible linker. Different environmental conditions (e.g., calcium concentration, pH, ionic strength) can alter CaM's conformation and change its affinity for select targets.

Previous work has demonstrated ubiquitin-independent degradation of CaM following *in vitro* oxidation or deamidation/isomerization of asparagines side-chains by both the 20S and 26S proteasomes, respectively (*169, 170, 175, 177, 178*). In our previous work using hydrogen peroxide to selectively oxidize Met in CaM to Met sulfoxide, we showed that the extent of *in vitro* oxidation of CaM correlates with both the rate at which CaM was degraded by the 20S proteasome and the degree of CaM structural unfolding (*175*). Others have also reported a strong correlation between CaM global structural rearrangement induced by oxidation and degradation by the 20S proteasome (*178*). These results suggest that a loss of native structure induced by oxidation could expose a degron, i.e., a specific sequence or structural motif, which signals degradation by the proteasome. Additionally, it is possible that oxidation of specific Met residues is required for this signal to become solvent exposed, triggering proteasome proteolysis.

A limitation of using peroxide to oxidize Met to Met sulfoxide is that a mixture of multiple oxidized species of CaM is generated (*175, 179*). An additional limitation of our previous work (*175*) was that we could not distinguish the specific site of oxidation. To overcome these limitations, the current study used site-directed mutagenesis, facilitating site-selective oxidation, to define the Met residues that are critical for signaling proteasome degradation. We show that oxidation of N-terminal Met residues 51, 71, and 72 are essential for degradation by the 20S proteasome, suggesting the presence of a putative degron in CaM's N-terminus.

5.3. Materials and Methods

Materials- Pigs were obtained from the University of Minnesota Experimental Farm and from Clemson University Research Farm Services. The Quick Change Site-Directed Mutagenesis Kit was purchased from Stratagene (LaJolla, CA). Fluorescamine was purchased from Sigma. 1-Anilinonaphthalene-8-sulfonate (ANS) was obtained from Molecular Probes (Eugene, OR). The bicinchoninic acid protein assay kit (BCA) was from Pierce (Rockford, IL). [^{3}H]Ryanodine was purchased from PerkinElmer Life Sciences (Waltham, MA). Unlabeled ryanodine was obtained from Calbiochem (La Jolla, CA). Adenosine 5'-(β,γ-imido)triphosphate tetralithium salt (AMPPNP) was from Sigma (St. Louis, MO). All other reagents were HPLC grade or better.

Purification of 20 S Proteasome- The 20S proteasome was purified from frozen rat liver as previously described (*175*). Samples were stored in 10 mM Tris and 200 mM KCl (pH 7.5) at -80ºC. Protein concentrations were determined using the BCA assay with bovine serum albumin as the protein standard. The purity of 20S proteasome preparations, which includes HSP90, was similar to previous reports (*175, 177*).

Site-directed Mutagenesis of CaM- Seven CaM mutants were generated, in which different combinations of Met were mutated to Leu. The nomenclature for the mutants indicates the number of Leu substitutions and their position within the protein (Figure 27). Mutants were constructed from the wild-type (WT) rat CaM cDNA by using primer-based site-directed mutagenesis following the protocol provided by Stratagene's Quick Change Site-Directed Mutagenesis Kit (LaJolla, CA). DNA sequence analysis, performed at the DNA Sequencing and Analysis Facility (University of Minnesota, Minneapolis, MN), confirmed the correct sequence for each mutant.

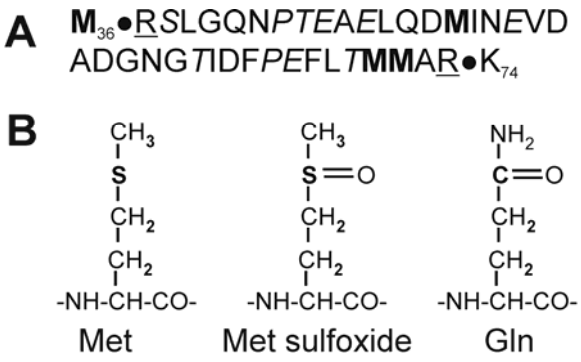

C

	PEST								
Sample	36	51	71	72	76	109	124	144	145
WT	M	M	M	M	M	M	M	M	M
L9	L	L	L	L	L	L	L	L	L
*L3PEST	M	L	L	L	M	M	M	M	M
L6NP	L	M	M	M	L	L	L	L	L
*L6CTNPP	L	L	L	L	L	L	M	M	M
L3CTPP	M	M	M	M	M	M	L	L	L
*L5NTerm	L	L	L	L	L	M	M	M	M
L4CTerm	M	M	M	M	M	L	L	L	L

Figure 27: Diagram of proposed PEST sequence and CaM mutants. (A) Putative PEST sequence in CaM (amino acids 37-73), includes Pro, Glu, Ser, or Thr (in italics), and is flanked by charged amino acids (underlined). (B) Structures of Met and derivatives. (C) CaM mutants; numbers indicate the positions of nine Met present in WT CaM. Amino acids 51, 71, 72 are located within the putative PEST sequence. Mutant names reflect the number of Leu substitutions and the relative position of the mutation: all 9 Met mutated (L9), mutation of 51, 71, 72 (L3 PEST), mutation of all non-PEST Met (L6 NP); mutation of all Met in the N-terminus (L5 NTerm) or C-Terminus (L4 CTerm). C Terminal "Pseudo-PEST" (L3 CTPP) indicates mutation of the C-terminal Met (124, 144, 145) that are analogous to the N-terminal PEST sequence. Mutation of all Met except 124, 144, 145 is designated as C Terminal Non-"Pseudo-PEST" (L6 CTNPP). *PEST region mutants contain Met to Leu substitutions for amino acids 51, 71, and 72.

Expression and Purification of WT and Mutant CaM- CaM was expressed in *E. coli* (BL21(DE3)pLys5), purified via phenyl-Sepharose chromatography (*180*), and dialyzed overnight at 4ºC against 2 mM HEPES (pH 7.0). Protein concentration was determined using the Micro BCA protein assay using wild-type CaM as the protein standard. The concentration of the CaM standard was determined using the published

molar extinction coefficient, $\varepsilon_{277\text{-}320\ nm} = 3{,}029\ M^{-1}\ cm^{-1}$ (*181*). The purity of the preparations was confirmed by a single protein band on Coomassie blue-stained gels that migrates at ~16 kDa.

Mass Spectrometric Analysis- Matrix-assisted laser desorption ionization time-of-flight (MALDI-TOF) mass spectrometry was used to determine the masses of non-oxidized and oxidized mutants. Prior to analysis, samples were desalted using Millipore C4 ZipTips as instructed by the manufacturer's protocol. Molecular mass was determined using a Bruker Biflex III Mass Spectrometer (Bruker Daltonics, Billerica, MA) and α-cyano-4-hydroxycinnamic acid as the matrix.

CaM Oxidation- Met in CaM were selectively oxidized by incubating 60 μM CaM (1 mg/mL) in 50mM HOMOPIPES (pH 5.0), 0.1 M KCl, 1 mM $MgCl_2$, and 0.1 mM $CaCl_2$ with 50mM H_2O_2 at 25°C for 24 hr (*16*). To stop the reaction, the sample was dialyzed (MWCO = 1,000 kDa) overnight at 4°C in distilled water buffered with 1 mM ammonium bicarbonate (pH 7.7).

Circular Dichroism (CD) Spectroscopy of CaM- CD spectra were recorded from 250 to 200 nm using a JASCO J-710 spectrophotometer and a temperature-jacketed spectral cell with a path length of 0.1 mm. Spectra were recorded at 1 nm intervals for CaM (50 μM) in 50 mM Tris (pH 7.5), 100 mM KCl, 10 mM $MgCl_2$, 1mM EGTA, and 600 μM $CaCl_2$ at 37°C. Two separate measurements were performed on each sample. CD spectra were analyzed based on the standard assumption that the CD spectrum is a linear combination of contributions from three discrete secondary structural populations,

$$E(\lambda) = x_\alpha E_\alpha(\lambda) + x_\beta E_\beta(\lambda) + x_R E_R(\lambda) \qquad \textbf{Equation 16}$$

where E is the molar ellipticity per residue, and x_i and $E_i(\lambda)$ are the mole fraction and molar ellipticity, respectively, of residues in α helix, β sheet, and random coil (*182, 183*). Specifically, at 208 nm and 222 nm (*184*),

$$E(208\text{ nm}) = -32\,x_\alpha - 4\,x_\beta - 4\,x_\beta \qquad \textbf{Equation 16}$$

$$E(222\text{ nm}) = -36\,x_\alpha - 14\,x_\beta + 6\,x_\beta$$

But $x_B = 0$ for CaM (*184*), so Equation 16 reduces to

$$x_\alpha = (6R - 4)/(42R + 28), \qquad \textbf{Equation 17}$$

where R = E(208 nm)/E(222 nm) and x_α is the α-helical content. Data are expressed as mean ± SD.

Thermal Denaturation Experiments- Thermal denaturation experiments were performed using a JASCO J-815 spectrophotometer with an automated temperature controller. Samples had a concentration of 10 μM in 50 mM Tris (pH 7.5), 100 mM KCl, 10 mM $MgCl_2$, 1mM EGTA, and 600 μM $CaCl_2$ in a cuvette with a path length of 1.0 mm. Samples were heated from 10°C to 90°C at a rate of 2°C/min, then cooled from 90°C to 10°C. Ellipticity was recorded at 222 nm at one degree increments. A minimum of two separate measurements was performed on each sample.

Analysis of Hydrophobicity of Oxidized CaM- The surface hydrophobicity of CaM was evaluated from fluorescence enhancement of ANS. CaM (180 nM) was incubated at 37°C in 50 mM HEPES, 100 mM KCl, 10 mM $MgCl_2$, 1mM EGTA, and 600 μM $CaCl_2$ for 30 min with 16-fold molar excess of ANS. Fluorescence emission spectra, with excitation at 372 nm, were recorded from 450 nm to 600 nm with a Jobin-Evon Spex Fluoromax-2. Hydrophobicity was defined as the increase in integrated fluorescence

intensity due to addition of CaM, normalized to WT. Four separate measurements were performed on each sample. Data are expressed as mean ± SD.

CaM Proteolysis by the 20S Proteasome- The rate of proteolysis using CaM as the substrate was determined using fluorescamine, which forms a fluorescent adduct with the amino termni of peptides released by proteasome cleavage of CaM (*177*). CaM (31.5 nM) was incubated at 37°C in 50 mM HEPES, 100 mM KCl, 10 mM $MgCl_2$, 1mM EGTA, 600 μM $CaCl_2$ and 1.5 nM 20S proteasome. Aliquots were removed every minute for 5 min. Measurement of the fluorescent adducts was performed in a Cytofluor 4000 Multiwell Plate Reader (ex=360 nm; em=460 nm). The concentration of peptides hydrolyzed was determined by comparing the linear response of sample fluorescence with the fluorescence of a glycine standard curve. The rate of CaM degradation was linear with respect to proteasome concentration.

[^{3}H]Ryanodine Binding to Skeletal Muscle Heavy Sarcoplasmic Reticulum (HSR)- Skeletal muscle HSR vesicles were prepared from porcine longissimus dorsi muscle and [^{3}H] Ryanodine binding was performed as described previously (*185*). Ryanodine binds to the open RyR with high affinity and specificity and is therefore a sensitive indicator of channel activity (*186, 187*). HSR vesicles (0.2 mg/ml) were incubated for 90 min at 37°C in medium containing 120 mM potassium propionate, 10 mM PIPES, pH 7.0, 1.5 mM AMPPNP, 100 nM [^{3}H]ryanodine, and a Ca-EGTA buffer set to give the desired free Ca^{2+} concentration (*188*). HSR vesicles were then collected on Whatman GF/B filters and washed with 8 ml of ice-cold 100 mM KCl buffer. Radioactivity retained by the filters was determined by liquid scintillation counting. Estimates of maximal [^{3}H]ryanodine binding capacity of each HSR vesicle preparation were determined in medium that in

addition contained 500 mM KCl, 5 mM ATP, and 100 μM Ca^{2+}. Nonspecific binding was measured in the presence of 20 μM nonradioactive ryanodine. [^{3}H]Ryanodine binding is expressed as a percent of maximal [^{3}H]ryanodine binding. The CaM concentration dependence of SR vesicle [^{3}H]ryanodine binding was fit with a four parameter Hill equation using SigmaPlot 9.0 (Systat Software, Point Richmond, CA). Data are presented as means±S.E.

Statistical Analysis- Degradation rates were compared for oxidized and non-oxidized samples using a Student's t-test. Linear regression analysis was performed to test the relationship between (i) α-helical content and the number of substitutions, (ii) degradation rate and α-helical content or (iii) degradation rate and ANS binding. Student's t-test and linear regression were performed using the statistical software in Origin 7.5 (Microcal). Parameters derived from the Hill equation fit to [^{3}H]ryanodine binding data were compared using a one-way analysis of variance with a Holm-Sidak multiple comparison as a *post-hoc* test. Statistical analysis was performed using SigmaStat 3.1 (Systat Software, Point Richmond, CA). Statistical significance was set at $p<0.05$. Results are expressed as mean ± SEM unless otherwise specified.

5.4. Results

Description and Rationale for CaM Mutants- CaM contains nine Met that can be oxidized to Met sulfoxide. Previous work has shown that the extent of *in vitro* oxidation of CaM using hydrogen peroxide correlates with both the rate of CaM degradation by the 20S proteasome and the degree of CaM structural unfolding (*175*). These results suggest that loss of secondary structure induced by oxidation could unmask a specific sequence or structural motif that signals degradation by the proteasome. One well-characterized

degradation signal, also known as a degron, is the PEST sequence. This degron is defined by the inclusion or exclusion of specific amino acids and the sequence hydrophobicity (*189*). The PEST sequence includes the amino acids Pro, Glu, Asp, Ser, and Thr that are flanked by positively charged amino acids; Lys and Arg are not permitted within the sequence. As determined using the PEST algorithm (https://emb1.bcc.univie.ac.at./toolbox/pestfind/), CaM contains a poor PEST sequence (score = -3.07, where positive scores indicate potential PEST sequences) within residues 37 to 73 (Figure 27A). Considering the structural and chemical similarities between Met sulfoxide and glutamine (Figure 27B), we substituted glutamine for Met (residues 51, 71, 72) and found that the PEST score improved to -0.33. It is likely that presence of an oxygen on the side chain alters the hydrophobicity of the sequence, making it a stronger PEST degron. Thus, we hypothesize that the oxidation of Met within the putative N-terminal degron will cause conformational unmasking of a signal that elicits degradation by the proteasome.

A limitation of using peroxide to oxidize Met to Met sulfoxide is that a mixture of multiple oxidized species of CaM is generated (*175*), thus complicating identification of key Met. To overcome this limitation, site-directed mutagenesis and site-specific oxidation were used to define the Met residues that are critical for eliciting proteasome degradation. Figure 27C defines the site of Met to Leu substitutions for the seven mutants that were studied. (See also Figure 27 legend for explanation of the nomenclature. Note that the nomenclature utilizes “PEST” as an indication of the position of Met mutations in relation to residues 37-73 in the N-terminus. However, we are not inferring that this region contains a legitimate (confirmed) PEST sequence.) Of

particular importance are the mutants containing Leu substitutions in positions 51, 71, 72, which prevent oxidation in the putative PEST region of the protein. These mutants (L3 PEST, L6 CTNPP, L5 NTerm) are referred to as the PEST-region mutants. The reciprocal mutants (L6 NP, L3 CTPP, L4 CTerm) were generated for each PEST-region mutant as negative controls and contain oxidizable Met in the PEST region. The Met in positions 124, 144, and 145 are located within the C-terminal EF-hand at approximately the same position as Met 51, 71, and 72 that are within the N-terminal EF-hand. We refer to the sequence containing Met 124, 144, 145 as the "Pseudo-PEST" sequence because it is the positional correlate to the PEST sequence in the N-terminus. However, the "Pseudo-PEST" sequence does not contain a putative PEST degron. Also included in the analysis are the two extremes; WT containing no substitutions and L9, where all 9 Met are mutated to Leu.

Characterization of CaM mutants- Analysis of the DNA sequence for each CaM mutant confirmed that the planned mutations were correctly generated (data not shown). Mass spectrometry was used to determine the molecular mass for WT and CaM mutants. WT CaM exhibits a single major peak at 16702 ± 1 Da, which is in close agreement with the experimental molecular mass for rat CaM (16706 Da) (Table 1).

Table 1: Characterization of CaM Mutants.

	Molecular Mass [b]					α-Helix Content [c]			Hydrophobicity [d]	
	Non-oxidized			Oxidized						
Sample[a]	Theor	Exper	Er(%)	Theor	Exper	Er(%)	Non-ox	Ox	Dif(%)	ANS Binding
Wt	16706	16702	0.03				63 ± 2		71	0.99 ± 0.02
Ox Wt				16850	16846	0.02		18 ± 1		1.00
L9	16544	16552	0.05	16544	16558	0.08	52 ± 2	53 ± 1	0	1.05 ± 0.02
L3 PEST [e]	16652	16645	0.04	16748	16751	0.02	61 ± 1	43 ± 3	30	0.88 ± 0.03
L6 NP	16598	16589	0.05	16646	16645	0.01	58 ± 4	43 ± 1	41	0.96 ± 0.00
L6 CTNPP [e]	16598	16608	0.06	16646	16654	0.05	55 ± 1	48 ± 1	15	1.09 ± 0.06
L3 CTPP	16652	16666	0.08	16748	16754	0.04	65 ± 1	30 ± 1	54	0.94 ± 0.05
L5 NTerm [e]	16616	16612	0.02	16680	16681	0.01	61 ± 1	47 ± 1	25	0.97 ± 0.02
L4 CTerm	16634	16628	0.04	16714	16711	0.02	60 ± 1	29 ± 1	52	0.96 ± 0.03

[a] Nomenclature reflects the number and location of Met to Leu substitutions. See Figure 27 for description. [b] Theoretical molecular mass was based on the sequence for CaM from rat (P62161, Swiss Prot) and the loss of 18 daltons for each Met to Leu substitutions. Theoretical mass of oxidized samples includes the addition of one oxygen (+16 daltons) for each Met. Experimental molecular mass was determined using MALDI-TOF mass spectrometry. The percent error was calculated by [(Exp MW – Theoret MW)/ Theoret MW] *100 . [c] α-helix content was calculated from the ratio of ellipticity at 208 and 222 nm, measured by CD spectroscopy. Values are mean ± SD of two separate measures for each sample. The percent difference (Dif) in α-helix content due to oxidation was calculated as (1-(oxidized/non-oxidized)) for each sample. [d] Hydrophobicity of oxidized samples was estimated from fluorescence of ANS binding. All values were normalized to Ox Wt for each trial. Values are mean ± SD of two separate measures for each sample. [e] PEST-region mutants.

Each of the unoxidized CaM mutants exhibited a single major peak that closely matched the theoretical mass; the average percent difference was 0.04±0.006%. Using experimental conditions where complete hydrogen peroxide-induced oxidation of Met to Met sulfoxide was achieved, there was a shift in the single major peak that corresponded to the addition of one oxygen (+16 daltons) for each Met present in the sequence. For example, oxidation of WT CaM resulted in the addition of 144 Da. In contrast, replacement of all Met with Leu (L9) resulted in no oxidation-dependent change in mass. The average percent difference comparing theoretical with experimentally measured masses for oxidized samples was 0.03±0.006%.

Circular dichroism (CD) spectroscopy was performed to evaluate changes in secondary structure due to either the Met to Leu substitutions or site-specific oxidation. Under our experimental conditions, WT CaM contains ~63% α-helix (Table 1). For the non-oxidized mutants, three to five substitutions had no effect on the α-helix content, whereas a minor loss in α-helix content was observed for mutants containing six or nine substitutions. With oxidation by hydrogen peroxide, all samples except L9 demonstrated a loss in secondary structure that correlated with the number of Met to Leu substitutions (Table 1, Figure 28). These results confirm that Met oxidation disrupts the secondary structure of CaM and that the decrease in α-helical content depends on the extent of Met oxidation. Of note, preventing oxidation of Met in the PEST region via their substitution to Leu, i.e., the PEST-region mutants, resulted in a loss in secondary structure that was similar to the reciprocal mutants containing an equivalent number of Met substitutions.

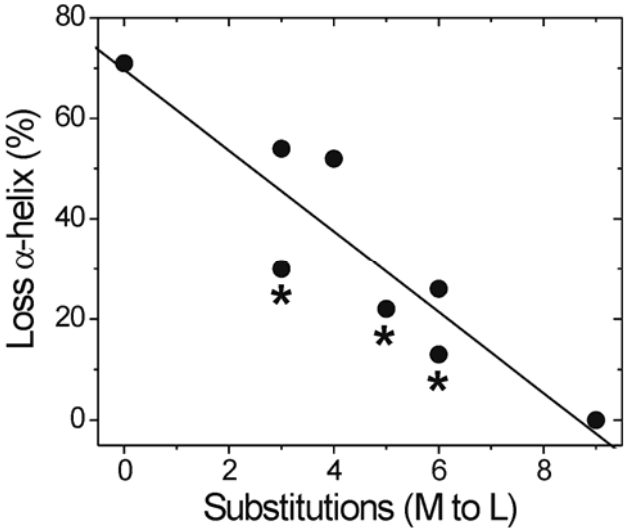

Figure 28: Decreased α-helix content after oxidation correlates with the extent of Met substitutions. Linear regression analysis shows a significant negative relationship between the number of Met to Leu substitutions and the loss in α-helix content after oxidation (p=0.002, R=0.91, slope= -8.04). Secondary structure was evaluated by CD spectroscopy. α-helical content was calculated from the ratio of ellipticity at 208 and 222 nm for non-oxidized and oxidized CaM samples. The percent loss in alpha helical content following oxidation for each CaM mutant is provided in Table 1* Indicates PEST region mutants.

PEST-Region Mutants Resist Degradation by the 20S Proteasome- To determine whether oxidation of specific Met residues alters the proteolytic susceptibility of CaM, the rate of degradation for WT and CaM mutants by the 20S proteasome was compared (Figure 29). With the exception of L9, degradation of the non-oxidized proteins was negligible. For oxidized WT and mutants containing oxidizable Met in the PEST region (L6 NP, L3 CTPP, and L4 CTerm), a significant increase in degradation rate was observed. However, oxidized PEST-region mutants were resistant to degradation, even though the extent of secondary structure loss was similar to the reciprocal non-PEST mutants (Figure 28). In plotting the rates of degradation versus the alpha helical content (Figure 30A), the dramatic differences between the PEST and non-PEST mutants are further highlighted. The loss of secondary structure observed for WT and oxidized Non-PEST mutants demonstrate a significant correlation with their rate of degradation. In contrast, oxidation and the corresponding loss in secondary structure for PEST-region mutants had no effect on the rate of degradation by the proteasome.

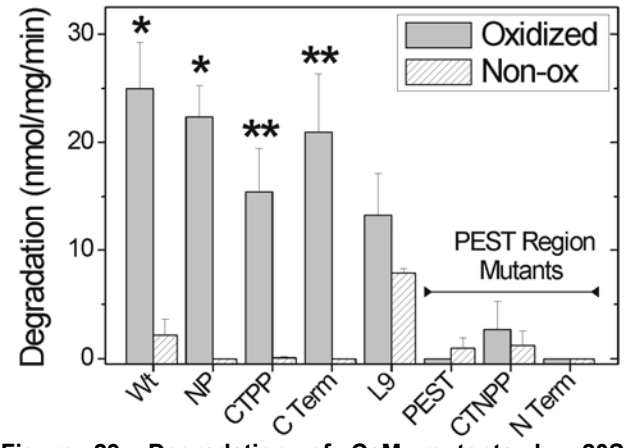

Figure 29: Degradation of CaM mutants by 20S proteasome: PEST region mutants resist proteolysis. CaM degradation by the 20S proteasome was determined from the reaction of free amines generated by peptide bond cleavage with fluorescamine. A minimum of 2-5 separate measurements were performed in triplicate for each sample. * $p<0.01$, **$p<0.06$ comparing oxidized versus non-oxidized samples by t-test analysis.

Hydrophobicity Is Not Altered in PEST-region Mutants- An oxidation-induced exposure of hydrophobic regions within proteins has been suggested as a signal for proteasome degradation (*172-174*). The relative hydrophobicity of WT and mutant CaM

was measured to determine whether mutation of the PEST region preferentially altered the hydrophobicity of the mutant protein and therefore could explain their resistance to degradation. The fluorescence emission of 1-anilinonaphthalene-8-sulfonate (ANS) was used as an indicator of hydrophobicity; an increase in fluorescence is associated with binding of ANS to hydrophobic surfaces that become accessible to the probe (*190*). ANS binding to CaM is blue shifted and increased by binding of calcium to CaM, due to the exposure of hydrophobic pockets (*191-193*). To establish a benchmark for ANS fluorescence changes, WT CaM was incubated with ANS in a buffer containing either EGTA or high (700 μM) calcium. Calcium induced the expected blue shift in emissions maximum along with a 1.9 ± 0.4-fold increase in integrated ANS fluorescence. By comparison, minimal differences in hydrophobicity were observed for oxidized CaM mutants relative to WT CaM; ANS fluorescence intensities ranged from 0.88 to 1.09 (Figure 30B) with no significant change in emissions maximum (data not shown). These results indicate that altered hydrophobicity does not explain the resistance of PEST-region mutants to proteasome degradation.

Thermodynamic Stability: One possible mechanism explaining the difference in susceptibility to proteasome degradation is that oxidation of the N-terminal Met in the non-PEST mutants causes greater destabilization of CaM conformation. This destabilization could promote accelerated unfolding and subsequent rapid degradation by the proteasome. To test the conformational stability of select mutants that are oxidized in either the N- or C-terminus, we monitored the ellipticity at 222 nm using CD spectroscopy. Thermal denaturation and subsequent cooling was performed for temperatures between 10°C and 90°C. For all samples, ellipticity at each temperature with either heating or cooling was essentially identical, suggesting the thermal unfolding was reversible (data not shown). Figure 31 reports the temperature-dependent changes in CD spectra, where the loss of ellipticity reflects CaM denaturation. The non-oxidized samples, including WT and mutants containing three to six Leu substitutions, displayed

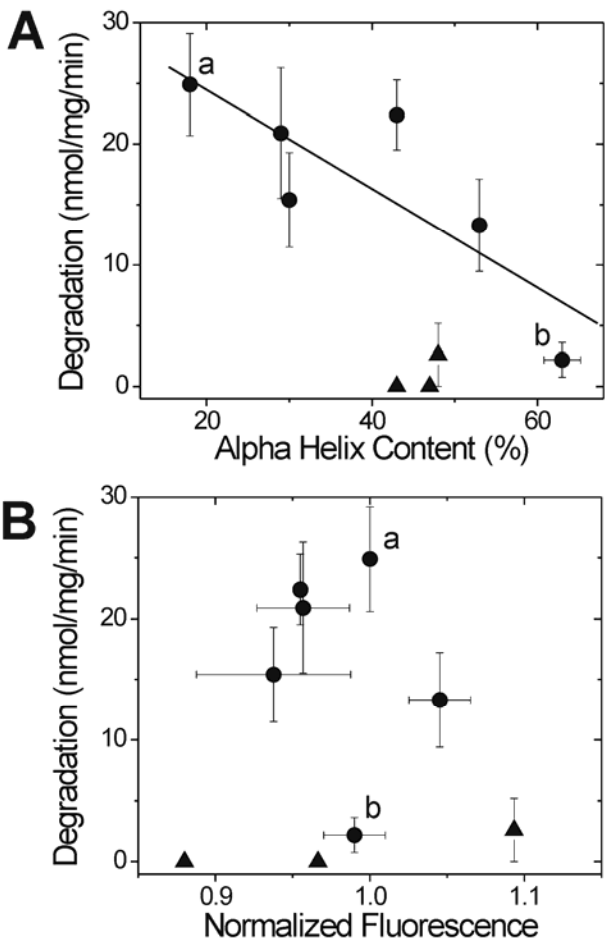

Figure 30: Dependence of CaM degradation on secondary structure and hydrophobicity. (A) The rate of CaM degradation as a function of α-helical content demonstrates a significant linear relationship for WT and all non-PEST region CaM mutants (p=0.04, R=0.83, slope = -0.41) (filled circles). PEST region mutants are plotted as filled triangles. Calculation of α-helical content and CaM degradation are as described in Figure 28 & Figure 29. Oxidized and non-oxidized WT are indicated by a and b, respectively. (B) The rate of CaM degradation showed no significant correlation with hydrophobicity (p=0.65). Hydrophobicity was determined from the fluorescence due to binding of ANS, as described in "Experimental Procedure". Normalized fluorescence is mean ± SD of two separate measures for each sample. Oxidized and non-oxidized WT are indicated by a and b, respectively.

nearly identical patterns of unfolding (Figure 31). These results suggest the Leu substitutions did not alter overall protein conformational stability. Note that two transitions of accelerated denaturation occurred at ~40°C and ~62°C. Previous thermal and chemical denaturation experiments with non-oxidized, calcium-bound CaM determined that the first and second transitions are associated with unfolding of CaM's N- and C-domains, respectively (*194*).

Spectra from oxidized WT CaM showed a significant decrease in signal intensity that corresponds with a mainly unstructured protein (~18% alpha helix at 37°C, (Table 1); no evidence of further unfolding occurred within the temperature range studied. Oxidation of the Non-PEST mutant containing five N-terminal Met (L4 C-Term) also demonstrated a significant loss of signal intensity compared with non-oxidized samples, which is indicative of reduced secondary structure (~29% alpha helix at 37°C, Table 1). There is no evidence of the transition at 40°C, suggesting the N-domain is significantly denatured by oxidation. A minor transition at 60°C is consistent with denaturation of the C-domain. For the L3 PEST mutant, oxidation of five C-terminal Met and Met 36 in the N-terminus resulted in an intermediate loss of signal intensity and reduced secondary structure (~43% alpha helix at 37°C, Table 1). In contrast with L4 C-Term, the L3 PEST mutant exhibited a

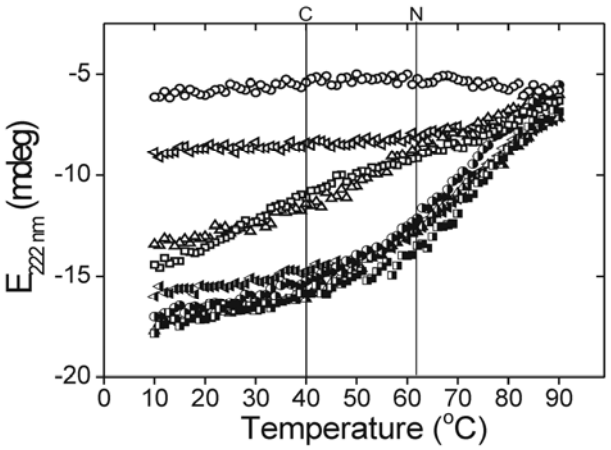

Figure 31: Thermodynamic Stability of WT, PEST- and Non-PEST region mutants. WT (circles), L3PEST (up triangles), L4CTerm (left triangles), and L6NP (squares). Oxidized and non-oxidized samples are represented by open and filled symbols, respectively. Vertical lines indicate C terminal (C) and N terminal (N) domain transitions as reported by Masino et al (*194*). Thermal denaturation experiments were performed as described in "Experimental Procedures.".

single transition that correlates with melting of the N-domain, suggesting the C-domain is significantly denatured by oxidation. These results suggest oxidation of five N-terminal Met (L4 C-Term) destabilizes CaM conformation more than oxidation of five C-terminal Met (L3 PEST) and thus decreased conformational stability may provide a partial explanation for the accelerated degradation of Non-PEST mutants.

To test this idea further, we measured the thermodynamic stability of an additional non-PEST mutant, L6 NP. This mutant contains only three Met that are located in the putative PEST region of the N-terminus. Thus, the L6 NP mutant is the direct correlate to the L3 PEST mutant, where Leu replaces the three Met in the putative PEST region. Importantly, oxidized L6 NP is degraded as rapidly as oxidized L4 C-term, which contains all five met in the N-terminus (Figure 29). Spectra from oxidized L6 NP showed a loss of signal intensity and reduced secondary structure (~43% alpha helix at 37°C, Table 1) that was similar to the thermodynamic changes in ellipticity demonstrated for L3 PEST. Thus, decreased conformational stability is not an absolute requirement for eliciting proteasome degradation. Our results support the hypothesis that CaM degradation is triggered by oxidation-induced disruption of the specific region between Met 51 and Met 72 in the N-terminus. As a caveat, it is possible that limited sensitivity of CD measurements will not permit observing focal disruptions of CaM structure. However, these results help to localize critical points of disruption that trigger proteasome proteolysis.

Table 2: Hill equation parameters for fits to calmodulin concentration dependence of inhibition of sarcoplasmic reticulum vesicle [^{3}H]ryanodine binding.

	Wild Type	L3PEST	L6NP	Oxidized L6NP		Wild Type	L5NTerm	Oxidized L5NTerm		Wild Type	L4CTerm	Oxidized L4CTerm
Inhibition (% Maximal Binding)	12.1±1.0	9.4±1.2	9.2±0.7	7.2±1.4*		15.0±0.8	10.7±0.8*	7.2±1.4*$^{\#}$		17.5±1.7	15.8±1.1	10.3±2.3*
n_i	-1.99±0.53	-2.84±1.33	-3.18±0.93	-2.12±1.41		-2.10±0.38	-3.77±1.34	-2.37±2.09		-1.78±0.53	-1.6±0.34	-2.39±1.8
IC_{50} (nM)	27.8±4.0	35.8±7.5	37.8±4.7	20.5±6.8		31.3±3.0	30.9±3.0	248.3±96.1 *$^{\#}$		37.9±7.4	53.7±7.8	47.5±18.8
n	4	4	4	4		6	6	6		10	10	10

n_i, the Hill coefficient of ryanodine binding; $IC_{50,}$ the concentration of CaM required to achieve half-inhibition of ryanodine binding; n, number of separate experiments performed. *Significantly different ($p<0.05$) from Wild Type. $^{\#}$Significantly different ($p<0.05$) from unoxidized.

Functional Consequences of PEST-region Mutants- To determine the functional consequence of the site-specific mutagenesis and oxidation, we measured CaM regulation of the ryanodine receptor calcium release channel (RyR1) isolated from skeletal muscle. *In vitro*, calcium-activated CaM regulates RyR1 function by inhibiting channel opening, which is measured from the binding of [^{3}H] ryanodine. Ryanodine is a neutral plant alkyloid that binds with high affinity and specificity to open RyR1 channels. Thus, changes in the amount of [^{3}H] ryanodine bound by RyR1 indicate changes in the number of open release channels (*186, 187*)).

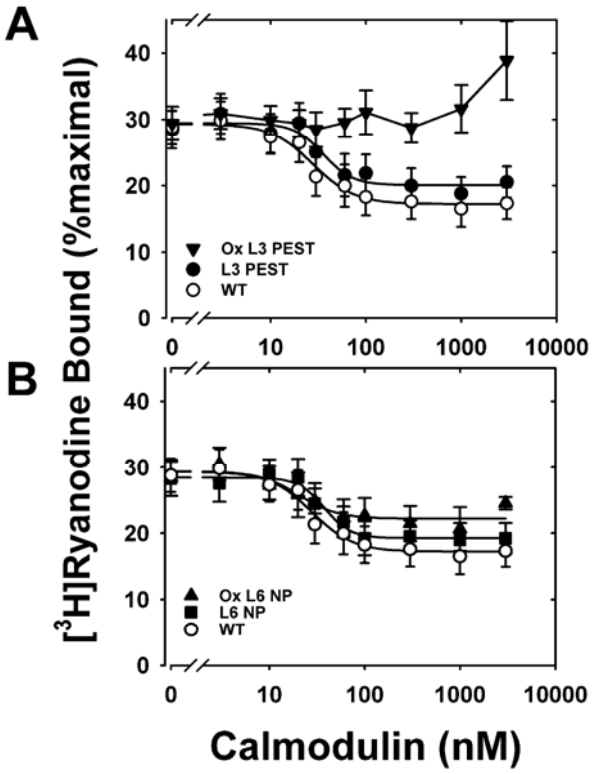

Figure 32: Inhibition of skeletal muscleRyR1 [3H]ryanodine binding for WT and mutant L3PEST and L6NP CaM. (A) non-oxidized WT (○),non-oxidized L3PEST (●), oxidized L3PEST (▼), (B) non-oxidized WT (○), non-oxidized L6 NP (■) and oxidized L6 NP (▲). RyR1 ryanodine binding was performed as described under "Experimental Procedures" in medium containing 700 μM Ca^{2+}. Solid lines represent fits to a four parameter Hill equation. Data are the mean±SEM of 6-10 experiments performed in duplicate. Table 2 reports the kinetic parameters derived from these fits, i.e., extent of inhibition of ryanodine binding, the concentration of CaM required to achieve half-inhibition of ryanodine binding (IC_{50}) or the Hill coefficient (n_i) of ryanodine binding for each fit..

We have previously shown that oxidation of all nine Met residues abolished CaM regulation of RyR1 (*185*). Here we show that while the mutations had no or only minor functional effects on the extent of inhibition of ryanodine binding, the concentration of CaM required to achieve half-inhibition of ryanodine binding (IC_{50}) or the Hill coefficient (n_i) of ryanodine binding (Figure 32, Figure 33, Table 2), oxidation of the PEST-region mutants, L3 PEST and L5 NTerm, causes significant functional impairment for CaM regulation of RyR1. Oxidation of L3 PEST, containing three Met to Leu substitutions within the putative PEST sequence, completely abolished CaM inhibition of ryanodine binding (Figure 32). Oxidation of L5 NTerm, where all N-terminal Met are replaced by Leu and the C-terminal Met are oxidized, also exhibited a loss in function as demonstrated by the decreased extent of inhibition and an eight-fold increase in IC_{50} (Figure 33, Table 2). Compared to the effects of oxidizing PEST region mutants, oxidizing non-PEST region

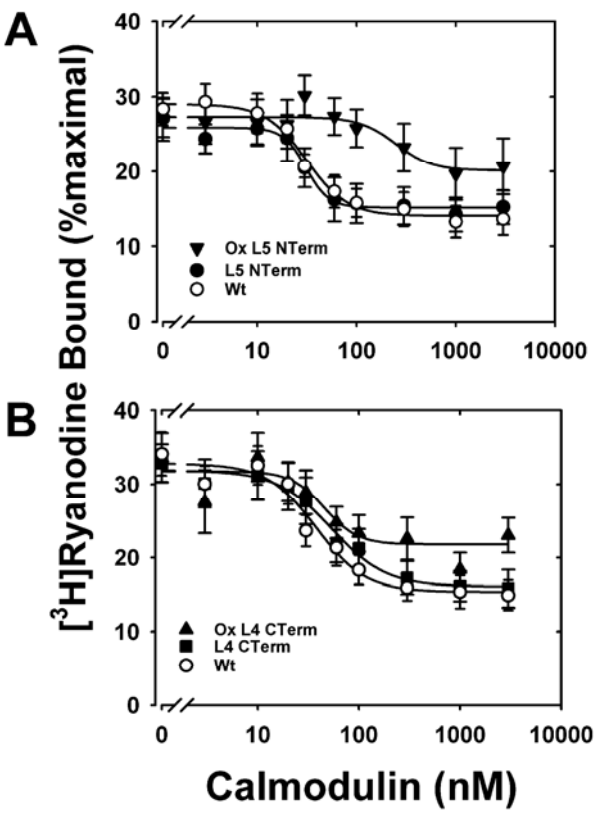

Figure 33: Inhibition of skeletal muscle RyR1 [3H]ryanodine binding for WT and mutant L5 NTerm and L4 CTerm CaM. (A) non-oxidized WT CaM (○), non-oxidized L5 NTerm CaM (●), oxidized L5 NTerm CaM (▼), (B) non-oxidized WT CaM (○),non-oxidized L4 CTerm CaM (■) and oxidized L4 CTerm CaM (▲). RyR1 ryanodine binding was performed as described under "Experimental Procedures" in medium containing 700 μM Ca2+. Solid lines represent fits to a four parameter Hill equation. Data are the mean±SEM of 6-10 experiments performed in duplicate. Table 2 reports the kinetic parameters derived from these fits, i.e., extent of inhibition of ryanodine binding, the concentration of CaM required to achieve half-inhibition of ryanodine binding (IC_{50}) or the Hill coefficient (n_i) of ryanodine binding for each fit.

mutants, L6 NP and L4 CTerm, had relatively minor effects on CaM inhibition of RyR1. Specific oxidation of the Met residues within the PEST sequence (Ox L6 NP) did not alter the extent of inhibition, the Hill coefficient or the IC_{50} when compared to the unoxidized mutant (L6 NP) (Table 2, Figure 32). However, oxidation of L6 NP did cause a decrease in the extent of inhibition compared to WT CaM. Similarly, oxidation of all of the N-terminal Met (L4 CTerm) did not alter any of the Hill equation parameters when compared to the unoxidized mutant, but did cause a significant decrease in the extent of inhibition compare to WT CaM. These results suggest that oxidation of the C-terminal Met residues (i.e., PEST-region mutants) have a greater negative impact on CaM regulation of the RyR1 than oxidation of Met residues in the N-terminus (i.e., non-PEST region mutants). Since oxidation of C-terminal Met does not signal proteasome degradation (Figure 29), accumulation of this CaM oxiform within the cell has the potential to adversely affect CaM regulation of RyR1 and calcium homeostasis.

5.5. Discussion

A

Comparison of Amino Acids Corresponding to Rat CaM Met Residues

Species	Identity	**36**	51	71	**72**	76	109	124	144	145
Human	98%	**M**	M	M	**M**	M	M	M	M	M
Chicken	99%	**M**	M	M	**M**	M	M	M	M	M
Xenopus	100%	**M**	M	M	**M**	M	M	M	M	M
Yeast	60%	**M**	M(52)	L	**M**	L	L	M	L	L
Wheat	91%	**M**	M	L	**M**	M	M	M	V	M
C. elegans	37%	**M**	V	C	**M**	Q	A	V	I	V

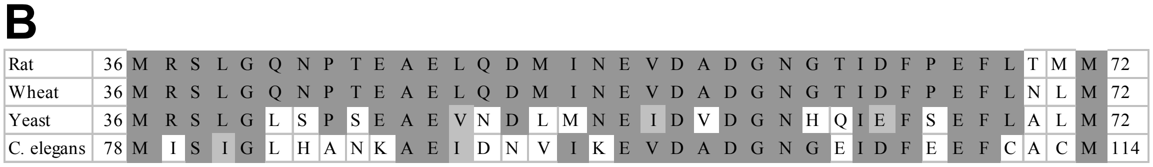

Rat	36	M	R	S	L	G	Q	N	P	T	E	A	E	L	Q	D	M	I	N	E	V	D	A	D	G	N	G	T	I	D	F	P	E	F	L	T	M	M	72
Wheat	36	M	R	S	L	G	Q	N	P	T	E	A	E	L	Q	D	M	I	N	E	V	D	A	D	G	N	G	T	I	D	F	P	E	F	L	N	L	M	72
Yeast	36	M	R	S	L	G	L	S	P	S	E	A	E	V	N	D	L	M	N	E	I	D	V	D	G	N	H	Q	I	E	F	S	E	F	L	A	L	M	72
C. elegans	78	M	I	S	I	G	L	H	A	N	K	A	E	I	D	N	V	I	K	E	V	D	A	D	G	N	G	E	I	D	F	E	E	F	C	A	C	M	114

Figure 34: Alignment of CaM sequences. (A) Comparison of amino acids corresponding with rat CaM Met residues show complete conservation of Met 36 and Met 72 among multiple species. Identity is the percent of amino acids in the entire sequence that are identical with rat CaM. In yeast, there was a Leu in position 51 and a Met in position 52. (B) Figure shows alignment of CaM sequences that correspond with the region containing the putative degron. Identical amino acids and conservative substitutions are highlighted in dark and light grey, respectively.

System of Site-specific Oxidation- The current study utilized site-directed mutagenesis coupled with site-selective oxidation of Met to identify residues that are critical for oxidation-induced degradation by the 20S proteasome. Mutation of Met to Leu is considered a conservative substitution based on data from evolution and the physico-chemical properties of the two amino acids. Throughout evolution, Leu is the most common substitution for Met (*195*). For example, in comparing the CaM sequence from *Sarccharomyces cercvisiae* and mammals, only three of the nine Met are retained in CaM from yeast; the remaining six residues contain Leu substitutions (Figure 34A). Considering the physico-chemical properties, Leu is slightly more hydrophobic than Met, but both amino acids have similar volumes and propensity to form α-helices, which is important considering the abundance of α-helices in CaM (*193, 196*). Data from the

current study is also consistent with the conservative nature of the Met to Leu substitutions; neither secondary structure nor hydrophobicity were substantially altered in CaM mutants containing 3 to 5 substitutions (Table 1).

Model of Protein Degradation by the Proteasome- Recent evidence suggests that signals for substrate recognition by both the 26S and 20S proteasomes are often bipartite, involving binding of an unstructured region coupled with secondary interactions that tether the substrate to the proteasome (*160, 197, 198*). An additional element of the recognition signal is the presence of a sequence within the unstructured region, a degron, that is recognized by the proteasome (*197*). Since the degron is part of the structured region in native protein, it can only become accessible after a post-translational modification, such as phosphorylation or oxidation, causes regional unfolding. Tethering the substrate to the proteasome can be accomplished via ubiquitin, which is recognized by subunits in PA700 (*199*). Other mechanisms for tethering substrates to either the 26S and 20S proteasomes are the ATPase subunits of PA700 and adaptor molecules that bind to the 20S, such as HSP90 or NAD(P)H quinone oxidoreductase 1, that recognize unfolded proteins or specific protein substrates (*170, 200, 201*). Recent studies suggest that even in the absence of adaptor molecules, proteins containing disordered regions can bind to and be degraded by the 20S proteasome (*202*). Taken together, these studies suggest the critical element for initiating degradation is the engagement of an unstructured region of the substrate with either the 20S or 26S proteasome.

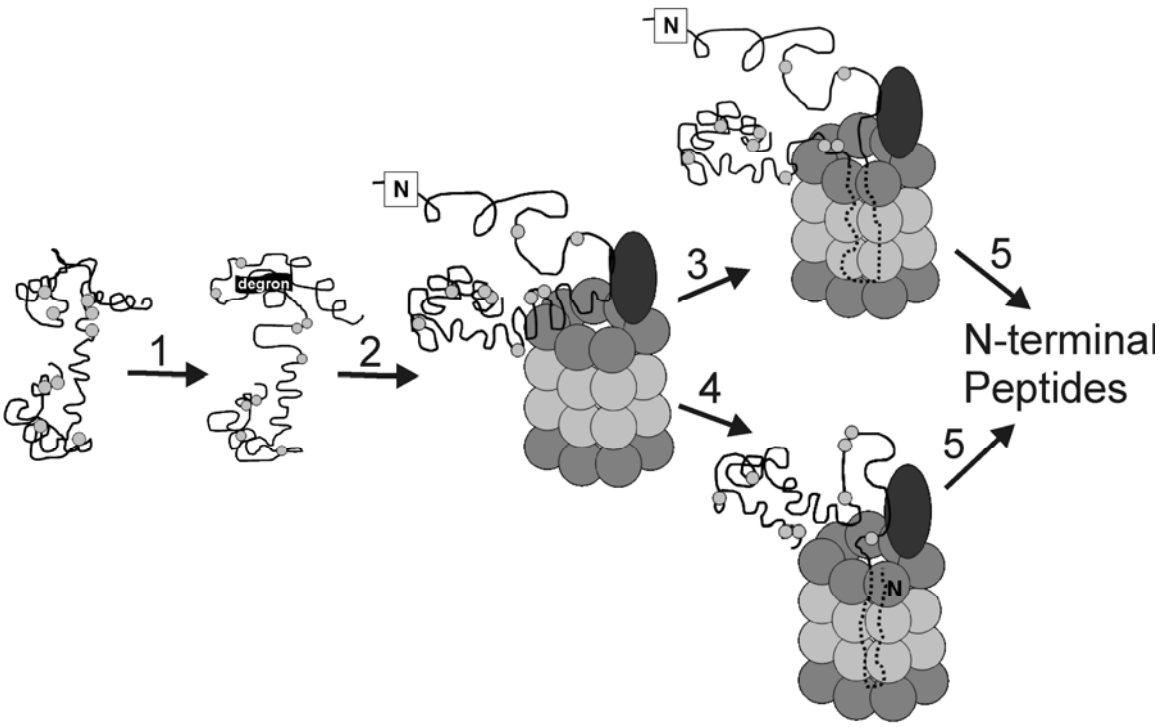

Figure 35: Model for CaM degradation by the 20S proteasome. CaM ribbon structure is shown with Met residues indicated as grey balls. The 20S proteasome is represented as a cylinder of four seven-member rings of subunits. CaM degradation is initiated by events, such as oxidation of N-terminal Met, that cause regional unfolding in the N-terminus (1). The degron, consisting of the disordered N-terminus plus a cryptic degradation sequence, is recognized and binds to the 20S and/or HSP90 (dark oval) (2). Degradation of the N-terminus occurs following translocation of either an unstructured loop (endoproteolysis) (3) or the free N-terminus (4) into the catalytic chamber. N-terminal peptides are initially released (5).

Model of CaM Degradation by the 20S Proteasome- Results from the current study shows that preventing oxidation of 3 to 5 Met in the N-terminus via Leu substitutions produces mutants that are resistant to degradation (Figure 29, PEST Region Mutants). Conversely, the unique oxidation of 3 to 5 N-terminal Met elicits rapid proteolysis by the 20S proteasome (Figure 29). These data suggest that the N-terminus contains a degradation signal that is revealed by site-specific oxidation of N-terminal Met. As a caveat, our in vitro results were obtained in the absence of the cadre of cellular proteins that could influence CaM proteolysis. Thus, these results may reflect an oversimplified view of CaM degradation by the proteasome. On the other hand, these in vitro experiments bring new biochemical and structural clarity to specific regions within

CaM that contain a potential degron, thus providing important guidance for future experiments in cultured cells where the in vivo conditions are more closely aligned.

As a general model for CaM degradation, we propose that an essential step in eliciting digestion by the proteasome is regional unfolding of the N-terminus caused by events such as oxidation of N-terminal Met (Figure 35). The unstructured region, along with a cryptic sequence that becomes solvent exposed, serves as the recognition element for binding to the 20S proteasome and/or adaptor proteins, such as HSP 90. Degradation of the N-terminus occurs following translocation of either an unstructured loop (endoproteolysis) or the free N-terminus into the catalytic chamber. As shown previously, the initial products of degradation are peptides derived from the N-terminus (*175, 178, 179*).

In our preparations of proteasome from liver, HSP 90 is tightly associated and co-purifies with the 20S catalytic core (*177, 200*). Previous reports have demonstrated an essential role for HSP90 in the degradation of oxidized CaM by the 20S proteasome (*200*). While all of the 20S preparations used in this study contained essentially the same amount of HSP90, we did not specifically test for mutant-specific differences in HSP90 interaction, which could affect rates of degradation. Another factor that could influence the rate of degradation is conformational stability since less stable proteins may be more easily unfolded and rapidly degraded. We tested stability under conditions of heat denaturation (Figure 31) and found similar conformational stability for oxidized mutants containing either Leu substitutions for Met 51, 71, and 72 (L3 PEST) or Leu substitutions at all positions except Met 51, 71, 72 (L6 NP). Oxidized L6 NP is rapidly degraded but oxidized L3PEST resists proteasome degradation. Taken together, these results suggest

that altered conformational stability does not explain the difference in susceptibility to proteasome degradation. These results also support the hypothesis that oxidation-induced perturbation of the region localized to residues 51 to 72 triggers proteasome proteolysis.

Sequence alignment of CaM from multiple species shows complete conservation of Met 36 and 72 (Figure 34A) even between divergent species, i.e., rat, wheat, and *C. elegans*. With the exception of *C. elegans*, Met 51 is also highly conserved among different species. The evolutionary conservation suggests that these residues are involved in critical functions. In addition to the well-described function of Met in providing surface contact with target proteins (*176*), data from the current study suggests that oxidation of one or more of these residues may also be an essential component for triggering proteasome degradation.

Besides oxidation of N-terminal Met, mutations or oxidation of other sites in the protein that cause conformational rearrangement could also elicit proteasome proteolysis. In the current study, mutation of all nine Met to Leu (L9) resulted in a loss of secondary structure (Table 1) that correlated with increased proteasome degradation (Figure 29, Figure 30). These results are consistent with a previous report of increased susceptibility of the L9 CaM mutant to proteasome degradation (*178*). Notably, mutation or oxidation of a single Met in the C-terminus can also elicit rapid proteasome proteolysis. Squier and colleagues showed that either mutation or oxidation of Met_{145} caused global tertiary structural rearrangements that correlated with rapid proteolysis by the proteasome (*178, 203*). Thus, it is possible that the conformational changes associated with altering Met_{145} causes regional unfolding and exposure of the recognition elements in the N-terminus that initiate proteasome proteolysis.

The unstructured region is often part of a bipartite recognition element that forms in conjunction with other residues that occur nearby in the primary sequence. Some degrons have sequences that are unique to specific proteins. For example, the degron specific for ornithine decarboxylase contains a structural motif that consists of the Cys $_{441}$-Ala $_{442}$ recognition element plus an unstructured C-terminus (*167*). The degron for cFos includes the tri-peptide motif Pro-Thr-Leu plus an additional undescribed structural element (*168, 204*). Notably, the "Pro-Thr-Leu" signal is unique to cFos since other protein family members contain a similar sequence that does not elicit degradation.

The PEST motif, which is rich in Pro, Glu, Asp, Ser, and Thr, is a well-known degron that is found in many proteins. While historically PEST was first described in proteins with short half-lives, our expanded understanding of protein degradation suggests that PEST is not limited to these proteins. For example, myosin heavy chain from rat heart has a half-life of 5.9 days (*205*) and contains a potential PEST sequence (PEST score +19.32) encompassing residues 369 to 382. Reported half-life of CaM in rat muscle and brain are 10 and 18 hours, respectively (*206, 207*). This half-life is short compared with the half-lives of the sarcoplasmic reticulum Ca-ATPase (14 days) and plasma membrane Ca-ATPase (12 days) reported from rat muscle and brain (*207, 208*). Thus, CaM may qualify as a "short-lived protein" when compared with other calcium regulatory proteins in the same tissue.

Although analysis of the CaM sequence using the PEST algorithm indicated CaM residues 36 to 72 as a weak PEST signal (Figure 27), substitution of Gln for Met to mimic oxidation improved the likelihood of a PEST motif. Sequence alignment of CaM from divergent species shows considerable identity (Figure 34B), providing further

support that this region contains a sequence that is part of the recognition element for proteasome degradation. It is also possible that a CaM-specific sequence in the N-terminus, such as the highly conserved residues $_{58}$DGNxxIDFxEF$_{68,}$ could serve as the degron.

One model of proteolytic digestion of substrates involves the translocation of the unstructured N- or C-termini into the catalytic chamber where the protein is fully degraded into peptides (*204, 209*). A second model involves endoproteolysis, where a disordered polypeptide loop is translocated into the catalytic chamber, resulting in partial digestion of the substrate (*203, 210*). This is the putative mechanism utilized for activation of transcription factors, such as the processing of the active nuclear factor κ B transcription factor p50 from the inactive precursor p105 (*210*). Another factor that influences the extent and rate of degradation includes the secondary structure of the region directly adjacent to the degradation signal. For example, proteins are readily digested when the degradation signal is next to a region containing either α-helices or irregular loops (*211*). Conversely, regions containing highly stable secondary structure, such as β-sheet, resist degradation (*211*).

With CaM, the N-terminal globular domain is followed by a flexible linker region (residues 75 to 86) consisting of an eight turn α-helix that tethers the two opposing domains (*176*). Biophysical measures of the solution structure of CaM report that the central linker exhibits considerable flexible and can adopt a non-helical conformation upon binding many of its target proteins (*176*). Thus, the presence of a favorable secondary structure adjacent to the putative degron that is exposed upon oxidation of the N-terminal Met may promote rapid CaM digestion. Additionally, the flexible central

linker region could permit endoproteolysis of CaM when conditions cause disorder in this region. Indeed, peptides generated from proteolysis of oxidized WT CaM by the 20S proteasome are consistent with both endoproteolysis as well as N-terminal degradation. Supporting endoproteolysis of oxidized CaM are the release of large N-terminal domain fragments (A_1-F_{92} and A_1-K_{30}) (*178, 179*) and multiple peptides originating from the flexible linker region (*179*). Consistent with proteolytic digestion of the free N-terminus, data from our previous work (*175*) showed numerous peptides originating mainly from the N-terminal domain were produced after one hour digestion of oxidized WT CaM. These differences in peptides released by the 20S proteasome could depend on the region and extent of CaM structural unfolding or could be due to differences in the adaptor molecules that co-purify with the 20S proteasome. None-the-less, these data support the hypothesis that the site of recognition and initial degradation is in CaM's N-terminus.

Physiological Relevance of CaM Oxidation and Proteasome Proteolysis- The binding of up to four calcium ions to CaM elicits significant conformational changes that increase the exposure of hydrophobic residues, e.g., Met, that serve as binding sites for target proteins (*176*). This conformational flexibility allows CaM to regulate over 100 different proteins in a wide variety of configurations (*176*). Additionally, the extent of calcium (Ca^{2+}) saturation and location of bound Ca^{2+} ions also influences CaM's binding to targets. For example, the Ca^{2+}-loaded N-lobe of CaM binds to a peptide of the Ca^{2+}-activated small conductance potassium channel while the Ca^{2+}-free C-lobe binds to a noncontiguous region of the target (*212*). Conversely, CaM binds anthrax adenylyl cylcase endotoxin via a Ca^{2+} loaded C-lobe and a Ca^{2+}-free N-lobe (*213*). Thus, CaM binding to specific targets can alter the solvent exposure of select Met residues. Because

solvent accessibility is a major determinant of susceptibility to oxidation, the specific Met residues subjected to oxidative modification may vary depending on the cellular conditions that determine intracellular calcium levels and subsequently, CaM binding partners.

Data from the current study (Figure 31, Figure 32) and others (*214-216*) have shown that oxidation of specific Met can significantly alter CaM's ability to regulate protein targets. Therefore, efficient removal of oxidized CaM is critical for maintain cell signaling. In the case of RyR1, oxidation of CaM's C-terminal Met were more deleterious to regulation of the channel than oxidation of CaM's N-terminal Met (Figure 31, Figure 32). Unless C-terminal oxidized CaM is removed from the cell, cell signaling would be significantly impaired.

In the current study, data support the presence of a degron in the N-terminus that is reveal by oxidation of N-terminal Met (Figure 29). The presence of an additional degron in CaM's C-terminus has also been proposed (*178*). Squier and colleagues (*178*) reported that oxidation of Met $_{145}$ induced an alteration in CaM's tertiary structure that triggered degradation. In the present study, oxidation of multiple C-terminal Met (L6 CTNPP), including Met 145, did not increase the rate of CaM degradation (Figure 29). It is possible that under our experimental conditions, i.e., oxidation of multiple C-terminal Met and a lower free calcium concentration (~10 μM versus 100 μM), the C-terminal degron is not exposed. Therefore, we cannot rule out the possibility that CaM contains degrons in both the N- and C-terminus. Multiple degrons would be advantageous considering the potential for site-selective oxidation that occurs when CaM is complexed with specific proteins.

The extent of CaM methionine oxidation *in vivo* has been estimated at ~two Met sulfoxide per CaM in both young and aged rat muscle (*217*) and in the brain of aged rats (*218*). In brain, the *in vivo* sites of modification were defined by HPLC separation of trypsin-generated peptides followed by mass spectrometry (*218*). In both young and aged brains, Met sulfoxide at position 76 was detected, suggesting that this site is readily oxidized *in vivo* and is likely not a signal for degradation. In aged brain, there was a general increase in oxidation of Met based on the appearance of multiple tryptic peptides containing Met sulfoxide. However, abundantly present in aged brain were two tryptic peptides containing a single added oxygen that corresponded with oxidation of Met 36 and oxidation of either Met 51, 71, or 72. The presence of oxidized Met in the putative CaM degron coupled with decreased proteasome activity reported in aged rat brain (*219*) suggests aging is accompanied by defects in proteasome-dependent removal of damaged CaM, which could lead to an *in vivo* loss in CaM signaling. In support of this idea, the age-dependent increase in Met sulfoxide content correlated with a reduction in the ability of CaM isolated from aged brain to activate the plasma membrane Ca-ATPase, an *in vivo* CaM target (*218*). Hence, even limited Met oxidation can alter the ability of CaM to regulate target proteins, further supporting an essential role for proteasome in maintaining cell signaling via the efficient removal of oxidatively damaged proteins.

Conclusion. We have used site-directed Met oxidation, followed by measurement of proteasome susceptibility and circular dichroism, to define both the chemical and structural features of the degron, the portion of CaM that is involved in targeting proteasome degradation. These results are important not only in providing the molecular

details of CaM as a proteasome substrate, but also in furthering our fundamental understanding of proteasome action on oxidized protein substrates.

CHAPTER 6 - Discussion and Future Directions

6.1. Summary of Current Study

The work presented here provides new insights into the regulation of calcium in the heart, which depends on the coordinate regulation of SERCA by PLB. Having a better understanding of how PLB regulates SERCA is crucial for designing and testing new treatments for heart failure. Toward this end, one major contribution we made was establishing a quick and convenient FRET method to screen potential PLB mutants for usage in gene therapy to treat heart failure.

Many fluorescence techniques were utilized during this work to determine the mechanism of Ca^{2+} transport in the heart. We established a FRET procedure for screening potential PLB mutants for use in gene therapy trials to treat heart failure. Time-resolved FRET experiments permitted us to verify another nucleotide binding site in SERCA, bringing the γ-phosphate of ADP closer to the Asp 351 that gets phosphorylated. Transient time-resolved FRET was a powerful technique for connecting structural dynamics of SERCA with its static crystal structures by identifying a biphasic reaction for TNP-ADP binding to SERCA. Steady state fluorescence experiments disproved that hydrophobicity is a signal for proteasomal degradation. Fluorescence spectroscopy is a potent technique for probing the SERCA-PLB interaction and is quite versatile in its applications.

6.2. FRET Screening Method for Testing Potential PLB Mutants for Use in Gene Therapy

The interaction between SERCA and PLB has become a therapeutic target since heart failure has been associated with an increase in ratio of PLB to SERCA (*7*). Studies have been performed on small and large animals to investigate an in vivo cardiac rAAV delivery of S16E, a pseudophosphorylated PLB mutant. The reports found that this method improved cardiac function (*129-133*). The results presented here provide a rational explanation for the partial success of S16E-based gene therapy. Specifically, we have illustrated that two LOF PLB mutants were able to compete with WT-PLB both functionally and physically, and that the inhibitory potency of these PLB mutants is distinct from the binding affinity. With these results, we will be able to design and test PLB mutants using this convenient FRET method. Work has already begun to design double mutants so that one mutation affects the affinity and the other affects the functional effect on SERCA. In addition, this technology has been transferred to an HEK system utilizing FRET to see if competition occurs in living cells. Results so far are promising and will add extra support to using FRET to screen PLB mutants for use in gene therapy to treat heart failure.

6.3. TR-FRET Confirms the Existence of a New Nucleotide Binding Site in SERCA

A newer FRET technique, transient time-resolved FRET, allowed us to resolve whether a novel nucleotide binding site existed in SERCA based on the crystal structure containing CPA (PDB code 2OA0) (*154*). Using AEDANS-SERCA and TNP-ADP, a fluorescent nucleotide, we found that our FRET data was consistent with the crystal structure, implying that there is another nucleotide binding site within SERCA. This site

brings the γ-phosphate closer to the Asp351, which gets phosphorylated during SERCA catalytic cycle. This step is crucial for transporting Ca^{2+} across the membrane through SERCA. Additionally, transient time-resolved FRET experiments depicted a biphasic reaction revealing a fast component, representing nucleotide binding (ES from Figure 26), and a slow component, representing a structural change within SERCA (E*S from Figure 26). Future studies will include the effect of Ca^{2+} and the effect of PLB on nucleotide binding within SERCA. This method will also be applicable to other systems involving kinetics of nucleotide binding.

6.4. Signals for Proteasomal Degradation Using CaM as a Model System

Using calmodulin as a model system, we also investigated the signals for proteasomal degradation. Our approach utilized site-directed mutagenesis in order to perform site-selective oxidation of methionine residues. We found that oxidation of Met residues 51, 71, and 72 located in the N-terminus of CaM are critical for degradation. We also tested the hypothesis that hydrophobicity is a signal for degradation using fluorescence spectroscopy. However, our results did not confirm this hypothesis. Though, the focus was on determining the signals for degradation, this work did relate to Ca^{2+} regulation. Functional data from ryanodine binding assays demonstrated that oxidation of Met residues in the C-terminus completely abolished CaM inhibition of RyR. Accumulation of these oxidized CaM in the cell could be detrimental to CaM regulation of RyR, altering Ca^{2+} regulation during muscle contraction. Future studies using will continue to elucidate oxidation of CaM affects its binding to RyR.

REFERENCES

1. **Bers, D. M. (2002) Cardiac excitation-contraction coupling, *Nature 415*, 198-205.**
2. **MacLennan, D. H., and Toyofuku, T. (1996) Regulatory interactions between calcium ATPases and phospholamban, *Soc Gen Physiol Ser 51*, 89-103.**
3. **Toyoshima, C., and Inesi, G. (2004) Structural basis of ion pumping by Ca2+-ATPase of the sarcoplasmic reticulum, *Annu Rev Biochem 73*, 269-292.**
4. **Inesi, G., Lewis, D., Ma, H., Prasad, A., and Toyoshima, C. (2006) Concerted conformational effects of Ca2+ and ATP are required for activation of sequential reactions in the Ca2+ ATPase (SERCA) catalytic cycle, *Biochemistry 45*, 13769-13778.**
5. **Simmerman, H. K., and Jones, L. R. (1998) Phospholamban: protein structure, mechanism of action, and role in cardiac function, *Physiol Rev 78*, 921-947.**
6. **Cornea, R. L., Jones, L. R., Autry, J. M., and Thomas, D. D. (1997) Mutation and phosphorylation change the oligomeric structure of phospholamban in lipid bilayers, *Biochemistry 36*, 2960-2967.**
7. **MacLennan, D. H., and Kranias, E. G. (2003) Phospholamban: a crucial regulator of cardiac contractility, *Nat Rev Mol Cell Biol 4*, 566-577.**
8. **Reddy, L. G., Jones, L. R., and Thomas, D. D. (1999) Depolymerization of phospholamban in the presence of calcium pump: a fluorescence energy transfer study, *Biochemistry 38*, 3954-3962.**
9. **Tada, M., Kadoma, M., Fujii, J., Kimura, Y., and Kijima, Y. (1989) Molecular structure and function of phospholamban: the regulatory protein of calcium pump in cardiac sarcoplasmic reticulum, *Adv Exp Med Biol 255*, 79-89.**
10. **Wegener, A. D., Simmerman, H. K., Lindemann, J. P., and Jones, L. R. (1989) Phospholamban phosphorylation in intact ventricles. Phosphorylation of serine 16 and threonine 17 in response to beta-adrenergic stimulation, *J Biol Chem 264*, 11468-11474.**
11. **Simmerman, H. K., Collins, J. H., Theibert, J. L., Wegener, A. D., and Jones, L. R. (1986) Sequence analysis of phospholamban. Identification of phosphorylation sites and two major structural domains, *J Biol Chem 261*, 13333-13341.**
12. **Hamilton, S. L., and Serysheva, II. (2009) Ryanodine receptor structure: progress and challenges, *J Biol Chem 284*, 4047-4051.**
13. **Inui, M., Saito, A., and Fleischer, S. (1987) Purification of the ryanodine receptor and identity with feet structures of junctional terminal cisternae of sarcoplasmic reticulum from fast skeletal muscle, *J Biol Chem 262*, 1740-1747.**

14. Lai, F. A., Erickson, H. P., Rousseau, E., Liu, Q. Y., and Meissner, G. (1988) Purification and reconstitution of the calcium release channel from skeletal muscle, *Nature 331*, 315-319.

15. Hakamata, Y., Nakai, J., Takeshima, H., and Imoto, K. (1992) Primary structure and distribution of a novel ryanodine receptor/calcium release channel from rabbit brain, *FEBS Lett 312*, 229-235.

16. Ludtke, S. J., Serysheva, II, Hamilton, S. L., and Chiu, W. (2005) The pore structure of the closed RyR1 channel, *Structure 13*, 1203-1211.

17. Orlova, E. V., Serysheva, II, van Heel, M., Hamilton, S. L., and Chiu, W. (1996) Two structural configurations of the skeletal muscle calcium release channel, *Nat Struct Biol 3*, 547-552.

18. Radermacher, M., Wagenknecht, T., Grassucci, R., Frank, J., Inui, M., Chadwick, C., and Fleischer, S. (1992) Cryo-EM of the native structure of the calcium release channel/ryanodine receptor from sarcoplasmic reticulum, *Biophys J 61*, 936-940.

19. Radermacher, M., Rao, V., Grassucci, R., Frank, J., Timerman, A. P., Fleischer, S., and Wagenknecht, T. (1994) Cryo-electron microscopy and three-dimensional reconstruction of the calcium release channel/ryanodine receptor from skeletal muscle, *J Cell Biol 127*, 411-423.

20. Samso, M., Wagenknecht, T., and Allen, P. D. (2005) Internal structure and visualization of transmembrane domains of the RyR1 calcium release channel by cryo-EM, *Nat Struct Mol Biol 12*, 539-544.

21. Samso, M., Feng, W., Pessah, I. N., and Allen, P. D. (2009) Coordinated movement of cytoplasmic and transmembrane domains of RyR1 upon gating, *PLoS Biol 7*, e85.

22. Serysheva, II, Orlova, E. V., Chiu, W., Sherman, M. B., Hamilton, S. L., and van Heel, M. (1995) Electron cryomicroscopy and angular reconstitution used to visualize the skeletal muscle calcium release channel, *Nat Struct Biol 2*, 18-24.

23. Serysheva, II, Schatz, M., van Heel, M., Chiu, W., and Hamilton, S. L. (1999) Structure of the skeletal muscle calcium release channel activated with Ca2+ and AMP-PCP, *Biophys J 77*, 1936-1944.

24. Serysheva, II, Hamilton, S. L., Chiu, W., and Ludtke, S. J. (2005) Structure of Ca2+ release channel at 14 A resolution, *J Mol Biol 345*, 427-431.

25. Serysheva, II, Ludtke, S. J., Baker, M. L., Cong, Y., Topf, M., Eramian, D., Sali, A., Hamilton, S. L., and Chiu, W. (2008) Subnanometer-resolution electron cryomicroscopy-based domain models for the cytoplasmic region of skeletal muscle RyR channel, *Proc Natl Acad Sci U S A 105*, 9610-9615.

26. Sharma, M. R., Penczek, P., Grassucci, R., Xin, H. B., Fleischer, S., and Wagenknecht, T. (1998) Cryoelectron microscopy and image analysis of the cardiac ryanodine receptor, *J Biol Chem 273*, 18429-18434.

27. Sharma, M. R., Jeyakumar, L. H., Fleischer, S., and Wagenknecht, T. (2000) Three-dimensional structure of ryanodine receptor isoform three in two conformational states as visualized by cryo-electron microscopy, *J Biol Chem 275*, 9485-9491.

28. Benacquista, B. L., Sharma, M. R., Samso, M., Zorzato, F., Treves, S., and Wagenknecht, T. (2000) Amino acid residues 4425-4621 localized on the three-dimensional structure of the skeletal muscle ryanodine receptor, *Biophys J 78*, 1349-1358.

29. Du, G. G., Sandhu, B., Khanna, V. K., Guo, X. H., and MacLennan, D. H. (2002) Topology of the Ca2+ release channel of skeletal muscle sarcoplasmic reticulum (RyR1), *Proc Natl Acad Sci U S A 99*, 16725-16730.

30. Lanner, J. T., Georgiou, D. K., Joshi, A. D., and Hamilton, S. L. Ryanodine receptors: structure, expression, molecular details, and function in calcium release, *Cold Spring Harb Perspect Biol 2*, a003996.

31. Wagenknecht, T., Berkowitz, J., Grassucci, R., Timerman, A. P., and Fleischer, S. (1994) Localization of calmodulin binding sites on the ryanodine receptor from skeletal muscle by electron microscopy, *Biophys J 67*, 2286-2295.

32. Wagenknecht, T., Grassucci, R., Berkowitz, J., Wiederrecht, G. J., Xin, H. B., and Fleischer, S. (1996) Cryoelectron microscopy resolves FK506-binding protein sites on the skeletal muscle ryanodine receptor, *Biophys J 70*, 1709-1715.

33. Wagenknecht, T., Radermacher, M., Grassucci, R., Berkowitz, J., Xin, H. B., and Fleischer, S. (1997) Locations of calmodulin and FK506-binding protein on the three-dimensional architecture of the skeletal muscle ryanodine receptor, *J Biol Chem 272*, 32463-32471.

34. Samso, M., and Wagenknecht, T. (2002) Apocalmodulin and Ca2+-calmodulin bind to neighboring locations on the ryanodine receptor, *J Biol Chem 277*, 1349-1353.

35. Sharma, M. R., Jeyakumar, L. H., Fleischer, S., and Wagenknecht, T. (2006) Three-dimensional visualization of FKBP12.6 binding to an open conformation of cardiac ryanodine receptor, *Biophys J 90*, 164-172.

36. Meng, X., Wang, G., Viero, C., Wang, Q., Mi, W., Su, X. D., Wagenknecht, T., Williams, A. J., Liu, Z., and Yin, C. C. (2009) CLIC2-RyR1 interaction and structural characterization by cryo-electron microscopy, *J Mol Biol 387*, 320-334.

37. Moore, C. P., Rodney, G., Zhang, J. Z., Santacruz-Toloza, L., Strasburg, G., and Hamilton, S. L. (1999) Apocalmodulin and Ca2+ calmodulin bind to the same region on the skeletal muscle Ca2+ release channel, *Biochemistry 38*, 8532-8537.

38. Yamaguchi, N., Xu, L., Pasek, D. A., Evans, K. E., Chen, S. R., and Meissner, G. (2005) Calmodulin regulation and identification of calmodulin binding region of type-3 ryanodine receptor calcium release channel, *Biochemistry 44*, 15074-15081.

39. Tripathy, A., Xu, L., Mann, G., and Meissner, G. (1995) Calmodulin activation and inhibition of skeletal muscle Ca2+ release channel (ryanodine receptor), *Biophys J 69*, 106-119.

40. Rodney, G. G., Williams, B. Y., Strasburg, G. M., Beckingham, K., and Hamilton, S. L. (2000) Regulation of RYR1 activity by Ca(2+) and calmodulin, *Biochemistry 39*, 7807-7812.

41. **Yamaguchi, N., Xu, L., Pasek, D. A., Evans, K. E., and Meissner, G. (2003) Molecular basis of calmodulin binding to cardiac muscle Ca(2+) release channel (ryanodine receptor), *J Biol Chem 278*, 23480-23486.**

42. **Chelu, M. G., Danila, C. I., Gilman, C. P., and Hamilton, S. L. (2004) Regulation of ryanodine receptors by FK506 binding proteins, *Trends Cardiovasc Med 14*, 227-234.**

43. **Jayaraman, T., Brillantes, A. M., Timerman, A. P., Fleischer, S., Erdjument-Bromage, H., Tempst, P., and Marks, A. R. (1992) FK506 binding protein associated with the calcium release channel (ryanodine receptor), *J Biol Chem 267*, 9474-9477.**

44. **Timerman, A. P., Ogunbumni, E., Freund, E., Wiederrecht, G., Marks, A. R., and Fleischer, S. (1993) The calcium release channel of sarcoplasmic reticulum is modulated by FK-506-binding protein. Dissociation and reconstitution of FKBP-12 to the calcium release channel of skeletal muscle sarcoplasmic reticulum, *J Biol Chem 268*, 22992-22999.**

45. **Qi, Y., Ogunbunmi, E. M., Freund, E. A., Timerman, A. P., and Fleischer, S. (1998) FK-binding protein is associated with the ryanodine receptor of skeletal muscle in vertebrate animals, *J Biol Chem 273*, 34813-34819.**

46. **Brillantes, A. B., Ondrias, K., Scott, A., Kobrinsky, E., Ondriasova, E., Moschella, M. C., Jayaraman, T., Landers, M., Ehrlich, B. E., and Marks, A. R. (1994) Stabilization of calcium release channel (ryanodine receptor) function by FK506-binding protein, *Cell 77*, 513-523.**

47. **Masumiya, H., Wang, R., Zhang, J., Xiao, B., and Chen, S. R. (2003) Localization of the 12.6-kDa FK506-binding protein (FKBP12.6) binding site to the NH2-terminal domain of the cardiac Ca2+ release channel (ryanodine receptor), *J Biol Chem 278*, 3786-3792.**

48. **Jeyakumar, L. H., Ballester, L., Cheng, D. S., McIntyre, J. O., Chang, P., Olivey, H. E., Rollins-Smith, L., Barnett, J. V., Murray, K., Xin, H. B., and Fleischer, S. (2001) FKBP binding characteristics of cardiac microsomes from diverse vertebrates, *Biochem Biophys Res Commun 281*, 979-986.**

49. **Timerman, A. P., Wiederrecht, G., Marcy, A., and Fleischer, S. (1995) Characterization of an exchange reaction between soluble FKBP-12 and the FKBP.ryanodine receptor complex. Modulation by FKBP mutants deficient in peptidyl-prolyl isomerase activity, *J Biol Chem 270*, 2451-2459.**

50. **Timerman, A. P., Onoue, H., Xin, H. B., Barg, S., Copello, J., Wiederrecht, G., and Fleischer, S. (1996) Selective binding of FKBP12.6 by the cardiac ryanodine receptor, *J Biol Chem 271*, 20385-20391.**

51. **McCall, E., Li, L., Satoh, H., Shannon, T. R., Blatter, L. A., and Bers, D. M. (1996) Effects of FK-506 on contraction and Ca2+ transients in rat cardiac myocytes, *Circ Res 79*, 1110-1121.**

52. **Marx, S. O., Gaburjakova, J., Gaburjakova, M., Henrikson, C., Ondrias, K., and Marks, A. R. (2001) Coupled gating between cardiac calcium release channels (ryanodine receptors), *Circ Res 88*, 1151-1158.**

53. **Marx, S. O., Ondrias, K., and Marks, A. R. (1998) Coupled gating between individual skeletal muscle Ca2+ release channels (ryanodine receptors), *Science 281*, 818-821.**

54. Ahern, G. P., Junankar, P. R., and Dulhunty, A. F. (1997) Subconductance states in single-channel activity of skeletal muscle ryanodine receptors after removal of FKBP12, *Biophys J 72*, 146-162.

55. Ahern, G. P., Junankar, P. R., and Dulhunty, A. F. (1994) Single channel activity of the ryanodine receptor calcium release channel is modulated by FK-506, *FEBS Lett 352*, 369-374.

56. Moller, J. V., Nissen, P., Sorensen, T. L., and le Maire, M. (2005) Transport mechanism of the sarcoplasmic reticulum Ca2+ -ATPase pump, *Curr Opin Struct Biol 15*, 387-393.

57. MacLennan, D. H., and Green, N. M. (2000) Structural biology. Pumping ions, *Nature 405*, 633-634.

58. MacLennan, D. H., Rice, W. J., and Green, N. M. (1997) The mechanism of Ca2+ transport by sarco(endo)plasmic reticulum Ca2+-ATPases, *J Biol Chem 272*, 28815-28818.

59. Mahaney, J. E., Froehlich, J. P., and Thomas, D. D. (1995) Conformational transitions of the sarcoplasmic reticulum Ca-ATPase studied by time-resolved EPR and quenched-flow kinetics, *Biochemistry 34*, 4864-4879.

60. Vilsen, B. (1995) Structure-function relationships in the Ca(2+)-ATPase of sarcoplasmic reticulum studied by use of the substrate analogue CrATP and site-directed mutagenesis. Comparison with the Na+,K(+)-ATPase, *Acta Physiol Scand Suppl 624*, 1-146.

61. Andersen, J. P., and Vilsen, B. (1995) Structure-function relationships of cation translocation by Ca(2+)- and Na+, K(+)-ATPases studied by site-directed mutagenesis, *FEBS Lett 359*, 101-106.

62. Brandl, C. J., Green, N. M., Korczak, B., and MacLennan, D. H. (1986) Two Ca2+ ATPase genes: homologies and mechanistic implications of deduced amino acid sequences, *Cell 44*, 597-607.

63. Brandl, C. J., deLeon, S., Martin, D. R., and MacLennan, D. H. (1987) Adult forms of the Ca2+ATPase of sarcoplasmic reticulum. Expression in developing skeletal muscle, *J Biol Chem 262*, 3768-3774.

64. MacLennan, D. H., Brandl, C. J., Korczak, B., and Green, N. M. (1985) Amino-acid sequence of a Ca2+ + Mg2+-dependent ATPase from rabbit muscle sarcoplasmic reticulum, deduced from its complementary DNA sequence, *Nature 316*, 696-700.

65. Periasamy, M., and Kalyanasundaram, A. (2007) SERCA pump isoforms: their role in calcium transport and disease, *Muscle Nerve 35*, 430-442.

66. Lytton, J., and MacLennan, D. H. (1988) Molecular cloning of cDNAs from human kidney coding for two alternatively spliced products of the cardiac Ca2+-ATPase gene, *J Biol Chem 263*, 15024-15031.

67. Lytton, J., Zarain-Herzberg, A., Periasamy, M., and MacLennan, D. H. (1989) Molecular cloning of the mammalian smooth muscle sarco(endo)plasmic reticulum Ca2+-ATPase, *J Biol Chem 264*, 7059-7065.

68. Anger, M., Samuel, J. L., Marotte, F., Wuytack, F., Rappaport, L., and Lompre, A. M. (1993) The sarco(endo)plasmic reticulum Ca(2+)-ATPase mRNA isoform, SERCA 3, is expressed in endothelial and epithelial cells in various organs, *FEBS Lett 334*, 45-48.

69. Wuytack, F., Papp, B., Verboomen, H., Raeymaekers, L., Dode, L., Bobe, R., Enouf, J., Bokkala, S., Authi, K. S., and Casteels, R. (1994) A sarco/endoplasmic reticulum Ca(2+)-ATPase 3-type Ca2+ pump is expressed in platelets, in lymphoid cells, and in mast cells, *J Biol Chem 269*, 1410-1416.

70. Lytton, J., Westlin, M., Burk, S. E., Shull, G. E., and MacLennan, D. H. (1992) Functional comparisons between isoforms of the sarcoplasmic or endoplasmic reticulum family of calcium pumps, *J Biol Chem 267*, 14483-14489.

71. Lytton, J., Westlin, M., and Hanley, M. R. (1991) Thapsigargin inhibits the sarcoplasmic or endoplasmic reticulum Ca-ATPase family of calcium pumps, *J Biol Chem 266*, 17067-17071.

72. Ji, Y., Loukianov, E., Loukianova, T., Jones, L. R., and Periasamy, M. (1999) SERCA1a can functionally substitute for SERCA2a in the heart, *Am J Physiol 276*, H89-97.

73. Toyoshima, C., and Nomura, H. (2002) Structural changes in the calcium pump accompanying the dissociation of calcium, *Nature 418*, 605-611.

74. Toyoshima, C., Asahi, M., Sugita, Y., Khanna, R., Tsuda, T., and MacLennan, D. H. (2003) Modeling of the inhibitory interaction of phospholamban with the Ca2+ ATPase, *Proc Natl Acad Sci U S A 100*, 467-472.

75. Toyoshima, C., Nakasako, M., Nomura, H., and Ogawa, H. (2000) Crystal structure of the calcium pump of sarcoplasmic reticulum at 2.6 A resolution, *Nature 405*, 647-655.

76. Sagara, Y., and Inesi, G. (1991) Inhibition of the sarcoplasmic reticulum Ca2+ transport ATPase by thapsigargin at subnanomolar concentrations, *J Biol Chem 266*, 13503-13506.

77. Takahashi, M., Kondou, Y., and Toyoshima, C. (2007) Interdomain communication in calcium pump as revealed in the crystal structures with transmembrane inhibitors, *Proc Natl Acad Sci U S A 104*, 5800-5805.

78. Olesen, C., Picard, M., Winther, A. M., Gyrup, C., Morth, J. P., Oxvig, C., Moller, J. V., and Nissen, P. (2007) The structural basis of calcium transport by the calcium pump, *Nature 450*, 1036-1042.

79. Winters, D. L., Autry, J. M., Svensson, B., and Thomas, D. D. (2008) Interdomain fluorescence resonance energy transfer in SERCA probed by cyan-fluorescent protein fused to the actuator domain, *Biochemistry 47*, 4246-4256.

80. Toyoshima, C., and Mizutani, T. (2004) Crystal structure of the calcium pump with a bound ATP analogue, *Nature 430*, 529-535.

81. Zamoon, J., Mascioni, A., Thomas, D. D., and Veglia, G. (2003) NMR solution structure and topological orientation of monomeric phospholamban in dodecylphosphocholine micelles, *Biophys J 85*, 2589-2598.

82. Metcalfe, E. E., Zamoon, J., Thomas, D. D., and Veglia, G. (2004) (1)H/(15)N heteronuclear NMR spectroscopy shows four dynamic domains for phospholamban reconstituted in dodecylphosphocholine micelles, *Biophys J 87*, 1205-1214.

83. **Karim, C. B., Stamm, J. D., Karim, J., Jones, L. R., and Thomas, D. D. (1998) Cysteine reactivity and oligomeric structures of phospholamban and its mutants, *Biochemistry 37*, 12074-12081.**

84. **Karim, C. B., Marquardt, C. G., Stamm, J. D., Barany, G., and Thomas, D. D. (2000) Synthetic null-cysteine phospholamban analogue and the corresponding transmembrane domain inhibit the Ca-ATPase, *Biochemistry 39*, 10892-10897.**

85. **Karim, C. B., Zhang, Z., Howard, E. C., Torgersen, K. D., and Thomas, D. D. (2006) Phosphorylation-dependent conformational switch in spin-labeled phospholamban bound to SERCA, *J Mol Biol 358*, 1032-1040.**

86. **Ha, K. N., Traaseth, N. J., Verardi, R., Zamoon, J., Cembran, A., Karim, C. B., Thomas, D. D., and Veglia, G. (2007) Controlling the inhibition of the sarcoplasmic Ca2+-ATPase by tuning phospholamban structural dynamics, *J Biol Chem 282*, 37205-37214.**

87. **Gustavsson, M., Traaseth, N. J., Karim, C. B., Lockamy, E. L., Thomas, D. D., and Veglia, G. Lipid-Mediated Folding/Unfolding of Phospholamban as a Regulatory Mechanism for the Sarcoplasmic Reticulum Ca(2+)-ATPase, *J Mol Biol 408*, 755-765.**

88. **Tatulian, S. A., Jones, L. R., Reddy, L. G., Stokes, D. L., and Tamm, L. K. (1995) Secondary structure and orientation of phospholamban reconstituted in supported bilayers from polarized attenuated total reflection FTIR spectroscopy, *Biochemistry 34*, 4448-4456.**

89. **Arkin, I. T., Rothman, M., Ludlam, C. F., Aimoto, S., Engelman, D. M., Rothschild, K. J., and Smith, S. O. (1995) Structural model of the phospholamban ion channel complex in phospholipid membranes, *J Mol Biol 248*, 824-834.**

90. **Oxenoid, K., and Chou, J. J. (2005) The structure of phospholamban pentamer reveals a channel-like architecture in membranes, *Proc Natl Acad Sci U S A 102*, 10870-10875.**

91. **Robia, S. L., Flohr, N. C., and Thomas, D. D. (2005) Phospholamban pentamer quaternary conformation determined by in-gel fluorescence anisotropy, *Biochemistry 44*, 4302-4311.**

92. **Traaseth, N. J., Verardi, R., Torgersen, K. D., Karim, C. B., Thomas, D. D., and Veglia, G. (2007) Spectroscopic validation of the pentameric structure of phospholamban, *Proc Natl Acad Sci U S A 104*, 14676-14681.**

93. **Robia, S. L., Campbell, K. S., Kelly, E. M., Hou, Z., Winters, D. L., and Thomas, D. D. (2007) Forster transfer recovery reveals that phospholamban exchanges slowly from pentamers but rapidly from the SERCA regulatory complex, *Circ Res 101*, 1123-1129.**

94. **Kelly, E. M., Hou, Z., Bossuyt, J., Bers, D. M., and Robia, S. L. (2008) Phospholamban oligomerization, quaternary structure, and sarco(endo)plasmic reticulum calcium ATPase binding measured by fluorescence resonance energy transfer in living cells, *J Biol Chem 283*, 12202-12211.**

95. **Traaseth, N. J., Shi, L., Verardi, R., Mullen, D. G., Barany, G., and Veglia, G. (2009) Structure and topology of monomeric phospholamban in lipid**

membranes determined by a hybrid solution and solid-state NMR approach, *Proc Natl Acad Sci U S A 106*, 10165-10170.

96. Hutter, M. C., Krebs, J., Meiler, J., Griesinger, C., Carafoli, E., and Helms, V. (2002) A structural model of the complex formed by phospholamban and the calcium pump of sarcoplasmic reticulum obtained by molecular mechanics, *Chembiochem 3*, 1200-1208.

97. Zamoon, J., Nitu, F., Karim, C., Thomas, D. D., and Veglia, G. (2005) Mapping the interaction surface of a membrane protein: unveiling the conformational switch of phospholamban in calcium pump regulation, *Proc Natl Acad Sci U S A 102*, 4747-4752.

98. Kirby, T. L., Karim, C. B., and Thomas, D. D. (2004) Electron paramagnetic resonance reveals a large-scale conformational change in the cytoplasmic domain of phospholamban upon binding to the sarcoplasmic reticulum Ca-ATPase, *Biochemistry 43*, 5842-5852.

99. Chien, K. R., Ross, J., Jr., and Hoshijima, M. (2003) Calcium and heart failure: the cycle game, *Nat Med 9*, 508-509.

100. Chen, Z., Akin, B. L., and Jones, L. R. (2007) Mechanism of reversal of phospholamban inhibition of the cardiac Ca2+-ATPase by protein kinase A and by anti-phospholamban monoclonal antibody 2D12, *J Biol Chem 282*, 20968-20976.

101. James, P., Inui, M., Tada, M., Chiesi, M., and Carafoli, E. (1989) Nature and site of phospholamban regulation of the Ca2+ pump of sarcoplasmic reticulum, *Nature 342*, 90-92.

102. Li, J., Bigelow, D. J., and Squier, T. C. (2004) Conformational changes within the cytosolic portion of phospholamban upon release of Ca-ATPase inhibition, *Biochemistry 43*, 3870-3879.

103. Mueller, B., Karim, C. B., Negrashov, I. V., Kutchai, H., and Thomas, D. D. (2004) Direct detection of phospholamban and sarcoplasmic reticulum Ca-ATPase interaction in membranes using fluorescence resonance energy transfer, *Biochemistry 43*, 8754-8765.

104. Bibert, S., Roy, S., Schaer, D., Horisberger, J. D., and Geering, K. (2008) Phosphorylation of phospholemman (FXYD1) by protein kinases A and C modulates distinct Na,K-ATPase isozymes, *J Biol Chem 283*, 476-486.

105. Teriete, P., Franzin, C. M., Choi, J., and Marassi, F. M. (2007) Structure of the Na,K-ATPase regulatory protein FXYD1 in micelles, *Biochemistry 46*, 6774-6783.

106. Morth, J. P., Pedersen, B. P., Toustrup-Jensen, M. S., Sorensen, T. L., Petersen, J., Andersen, J. P., Vilsen, B., and Nissen, P. (2007) Crystal structure of the sodium-potassium pump, *Nature 450*, 1043-1049.

107. Crambert, G., Fuzesi, M., Garty, H., Karlish, S., and Geering, K. (2002) Phospholemman (FXYD1) associates with Na,K-ATPase and regulates its transport properties, *Proc Natl Acad Sci U S A 99*, 11476-11481.

108. Beevers, A. J., and Kukol, A. (2006) Secondary structure, orientation, and oligomerization of phospholemman, a cardiac transmembrane protein, *Protein Sci 15*, 1127-1132.

109. Beevers, A. J., and Kukol, A. (2007) Phospholemman transmembrane structure reveals potential interactions with Na+/K+-ATPase, *J Biol Chem 282*, 32742-32748.
110. Traaseth, N. J., Thomas, D. D., and Veglia, G. (2006) Effects of Ser16 phosphorylation on the allosteric transitions of phospholamban/Ca(2+)-ATPase complex, *J Mol Biol 358*, 1041-1050.
111. Glaves, J. P., Trieber, C. A., Ceholski, D. K., Stokes, D. L., and Young, H. S. Phosphorylation and mutation of phospholamban alter physical interactions with the sarcoplasmic reticulum calcium pump, *J Mol Biol 405*, 707-723.
112. Odermatt, A., Taschner, P. E., Khanna, V. K., Busch, H. F., Karpati, G., Jablecki, C. K., Breuning, M. H., and MacLennan, D. H. (1996) Mutations in the gene-encoding SERCA1, the fast-twitch skeletal muscle sarcoplasmic reticulum Ca2+ ATPase, are associated with Brody disease, *Nat Genet 14*, 191-194.
113. Dhitavat, J., Dode, L., Leslie, N., Sakuntabhai, A., Lorette, G., and Hovnanian, A. (2003) Mutations in the sarcoplasmic/endoplasmic reticulum Ca2+ ATPase isoform cause Darier's disease, *J Invest Dermatol 121*, 486-489.
114. Varadi, A., Lebel, L., Hashim, Y., Mehta, Z., Ashcroft, S. J., and Turner, R. (1999) Sequence variants of the sarco(endo)plasmic reticulum Ca(2+)-transport ATPase 3 gene (SERCA3) in Caucasian type II diabetic patients (UK Prospective Diabetes Study 48), *Diabetologia 42*, 1240-1243.
115. Pan, Y., Zvaritch, E., Tupling, A. R., Rice, W. J., de Leon, S., Rudnicki, M., McKerlie, C., Banwell, B. L., and MacLennan, D. H. (2003) Targeted disruption of the ATP2A1 gene encoding the sarco(endo)plasmic reticulum Ca2+ ATPase isoform 1 (SERCA1) impairs diaphragm function and is lethal in neonatal mice, *J Biol Chem 278*, 13367-13375.
116. Periasamy, M., Reed, T. D., Liu, L. H., Ji, Y., Loukianov, E., Paul, R. J., Nieman, M. L., Riddle, T., Duffy, J. J., Doetschman, T., Lorenz, J. N., and Shull, G. E. (1999) Impaired cardiac performance in heterozygous mice with a null mutation in the sarco(endo)plasmic reticulum Ca2+-ATPase isoform 2 (SERCA2) gene, *J Biol Chem 274*, 2556-2562.
117. Liu, L. H., Paul, R. J., Sutliff, R. L., Miller, M. L., Lorenz, J. N., Pun, R. Y., Duffy, J. J., Doetschman, T., Kimura, Y., MacLennan, D. H., Hoying, J. B., and Shull, G. E. (1997) Defective endothelium-dependent relaxation of vascular smooth muscle and endothelial cell Ca2+ signaling in mice lacking sarco(endo)plasmic reticulum Ca2+-ATPase isoform 3, *J Biol Chem 272*, 30538-30545.
118. Seidman, J. G., and Seidman, C. (2001) The genetic basis for cardiomyopathy: from mutation identification to mechanistic paradigms, *Cell 104*, 557-567.
119. Schmitt, J. P., Kamisago, M., Asahi, M., Li, G. H., Ahmad, F., Mende, U., Kranias, E. G., MacLennan, D. H., Seidman, J. G., and Seidman, C. E. (2003) Dilated cardiomyopathy and heart failure caused by a mutation in phospholamban, *Science 299*, 1410-1413.
120. Ha, K. N., Masterson, L. R., Hou, Z., Verardi, R., Walsh, N., Veglia, G., and Robia, S. L. Lethal Arg9Cys phospholamban mutation hinders Ca2+-ATPase

regulation and phosphorylation by protein kinase A, *Proc Natl Acad Sci U S A 108*, 2735-2740.

121. Haghighi, K., Kolokathis, F., Pater, L., Lynch, R. A., Asahi, M., Gramolini, A. O., Fan, G. C., Tsiapras, D., Hahn, H. S., Adamopoulos, S., Liggett, S. B., Dorn, G. W., 2nd, MacLennan, D. H., Kremastinos, D. T., and Kranias, E. G. (2003) Human phospholamban null results in lethal dilated cardiomyopathy revealing a critical difference between mouse and human, *J Clin Invest 111*, 869-876.

122. Haghighi, K., Kolokathis, F., Gramolini, A. O., Waggoner, J. R., Pater, L., Lynch, R. A., Fan, G. C., Tsiapras, D., Parekh, R. R., Dorn, G. W., 2nd, MacLennan, D. H., Kremastinos, D. T., and Kranias, E. G. (2006) A mutation in the human phospholamban gene, deleting arginine 14, results in lethal, hereditary cardiomyopathy, *Proc Natl Acad Sci U S A 103*, 1388-1393.

123. Roger, V. L., Go, A. S., Lloyd-Jones, D. M., Adams, R. J., Berry, J. D., Brown, T. M., Carnethon, M. R., Dai, S., de Simone, G., Ford, E. S., Fox, C. S., Fullerton, H. J., Gillespie, C., Greenlund, K. J., Hailpern, S. M., Heit, J. A., Ho, P. M., Howard, V. J., Kissela, B. M., Kittner, S. J., Lackland, D. T., Lichtman, J. H., Lisabeth, L. D., Makuc, D. M., Marcus, G. M., Marelli, A., Matchar, D. B., McDermott, M. M., Meigs, J. B., Moy, C. S., Mozaffarian, D., Mussolino, M. E., Nichol, G., Paynter, N. P., Rosamond, W. D., Sorlie, P. D., Stafford, R. S., Turan, T. N., Turner, M. B., Wong, N. D., and Wylie-Rosett, J. Heart disease and stroke statistics--2011 update: a report from the American Heart Association, *Circulation 123*, e18-e209.

124. Lipskaia, L., Chemaly, E. R., Hadri, L., Lompre, A. M., and Hajjar, R. J. Sarcoplasmic reticulum Ca(2+) ATPase as a therapeutic target for heart failure, *Expert Opin Biol Ther 10*, 29-41.

125. Giordano, F. J., He, H., McDonough, P., Meyer, M., Sayen, M. R., and Dillmann, W. H. (1997) Adenovirus-mediated gene transfer reconstitutes depressed sarcoplasmic reticulum Ca2+-ATPase levels and shortens prolonged cardiac myocyte Ca2+ transients, *Circulation 96*, 400-403.

126. Zarain-Herzberg, A., Afzal, N., Elimban, V., and Dhalla, N. S. (1996) Decreased expression of cardiac sarcoplasmic reticulum Ca(2+)-pump ATPase in congestive heart failure due to myocardial infarction, *Mol Cell Biochem 163-164*, 285-290.

127. Kawase, Y., Ly, H. Q., Prunier, F., Lebeche, D., Shi, Y., Jin, H., Hadri, L., Yoneyama, R., Hoshino, K., Takewa, Y., Sakata, S., Peluso, R., Zsebo, K., Gwathmey, J. K., Tardif, J. C., Tanguay, J. F., and Hajjar, R. J. (2008) Reversal of cardiac dysfunction after long-term expression of SERCA2a by gene transfer in a pre-clinical model of heart failure, *J Am Coll Cardiol 51*, 1112-1119.

128. Jaski, B. E., Jessup, M. L., Mancini, D. M., Cappola, T. P., Pauly, D. F., Greenberg, B., Borow, K., Dittrich, H., Zsebo, K. M., and Hajjar, R. J. (2009) Calcium upregulation by percutaneous administration of gene therapy in cardiac disease (CUPID Trial), a first-in-human phase 1/2 clinical trial, *J Card Fail 15*, 171-181.

129. Hoshijima, M., Ikeda, Y., Iwanaga, Y., Minamisawa, S., Date, M. O., Gu, Y., Iwatate, M., Li, M., Wang, L., Wilson, J. M., Wang, Y., Ross, J., Jr., and Chien, K. R. (2002) Chronic suppression of heart-failure progression by a pseudophosphorylated mutant of phospholamban via in vivo cardiac rAAV gene delivery, *Nat Med 8*, 864-871.

130. del Monte, F., Harding, S. E., Dec, G. W., Gwathmey, J. K., and Hajjar, R. J. (2002) Targeting phospholamban by gene transfer in human heart failure, *Circulation 105*, 904-907.

131. Iwanaga, Y., Hoshijima, M., Gu, Y., Iwatate, M., Dieterle, T., Ikeda, Y., Date, M. O., Chrast, J., Matsuzaki, M., Peterson, K. L., Chien, K. R., and Ross, J., Jr. (2004) Chronic phospholamban inhibition prevents progressive cardiac dysfunction and pathological remodeling after infarction in rats, *J Clin Invest 113*, 727-736.

132. Meyer, M., Belke, D. D., Trost, S. U., Swanson, E., Dieterle, T., Scott, B., Cary, S. P., Ho, P., Bluhm, W. F., McDonough, P. M., Silverman, G. J., and Dillmann, W. H. (2004) A recombinant antibody increases cardiac contractility by mimicking phospholamban phosphorylation, *Faseb J 18*, 1312-1314.

133. Minamisawa, S., Hoshijima, M., Chu, G., Ward, C. A., Frank, K., Gu, Y., Martone, M. E., Wang, Y., Ross, J., Jr., Kranias, E. G., Giles, W. R., and Chien, K. R. (1999) Chronic phospholamban-sarcoplasmic reticulum calcium ATPase interaction is the critical calcium cycling defect in dilated cardiomyopathy, *Cell 99*, 313-322.

134. Kimura, Y., Kurzydlowski, K., Tada, M., and MacLennan, D. H. (1997) Phospholamban inhibitory function is activated by depolymerization, *J Biol Chem 272*, 15061-15064.

135. Campbell, I. D., and Dwek, R.A. (1984) Biological Spectroscopy, The Benjamin/Cummings Publishing Company, Inc, Reading, Massachusetts.

136. Stryer, L. (1978) Fluorescence energy transfer as a spectroscopic ruler, *Annu Rev Biochem 47*, 819-846.

137. Cantilina, T., Sagara, Y., Inesi, G., and Jones, L. R. (1993) Comparative studies of cardiac and skeletal sarcoplasmic reticulum ATPases. Effect of a phospholamban antibody on enzyme activation by Ca2+, *J Biol Chem 268*, 17018-17025.

138. Simmerman, H. K., Kobayashi, Y. M., Autry, J. M., and Jones, L. R. (1996) A leucine zipper stabilizes the pentameric membrane domain of phospholamban and forms a coiled-coil pore structure, *J Biol Chem 271*, 5941-5946.

139. Chen, Z., Stokes, D. L., and Jones, L. R. (2005) Role of leucine 31 of phospholamban in structural and functional interactions with the Ca2+ pump of cardiac sarcoplasmic reticulum, *J Biol Chem 280*, 10530-10539.

140. Kaye, D. M., Preovolos, A., Marshall, T., Byrne, M., Hoshijima, M., Hajjar, R., Mariani, J. A., Pepe, S., Chien, K. R., and Power, J. M. (2007) Percutaneous cardiac recirculation-mediated gene transfer of an inhibitory phospholamban peptide reverses advanced heart failure in large animals, *J Am Coll Cardiol 50*, 253-260.

141. Stokes, D. L., and Green, N. M. (1990) Three-dimensional crystals of CaATPase from sarcoplasmic reticulum. Symmetry and molecular packing, *Biophys J 57*, 1-14.
142. Vanderkooi, J. M., Ierokomas, A., Nakamura, H., and Martonosi, A. (1977) Fluorescence energy transfer between Ca2+ transport ATPase molecules in artificial membranes, *Biochemistry 16*, 1262-1267.
143. Reddy, L. G., Autry, J. M., Jones, L. R., and Thomas, D. D. (1999) Co-reconstitution of phospholamban mutants with the Ca-ATPase reveals dependence of inhibitory function on phospholamban structure, *J Biol Chem 274*, 7649-7655.
144. Reddy, L. G., Cornea, R. L., Winters, D. L., McKenna, E., and Thomas, D. D. (2003) Defining the molecular components of calcium transport regulation in a reconstituted membrane system, *Biochemistry 42*, 4585-4592.
145. Reddy, L. G., Jones, L. R., Pace, R. C., and Stokes, D. L. (1996) Purified, reconstituted cardiac Ca2+-ATPase is regulated by phospholamban but not by direct phosphorylation with Ca2+/calmodulin-dependent protein kinase, *J Biol Chem 271*, 14964-14970.
146. Karim, C. B., Paterlini, M. G., Reddy, L. G., Hunter, G. W., Barany, G., and Thomas, D. D. (2001) Role of cysteine residues in structural stability and function of a transmembrane helix bundle, *J Biol Chem 276*, 38814-38819.
147. Ferrington, D. A., Moewe, P., Yao, Q., and Bigelow, D. (1998) Comparison of the stoichiometery of phospholamban to SERCA2a in cardiac and skeletal muscle, *Biophys J 74*, 356-361.
148. Cornea, R. L., Autry, J. M., Chen, Z., and Jones, L. R. (2000) Reexamination of the role of the leucine/isoleucine zipper residues of phospholamban in inhibition of the Ca2+ pump of cardiac sarcoplasmic reticulum, *J Biol Chem 275*, 41487-41494.
149. Zvaritch, E., Backx, P. H., Jirik, F., Kimura, Y., de Leon, S., Schmidt, A. G., Hoit, B. D., Lester, J. W., Kranias, E. G., and MacLennan, D. H. (2000) The transgenic expression of highly inhibitory monomeric forms of phospholamban in mouse heart impairs cardiac contractility, *J Biol Chem 275*, 14985-14991.
150. Toyofuku, T., Kurzydlowski, K., Tada, M., and MacLennan, D. H. (1994) Amino acids Glu2 to Ile18 in the cytoplasmic domain of phospholamban are essential for functional association with the Ca(2+)-ATPase of sarcoplasmic reticulum, *J Biol Chem 269*, 3088-3094.
151. Meyer, M., Schillinger, W., Pieske, B., Holubarsch, C., Heilmann, C., Posival, H., Kuwajima, G., Mikoshiba, K., Just, H., Hasenfuss, G., and et al. (1995) Alterations of sarcoplasmic reticulum proteins in failing human dilated cardiomyopathy, *Circulation 92*, 778-784.
152. Dash, R., Frank, K. F., Carr, A. N., Moravec, C. S., and Kranias, E. G. (2001) Gender influences on sarcoplasmic reticulum Ca2+-handling in failing human myocardium, *J Mol Cell Cardiol 33*, 1345-1353.
153. Jensen, A. M., Sorensen, T. L., Olesen, C., Moller, J. V., and Nissen, P. (2006) Modulatory and catalytic modes of ATP binding by the calcium pump, *Embo J 25*, 2305-2314.

154. Moncoq, K., Trieber, C. A., and Young, H. S. (2007) The molecular basis for cyclopiazonic acid inhibition of the sarcoplasmic reticulum calcium pump, *J Biol Chem 282*, 9748-9757.
155. Denessiouk, K. A., Rantanen, V. V., and Johnson, M. S. (2001) Adenine recognition: a motif present in ATP-, CoA-, NAD-, NADP-, and FAD-dependent proteins, *Proteins 44*, 282-291.
156. Mao, L., Wang, Y., Liu, Y., and Hu, X. (2003) Multiple intermolecular interaction modes of positively charged residues with adenine in ATP-binding proteins, *J Am Chem Soc 125*, 14216-14217.
157. Kast, D., Espinoza-Fonseca, L. M., Yi, C., and Thomas, D. D. Phosphorylation-induced structural changes in smooth muscle myosin regulatory light chain, *Proc Natl Acad Sci U S A 107*, 8207-8212.
158. Muretta, J. M., Kyrychenko, A., Ladokhin, A. S., Kast, D. J., Gillispie, G. D., and Thomas, D. D. High-performance time-resolved fluorescence by direct waveform recording, *Rev Sci Instrum 81*, 103101.
159. Toyoshima, C., Yonekura, S., Tsueda, J., and Iwasawa, S. Trinitrophenyl derivatives bind differently from parent adenine nucleotides to Ca2+-ATPase in the absence of Ca2+, *Proc Natl Acad Sci U S A 108*, 1833-1838.
160. Asher, G., Reuven, N., and Shaul, Y. (2006) 20S proteasomes and protein degradation "by default", *Bioessays 28*, 844-849.
161. Goldberg, A. L. (2003) Protein degradation and protection against misfolded or damaged proteins, *Nature 426*, 895-899.
162. Davies, K. J. (2001) Degradation of oxidized proteins by the 20S proteasome, *Biochimie 83*, 301-310.
163. Hochstrasser, M. (1996) Ubiquitin-dependent protein degradation, *Annu Rev Genet 30*, 405-439.
164. Wang, T. (2003) The 26S proteasome system in the signaling pathways of TGF-beta superfamily, *Front Biosci 8*, d1109-1127.
165. Jesenberger, V., and Jentsch, S. (2002) Deadly encounter: ubiquitin meets apoptosis, *Nat Rev Mol Cell Biol 3*, 112-121.
166. Kisselev, A. F., Akopian, T. N., Woo, K. M., and Goldberg, A. L. (1999) The sizes of peptides generated from protein by mammalian 26 and 20 S proteasomes. Implications for understanding the degradative mechanism and antigen presentation, *J Biol Chem 274*, 3363-3371.
167. Takeuchi, J., Chen, H., Hoyt, M. A., and Coffino, P. (2008) Structural elements of the ubiquitin-independent proteasome degron of ornithine decarboxylase, *Biochem J 410*, 401-407.
168. Acquaviva, C., Brockly, F., Ferrara, P., Bossis, G., Salvat, C., Jariel-Encontre, I., and Piechaczyk, M. (2001) Identification of a C-terminal tripeptide motif involved in the control of rapid proteasomal degradation of c-Fos proto-oncoprotein during the G(0)-to-S phase transition, *Oncogene 20*, 7563-7572.
169. Tarcsa, E., Szymanska, G., Lecker, S., O'Connor, C. M., and Goldberg, A. L. (2000) Ca2+-free calmodulin and calmodulin damaged by in vitro aging are selectively degraded by 26 S proteasomes without ubiquitination, *J Biol Chem 275*, 20295-20301.

170. Benaroudj, N., Tarcsa, E., Cascio, P., and Goldberg, A. L. (2001) The unfolding of substrates and ubiquitin-independent protein degradation by proteasomes, *Biochimie 83*, 311-318.
171. Reinheckel, T., Sitte, N., Ullrich, O., Kuckelkorn, U., Davies, K. J., and Grune, T. (1998) Comparative resistance of the 20S and 26S proteasome to oxidative stress, *Biochem J 335 (Pt 3)*, 637-642.
172. Pacifici, R. E., Kono, Y., and Davies, K. J. (1993) Hydrophobicity as the signal for selective degradation of hydroxyl radical-modified hemoglobin by the multicatalytic proteinase complex, proteasome, *J Biol Chem 268*, 15405-15411.
173. Giulivi, C., Pacifici, R. E., and Davies, K. J. (1994) Exposure of hydrophobic moieties promotes the selective degradation of hydrogen peroxide-modified hemoglobin by the multicatalytic proteinase complex, proteasome, *Arch Biochem Biophys 311*, 329-341.
174. Friguet, B., Szweda, L. I., and Stadtman, E. R. (1994) Susceptibility of glucose-6-phosphate dehydrogenase modified by 4-hydroxy-2-nonenal and metal-catalyzed oxidation to proteolysis by the multicatalytic protease, *Arch Biochem Biophys 311*, 168-173.
175. Ferrington, D. A., Sun, H., Murray, K. K., Costa, J., Williams, T. D., Bigelow, D. J., and Squier, T. C. (2001) Selective degradation of oxidized calmodulin by the 20 S proteasome, *J Biol Chem 276*, 937-943.
176. Yamniuk, A. P., and Vogel, H. J. (2004) Calmodulin's flexibility allows for promiscuity in its interactions with target proteins and peptides, *Mol Biotechnol 27*, 33-57.
177. Ferrington, D. A., Husom, A. D., and Thompson, L. V. (2005) Altered proteasome structure, function, and oxidation in aged muscle, *Faseb J 19*, 644-646.
178. Sacksteder, C. A., Whittier, J. E., Xiong, Y., Li, J., Galeva, N. A., Jacoby, M. E., Purvine, S. O., Williams, T. D., Rechsteiner, M. C., Bigelow, D. J., and Squier, T. C. (2006) Tertiary structural rearrangements upon oxidation of Methionine145 in calmodulin promotes targeted proteasomal degradation, *Biophys J 91*, 1480-1493.
179. Strosova, M., Voss, P., Engels, M., Horakova, L., and Grune, T. (2008) Limited degradation of oxidized calmodulin by proteasome: formation of peptides, *Arch Biochem Biophys 475*, 50-54.
180. Gopalakrishna, R., and Anderson, W. B. (1982) Ca2+-induced hydrophobic site on calmodulin: application for purification of calmodulin by phenyl-Sepharose affinity chromatography, *Biochem Biophys Res Commun 104*, 830-836.
181. Strasburg, G. M., Hogan, M., Birmachu, W., Thomas, D. D., and Louis, C. F. (1988) Site-specific derivatives of wheat germ calmodulin. Interactions with troponin and sarcoplasmic reticulum, *J Biol Chem 263*, 542-548.
182. Chen, Y. H., Yang, J. T., and Chau, K. H. (1974) Determination of the helix and beta form of proteins in aqueous solution by circular dichroism, *Biochemistry 13*, 3350-3359.

183. Saxena, V. P., and Wetlaufer, D. B. (1971) A new basis for interpreting the circular dichroic spectra of proteins, *Proc Natl Acad Sci U S A 68*, 969-972.
184. Greenfield, N., and Fasman, G. D. (1969) Computed circular dichroism spectra for the evaluation of protein conformation, *Biochemistry 8*, 4108-4116.
185. Balog, E. M., Norton, L. E., Bloomquist, R. A., Cornea, R. L., Black, D. J., Louis, C. F., Thomas, D. D., and Fruen, B. R. (2003) Calmodulin oxidation and methionine to glutamine substitutions reveal methionine residues critical for functional interaction with ryanodine receptor-1, *J Biol Chem 278*, 15615-15621.
186. Chu, A., Diaz-Munoz, M., Hawkes, M. J., Brush, K., and Hamilton, S. L. (1990) Ryanodine as a probe for the functional state of the skeletal muscle sarcoplasmic reticulum calcium release channel, *Mol Pharmacol 37*, 735-741.
187. Meissner, G., and el-Hashem, A. (1992) Ryanodine as a functional probe of the skeletal muscle sarcoplasmic reticulum Ca2+ release channel, *Mol Cell Biochem 114*, 119-123.
188. Brooks, S. P., and Storey, K. B. (1992) Bound and determined: a computer program for making buffers of defined ion concentrations, *Anal Biochem 201*, 119-126.
189. Rechsteiner, M., and Rogers, S. W. (1996) PEST sequences and regulation by proteolysis, *Trends Biochem Sci 21*, 267-271.
190. Cardamone, M., and Puri, N. K. (1992) Spectrofluorimetric assessment of the surface hydrophobicity of proteins, *Biochem J 282 (Pt 2)*, 589-593.
191. O'Neil, K. T., and DeGrado, W. F. (1985) A predicted structure of calmodulin suggests an electrostatic basis for its function, *Proc Natl Acad Sci U S A 82*, 4954-4958.
192. O'Neil, K. T., and DeGrado, W. F. (1990) How calmodulin binds its targets: sequence independent recognition of amphiphilic alpha-helices, *Trends Biochem Sci 15*, 59-64.
193. Gellman, S. H. (1991) On the role of methionine residues in the sequence-independent recognition of nonpolar protein surfaces, *Biochemistry 30*, 6633-6636.
194. Masino, L., Martin, S. R., and Bayley, P. M. (2000) Ligand binding and thermodynamic stability of a multidomain protein, calmodulin, *Protein Sci 9*, 1519-1529.
195. Dayhoff, M. O. (1978) Atlas of Protein Sequence and Structure, Vol. 5, National Biomedical Research Foundation, Washington, D.C.
196. Sharp, K. A., Nicholls, A., Friedman, R., and Honig, B. (1991) Extracting hydrophobic free energies from experimental data: relationship to protein folding and theoretical models, *Biochemistry 30*, 9686-9697.
197. Kenniston, J. A., and Sauer, R. T. (2004) Signaling degradation, *Nat Struct Mol Biol 11*, 800-802.
198. Prakash, S., Tian, L., Ratliff, K. S., Lehotzky, R. E., and Matouschek, A. (2004) An unstructured initiation site is required for efficient proteasome-mediated degradation, *Nat Struct Mol Biol 11*, 830-837.

199. Janse, D. M., Crosas, B., Finley, D., and Church, G. M. (2004) Localization to the proteasome is sufficient for degradation, *J Biol Chem 279*, 21415-21420.
200. Whittier, J. E., Xiong, Y., Rechsteiner, M. C., and Squier, T. C. (2004) Hsp90 enhances degradation of oxidized calmodulin by the 20 S proteasome, *J Biol Chem 279*, 46135-46142.
201. Asher, G., Tsvetkov, P., Kahana, C., and Shaul, Y. (2005) A mechanism of ubiquitin-independent proteasomal degradation of the tumor suppressors p53 and p73, *Genes Dev 19*, 316-321.
202. Liu, C. W., Corboy, M. J., DeMartino, G. N., and Thomas, P. J. (2003) Endoproteolytic activity of the proteasome, *Science 299*, 408-411.
203. Yin, D., Sun, H., Ferrington, D. A., and Squier, T. C. (2000) Closer proximity between opposing domains of vertebrate calmodulin following deletion of Met(145)-Lys(148), *Biochemistry 39*, 10255-10268.
204. Navon, A., and Goldberg, A. L. (2001) Proteins are unfolded on the surface of the ATPase ring before transport into the proteasome, *Mol Cell 8*, 1339-1349.
205. Zak, R., Martin, A. F., Prior, G., and Rabinowitz, M. (1977) Comparison of turnover of several myofibrillar proteins and critical evaluation of double isotope method, *J Biol Chem 252*, 3430-3435.
206. Peterson-von Gehr, J. a. J., HP. (1982) in *12 Int. Congr. Biochem.*
207. Ferrington, D. A., Chen, X., Krainev, A. G., Michaelis, E. K., and Bigelow, D. J. (1997) Protein half-lives of calmodulin and the plasma membrane Ca-ATPase in rat brain, *Biochem Biophys Res Commun 237*, 163-165.
208. Ferrington, D. A., Krainev, A. G., and Bigelow, D. J. (1998) Altered turnover of calcium regulatory proteins of the sarcoplasmic reticulum in aged skeletal muscle, *J Biol Chem 273*, 5885-5891.
209. Voges, D., Zwickl, P., and Baumeister, W. (1999) The 26S proteasome: a molecular machine designed for controlled proteolysis, *Annu Rev Biochem 68*, 1015-1068.
210. Rape, M., and Jentsch, S. (2002) Taking a bite: proteasomal protein processing, *Nat Cell Biol 4*, E113-116.
211. Lee, C., Schwartz, M. P., Prakash, S., Iwakura, M., and Matouschek, A. (2001) ATP-dependent proteases degrade their substrates by processively unraveling them from the degradation signal, *Mol Cell 7*, 627-637.
212. Schumacher, M. A., Rivard, A. F., Bachinger, H. P., and Adelman, J. P. (2001) Structure of the gating domain of a Ca2+-activated K+ channel complexed with Ca2+/calmodulin, *Nature 410*, 1120-1124.
213. Drum, C. L., Yan, S. Z., Bard, J., Shen, Y. Q., Lu, D., Soelaiman, S., Grabarek, Z., Bohm, A., and Tang, W. J. (2002) Structural basis for the activation of anthrax adenylyl cyclase exotoxin by calmodulin, *Nature 415*, 396-402.
214. Balog, E. M., Norton, L. E., Thomas, D. D., and Fruen, B. R. (2006) Role of calmodulin methionine residues in mediating productive association with cardiac ryanodine receptors, *Am J Physiol Heart Circ Physiol 290*, H794-799.
215. Yao, Y., Yin, D., Jas, G. S., Kuczer, K., Williams, T. D., Schoneich, C., and Squier, T. C. (1996) Oxidative modification of a carboxyl-terminal vicinal

methionine in calmodulin by hydrogen peroxide inhibits calmodulin-dependent activation of the plasma membrane Ca-ATPase, *Biochemistry 35*, 2767-2787.

216. Bartlett, R. K., Bieber Urbauer, R. J., Anbanandam, A., Smallwood, H. S., Urbauer, J. L., and Squier, T. C. (2003) Oxidation of Met144 and Met145 in calmodulin blocks calmodulin dependent activation of the plasma membrane Ca-ATPase, *Biochemistry 42*, 3231-3238.

217. Boschek, C. B., Jones, T. E., Smallwood, H. S., Squier, T. C., and Bigelow, D. J. (2008) Loss of the calmodulin-dependent inhibition of the RyR1 calcium release channel upon oxidation of methionines in calmodulin, *Biochemistry 47*, 131-142.

218. Gao, J., Yin, D., Yao, Y., Williams, T. D., and Squier, T. C. (1998) Progressive decline in the ability of calmodulin isolated from aged brain to activate the plasma membrane Ca-ATPase, *Biochemistry 37*, 9536-9548.

219. Keller, J. N., Hanni, K. B., and Markesbery, W. R. (2000) Possible involvement of proteasome inhibition in aging: implications for oxidative stress, *Mech Ageing Dev 113*, 61-70.

220. Asahi, M., Kimura, Y., Kurzydlowski, K., Tada, M., and MacLennan, D. H. (1999) Transmembrane helix M6 in sarco(endo)plasmic reticulum Ca(2+)-ATPase forms a functional interaction site with phospholamban. Evidence for physical interactions at other sites, *J Biol Chem 274*, 32855-32862.

221. Madden, T. D., Chapman, D., and Quinn, P. J. (1979) Cholesterol modulates activity of calcium-dependent ATPase of the sarcoplasmic reticulum, *Nature 279*, 538-541.

222. Fabiato, A., and Fabiato, F. (1979) Calculator programs for computing the composition of the solutions containing multiple metals and ligands used for experiments in skinned muscle cells, *J Physiol (Paris) 75*, 463-505.

APPENDIX 1 – Dabcyl Masks the Effect of PLB Phosphorylation

A1.1 Introduction

In heart muscle, calcium translocation into the sarcoplasmic reticulum (SR) by the Ca^{2+}-ATPase (SERCA) is regulated by phospholamban (PLB), a 52-residue membrane protein that inhibits SERCA at submicromolar [Ca^{2+}] (*5*). Reversal of inhibition can be achieved by micromolar [Ca^{2+}] or β-adrenergic stimulation of PLB phosphorylation by protein kinase A (PKA) (*5, 11, 99*). PLB inhibits SERCA through tight physical interaction between the two proteins (*5, 220*). However, the mechanism responsible for reversal of inhibition remains quite controversial.

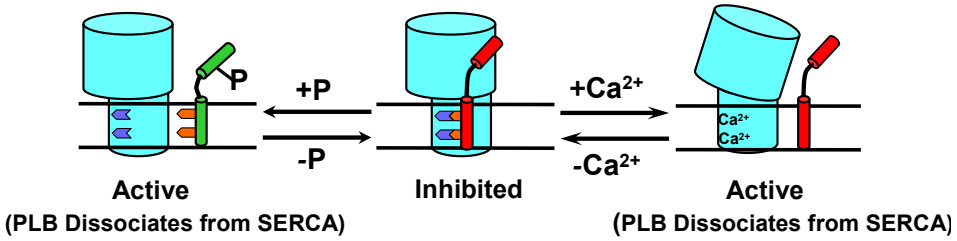

Figure 36: Dissociation Model of SERCA Regulation by PLB. Complete dissociation of PLB from SERCA is required for relief of inhibition.

The original goal of this project was to investigate molecular mechanisms of SERCA regulation by PLB, by studying the effects of phosphorylation of PLB and micromolar Ca^{2+}. We used AEDANS-SERCA with DABCYL-PLB in known lipid compositions to test the dissociation model of SERCA regulation by PLB (Figure 36). However, the use of the fluorescent probe, DABCYL, limited this work, and project shifted to examining the effect of DABCYL on PLB phosphorylation.

A1.2 Materials and Methods

SERCA Purification and Labeling. SERCA was isolated from New Zealand White Rabbit skeletal muscle and purified using Reactive Red method in 0.01% $C_{12}E_8$ (*141*). Aliquots were flash frozen and stored at -80°C until further use. For labeling, detergent was removed with Biobeads SM2 (37.5 mg/mg) stirring for three hours. SERCA (18.2 μM) was labeled with IAEDANS (364 μM) for 30 min at 25°C in the dark (labeling buffer: 80 mM KCl, 5 mM $MgCl_2$, 1 mM $CaCl_2$, 20 mM MOPS, pH 6.8). Excess dye was removed by washing two times with wash buffer (20 mM sucrose, 100 mM KCl, 20 mM MOPS, pH 7.0) (*103*). Concentration of IAEDANS was determined from absorbance at ε_{334nm} = 6100 M^{-1} cm^{-1} after treatment with 0.1 M NaOH and 1% SDS) (*142*). Concentration of protein was determined by the BCA assay using BSA as a standard. Aliquots were flash frozen and stored at -80°C until usage in co-reconstitution for ATPase and FRET assays.

Synthesis and Purification of AFA PLB. Using Fmoc chemistry, PLB was synthesized with Fmoc-Leu-PEG-PS resin with a PE Biosystems PioneerTM peptide synthesis instrument (*103*). The residues Cys 36, Cys 41, and Cys 46 were replaced with residues Ala, Phe, and Ala (AFA) respectively to ensure monomer formation of PLB. ESI and amino acid analysis were used to confirm the peptide concentration and sequence of each PLB mutant. AFA was dissolved in TFE and stored at -20°C until co-reconstitution.

Phosphorylation of PLB by PKA. HPLC-purified Ac-AFA-PLB was dissolved in 20 mM MOPS with 1% β-OG at pH 7.2 for a final PLB concentration of 0.3 mg/mL. Next, 1 mM $MgCl_2$, 1,000 IU PKA, and 1 mM ATP were added to the mixture in that

order. Samples were incubated overnight at 30°C for ~16 hours. After incubation, samples were purified using HPLC with a C_8 column. Phosphorylation of PLB was confirmed using ESI mass spectrometry.

DABCYL Labeling of Phosphorylated PLB. HPLC-purified Ac-pSer16-AFA-PLB (0.3 μmol) was labeled with DABCYL (0.6 μmol) in 100 mM $NaHCO_3$ containing 1% SDS at pH 9.0. Samples were shaken overnight at 25°C and then flash frozen to stop the labeling reaction. Samples were then purified using HPLC with a diphenyl column. DABCYL labeling of PLB was confirmed using ESI mass spectrometry. Concentration of DABCYL was determined from absorbance at ε_{453nm} = 32,000 M^{-1} cm^{-1} in TFE. Protein concentration was measured utilizing a BCA assay with BSA as a standard.

Co-reconstitution of SERCA and PLB. As previously reported, SERCA was co-reconstituted with PLB at 700/1 lipid/SERCA molar ratio and varying amounts PLB/SERCA molar ratios (*103*). The desired amount of PLB in TFE and lipids (4:1 DOPC:DOPE weight ratio) were mixed with an equal volume of methanol (*143, 144*). These samples were dried using a rotovap to remove solvent and to create a thin film. To ensure all solvent was removed, the PLB-lipid samples were stored overnight in a vacuum desiccator. PLB-lipid sample were solubilized in buffer (5 mM MgCl2, 0.1M KCl, 10% glycerol, 20 mM MOPS, pH 7.0) by vortexing and mild sonication for 55 sec to form unilamellar vesicles; afterwards, $C_{12}E_8$ (2 mg/mg lipid) was added. Co-reconstituted samples contained 50 μg of purified IAEDANS-SERCA and varying molar ratios of PLB. Detergent was removed with Biobeads (37.5 mg/mg C12E8) for three hours. Ca^{2+}-ATPase and FRET measurements were taken immediately after co-reconstitution.

Ca^{2+}-ATPase Functional Measurements. Ca^{2+}-ATPase activity was determined using a NADH-enzyme linked microtiter plate assay (*221*) with the [Ca^{2+}] prepared with EGTA buffering (*222*). Activity was determined by the decrease in absorbance at 340 nm, corresponding to the decrease in [NADH], with a SpectroMax Plus 384 microplate reader (Molecular Devices, Sunnyvale, CA). To prevent build up of Ca^{2+} in the vesicles, ionophore A23187 was used. Data were plotted V vs. pCa, fitted to a Hill equation, $V = V_{max}/[1+ 10^{-n\ (pKCa\ -\ pCa)}]$, and normalized to maximal rate, V_{max}, which was obtained from the fit. Replots of the data were used to determine the shift in pK_{Ca}.

A1.3 Results

Characterization of Labeled Proteins. The dye-to-protein molar ratio of AEDANS-SERCA was calculated to be 0.92 ± 0.09. Labeled SERCA, reconstituted into lipid membranes, maintained 80% of its Ca-ATPase activity and all of its sensitivity to PLB inhibition. ESI mass spectrometry was used to confirm that PLB had been phosphorylated and labeled with DABCYL. The labeling efficiency of DABCYL PLBs was calculated from concentrations from BCA assays and absorbance readings at 453 nm. The dye-to-protein molar ratios for DABCYL-AFA-PLB was 0.93 ± 0.17 and DABCYL-pAFA-PLB was 1.4.

The effect of DABCYL on Ca-ATPase activity was studied previously in Mueller et al (*103*). They found that DABCYL did not effect the inhibition of mutants in their research. However, they were not investigating the effect of phosphorylation. In the current study, we began looking at effect of PLB phosphorylation as a relief mechanism of SERCA inhibition. We found that DABYCL masked the effect of phosphorylation of PLB even though PLB was fully phosphorylated before labeling (Compare Figure 37A&B). Phosphorylation of unlabeled AFA resulted in ~ 70% relief of inhibition compared to labeled phosphorylated PLB mutants that only had 30% relief of inhibition (Figure 38).

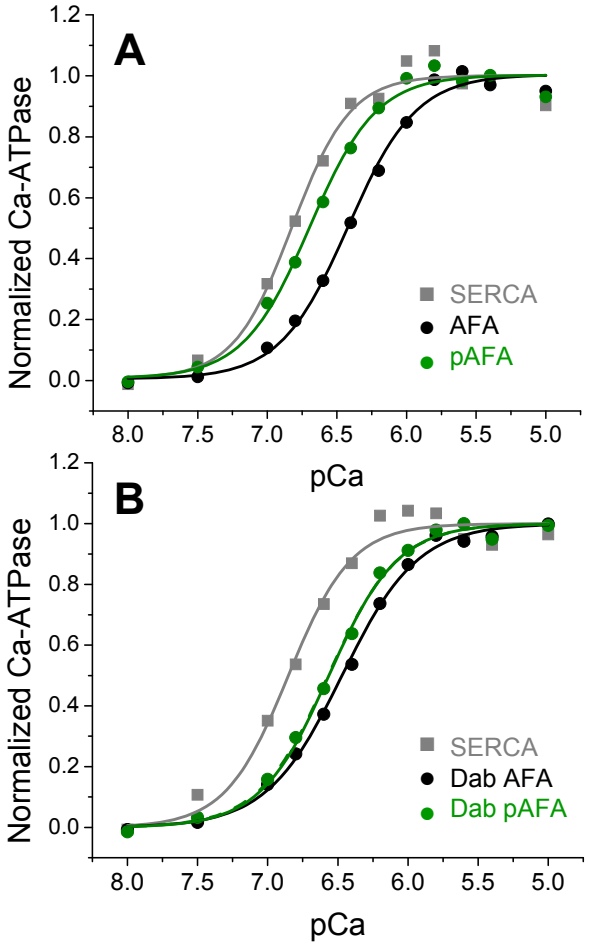

Figure 37: Effect of Phosphorylation on Inhibition. A) Normalized Ca-ATPase curves of unlabeled SERCA and AFA fitted with Hill Equation. B) Normalized Ca-ATPase curves of AFA labeled with DABCYL. Data represent the mean ± standard error of 4 separate trials.

A1.4 Discussion and Future Directions

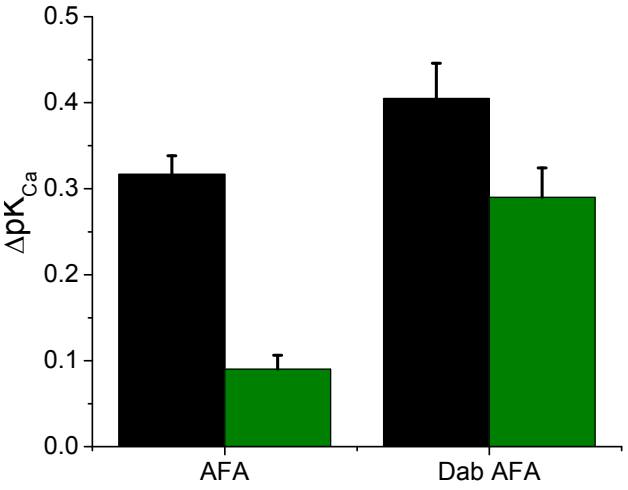

Figure 38: Comparison of Effect of Phosphorylation on Unlabeled and Labeled AFA. Black bars represent unphosphorylated AFA while green bars represent phosphorylated AFA. Data represent the mean ± standard error of 4 separate trials.

Due to limits of this probe, we were unable to investigate the original goal of studying relief mechanism for SERCA. We discovered that DABCYL was masking the effect of PLB phosphorylation probably due to DABCYL sticking to the membrane. A similar result was seen when a lipid anchor was synthesized on the N-terminus of PLB. This PLB with the lipid anchor was then phosphorylated, and no relief of inhibition was seen in the ATPase-assay. Further experiments with EPR noted an increase of the inhibitory form ("T" state) of PLB due to the lipid anchor (*85*).

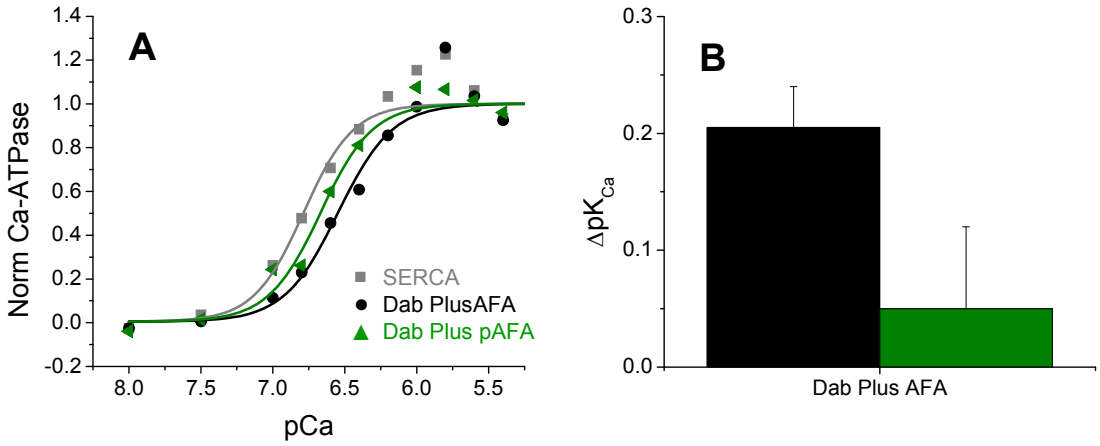

Figure 39:DABCYL PLUS effect on phosphorylation of PLB. A) Normalized Ca-ATPase curves fit with Hill Equation. B) The black bar represents unphosphorylated DabP-AFA and the green bar symbolizes phosphorylated DabP-AFA. PLB phosphorylation causes a partial relief of inhibition. Data represent the mean ± standard deviation of 2 separate trials.

To address this probe problem, preliminary experiments have already begun to look at the effect of DABCYL-PLUS, a hydrophilic derivative of DABCYL, on phosphorylation of AFA-PLB. The results have been positive; supporting the hypothesis that DABCYL masks the phosphorylation effect of PLB (Figure 39). Phosphorylation of DABCYL-PLUS AFA (DabP AFA) partially relieves the inhibition of SERCA by PLB. This response is greater than the effect seen with Dab-AFA by ~20% (compare Figure 37 B & Figure 39 B). Further experiments are needed to establish the effect of DABCYL-PLUS on inhibition and on phosphorylation.

APPENDIX 2 – Probing the SERCA-PLB Complex Using FRET

One study that has started in our laboratory using DABCYL is probing the SERCA-PLB complex. To date, there is no crystal structure of this complex. Therefore, I began labeling different sites in PLB with DABCYL to determine the distance between specific residues on PLB and SERCA using FRET. The first three distances are in good agreement with the modeled distances (Figure 40). The A24K distance varies from the predicted distance from the model, which will be used to refine the Toyoshima model based on cross-linking, crystallography, and NMR experiments (*74*). Since DABCYL does not affect measurements made here at low Ca^{2+}, the preliminary data collected is still valid. However, future studies need to include the effect of high Ca^{2+} and phosphorylation of PLB on the SERCA-PLB complex. These proposed experiments should be continued with DABCYL-PLUS. In addition, a different probe is required to measure the longer distances since the sensitivity range of DABCYL and DABCYL-PLUS is 16Å-48Å. 5-iodoacetamidofluorescein (5-IAF) has been selected in order to probe these longer distances in the transmembrane domain. These experiments will be insightful for

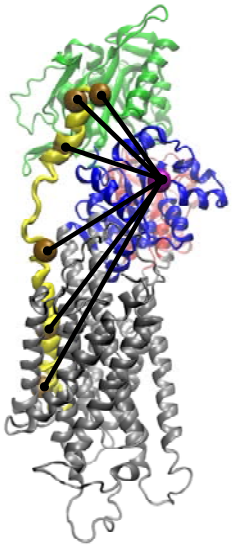

PLB site	Model (Å)	Expt (Å)
N-term	28.6	27 ± 1.9
K3	33.0	34 ± 1.1
A11K	26.6	25 ± 2.8
A24K	33.3	27 ± 1.0
C36	47.7	
C46	62.8	

Figure 40: SERCA-PLB complex detected by FRET. Model of SERCA-PLB complex by Toyoshima et al made using PyMol (*74*). Distances measured between the center of IAEDANS-SERCA and DABCYL-PLB. Mean ± standard deviation, n = 3.

understanding how these proteins interact and what structural rearrangements occur to relieve SERCA inhibition by PLB.